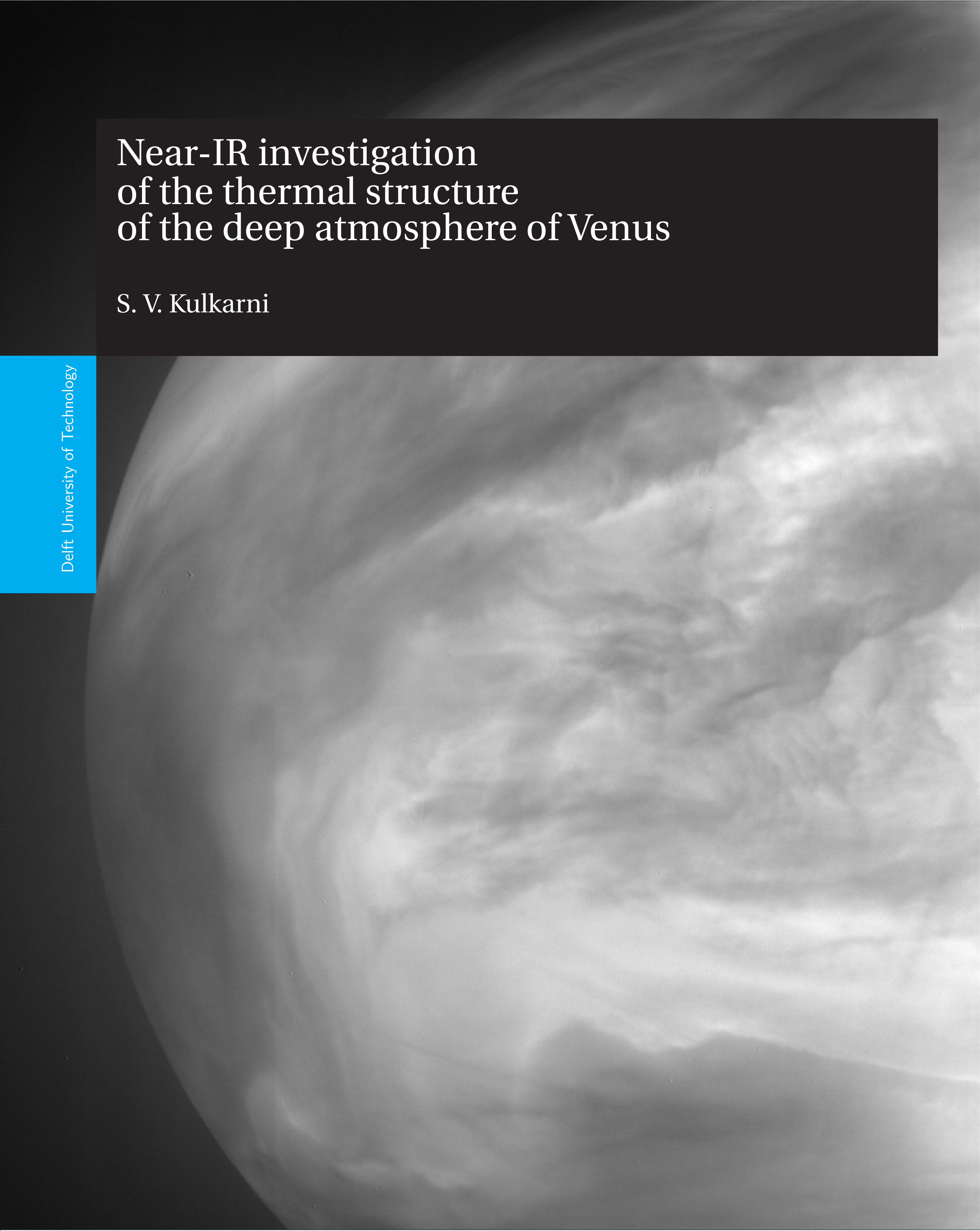

Near-IR investigation of the thermal structure of the deep atmosphere of Venus

S. V. Kulkarni

Delft University of Technology

TU Delft Delft University of Technology

Challenge the future

Near-IR investigation of the thermal structure of the deep atmosphere of Venus

By

S. V. Kulkarni

in partial fulfilment of the requirements for the degree of

Master of Science
in Aerospace Engineering

at the Delft University of Technology,
to be defended publicly on Friday, April 30, 2021, at 13:30.

Supervisor:	Dr. D.M. Stam	TU Delft / Astrodynamics and Space Missions
	Dr. N.T. Mueller	DLR Institute of Planetary Research / Planetary Physics Department
Thesis committee:	Dr. Ir. W. van der Wal	TU Delft / Astrodynamics and Space Missions
	Dr. A.A. Nuijens	TU Delft / Geosciences and Remote Sensing

This thesis is confidential and cannot be made public until April 30, 2023.

Abstract

Planet Venus is characterized by continuous global cloud cover along with extreme pressure and temperature conditions near the surface. In spite of a large number of in-situ missions, the knowledge of the deep atmosphere remains limited because of multiple instrument failures during various missions. In 1985, VeGa-2 provided the first and only high-resolution thermal measurements which indicated a highly unstable layer in the atmosphere below 7 km altitude. The physical explanation of such an unstable layer is not yet available, hence, the VeGa-2 measurements are not accepted in the Venus International Reference Atmosphere (VIRA). Lebonnois and Schubert (2017) tried to explain the VeGa-2 measurements by introducing a theory of a composition gradient in the LMD Venus global circulation model (GCM).

The research presented in this report aims at testing this theory by utilizing the near-infrared observations from Akatsuki (IR1) and Venus Express (VIRTIS) missions in combination with the altimetry observations Magellan Mission. The IR1 observations cover the high-lands on Venus and are important for our study. However, they are highly contaminated. To make use of IR1 observations, we first study the noise present in the data and develop a procedure to sequentially reduce this contamination to an acceptable level. Next, we develop an atmospheric radiative transfer model to simulate the thermal emission from the surface of Venus. This model is then used to retrieve the surface temperature values from the observations. Then, the surface temperatures are correlated with surface topography to generate temperature vs altitude profile.

The temperature vs altitude profile of IR1 and VIRTIS observations is compared with that from the results from LMD Venus GCM. From both the observations, we find a lapse rate smaller than VIRA below 2 km altitude which is in agreement with the GCM results and previous study by Meadows and Crisp (1996). Above this altitude, IR1 observations indicate a lapse rate higher than the GCM results indicating a possibly more complex situation in the atmosphere than the composition gradient. The IR1 observations also indicate a maximum deviation of ~5 K from the VIRA temperature profile at the altitude range of 4-5 km which coincides with the radiothermal emissivity anomaly (Klose et al., 1992). However, based on the quality of available data it is difficult to establish a firm relation. Thus, we highlight the need of future near-IR observations using an instrument optimized for thermal emission windows of Venus.

Acknowledgement

I would like to thank *Dr. Daphne Stam* for her supervision during the period of this thesis and the literature review. In addition to the scientific content discussed in our meetings, the meetings were really helpful to keep a check on the progress of the thesis work. Our meetings especially helped me with the radiative transfer part of the thesis. I would also like to thank her for the guidance and support regarding my future career path.

I would equally like to thank *Dr. Nils Mueller* for his supervision and support right from the selection of the thesis topic, during the literature review and the thesis. My understanding of the data processing techniques and Venusian studies was significantly enhanced through our meetings. I have learned a lot through our discussions. I would also like to thank him for his guidance and support for my future career path.

I would like to thank the lecturers and the staff from both the Space Engineering and Space Exploration profiles for offering wonderful coursework. I would also like to thank my friends at TU Delft for their support during the MSc program. I have really enjoyed the group assignments. Lastly, I would like to thank *Susan de Rouw* for the counseling sessions.

Additionally, I would like to thank my parents for supporting me throughout the duration of the MSc program. I would also like to thank my friends back at home for the virtual hangouts during the pandemic. Without continuous support from the family and friends in India, the journey of my MSc program would not have been possible.

Shubham
Delft, April 23, 2021

Contents

List of Figures

List of Tables

List of Abbreviations

Abbreviation	Meaning
ADU	Analogue to digital conversion unit
CDSD	Carbon Dioxide Spectroscopic Databank
CIA	Collision-induced absorption
FWHM	Full width at half maximum
GCM	Global Circulation Model
GTDR	Global Topography Data Records
HITEMP	High-TemperatureMolecular Spectroscopic Database
HITRAN	High Resolution TransmissionMolecular Spectroscopic Database
IFOV	Instantaneous field of view
IR1	1µm camera
IR2	2µm camera
LMD	Laboratoire de Météorologie Dynamique
NER	Net Exchange Rate
NIMS	Near-InfraredMapping Spectrometer
NIR	Near-infrared
OIR	Infrared radiometer
PBL	Planetary Boundary Layer
SAR	Synthetic Aperture Radar
UV	Ultraviolet
VCO	Venus Climate Orbiter
VeGa	Venera (Venus) and Gallei (Halley)
VEM	Venus Emissivity Mapper
VeRa	Venus Express Radio Science experiment
Vex	Venus Express
VIMS	Visual InfraredMapping Spectrometer
VIRA	Venus International Reference Atmosphere
VIRTIS	Visible and Infrared Thermal Imaging Spectrometer
VMC	VenusMonitoring Camera

LIST OF SYMBOLS

Symbol	Meaning	Units
τ	Optical depth	-
r	Particle size radii	µm
λ	Wavelength	µm
U	Internal energy	J
R	Universal gas constant	$J/(mol * K)$
μ	Mean molecular mass	g/mol
c_p	Specific heat at constant pressure	J/kgK
c_v	Specific heat at constant volume	J/kgK
v	Specific volume	m^3/kg
ρ	Density	kg/m^3
p	Pressure	bar, mbar
T	Temperature	K
Γ	Temperature lapse rate	K/km
θ	Potential temperature	K
θ'	Modified potential temperature	K
S	Static Stability	K/km
Ba	Bias	$W/m^2/sr/\mu m$
$NL_{x,y}$	Non-linear noise	$W/m^2/sr/\mu m$
L_y	Linear noise	$W/m^2/sr/\mu m$
$V_{x,y}$	Vignette	$W/m^2/sr/\mu m$
$N_{x,y}$	Total noise	$W/m^2/sr/\mu m$
ξ	cosine of the emission angle	
$P(\xi)$	synthetic limb darkening function	
$I(\xi)$	Observed radiances at emission angle $\cos^{-1}(\xi)$	$W/m^2/sr/\mu m$
$I(1)$	Nadir radiances	$W/m^2/sr/\mu m$
b	Optical thickness of a particular layer in the model atmosphere	
B	Optical thickness of the entire atmospheric column	
B^a	Optical thickness of the aerosols in the entire atmospheric column	
B^m	Optical thickness of the molecules in the entire atmospheric column	
B_{sca}	Scattering optical thickness of the entire atmospheric column	
B_{abs}	Absorption optical thickness of the entire atmospheric column	
$L(\lambda, T)$	Spectral radiance at the given wavelength (λ) and temperature (T) as per Planck's law	$W/m^2/sr/\mu m$
L_{surf}	Thermal emission from the surface	$W/m^2/sr/\mu m$

L_{atm}	Thermal emission from the atmospheric layer	$W/m^2/sr/\mu m$
A_g	Ground surface albedo	
a	Single scattering albedo	
α	CIA Coefficient	$cm^{-1}amagat^{-2}$
l	Atmospheric layer thickness	cm
χ	Line shape function	
ν_0	Wavenumber of the spectral line center	cm^{-1}
ν	Wavenumber	cm^{-1}
$\delta\nu$	Difference between ν_0 and ν	cm^{-1}
θ	Angle made by outgoing radiation with respect to the normal of the atmospheric plane	°
μ	Cosine of θ	
$\mathrm{I_{IR1}}$	The lookup table of radiance vs altitude, radiances are calculated by using the IR1 transmission filter	$W/m^2/sr/\mu m$
$\mathrm{I_{VIRTIS}}$	The lookup table of radiance vs altitude, radiances are calculated by using the VIRTIS transmission filter	$W/m^2/sr/\mu m$
R_{obs}	Observed radiance	$W/m^2/sr/\mu m$
R_{sim}	Simulated radiance for the corresponding location of R_{obs}	$W/m^2/sr/\mu m$
B	Radiances as per plancks function	$W/m^2/sr/\mu m$
T	Temperature	K

1

INTRODUCTION

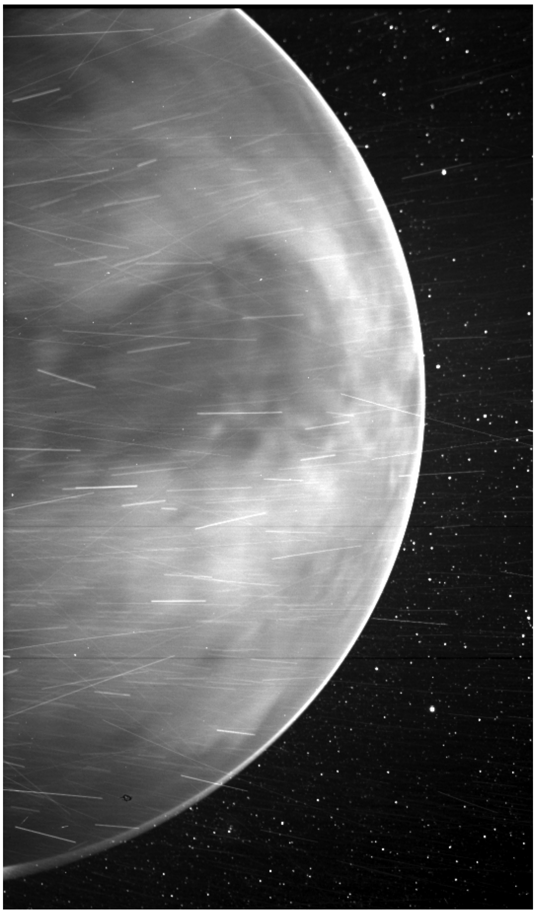

Figure 1.1: Venus nightside captured by the WISPR instrument on-board the Parker solar probe during the flyby in July 2020 (Buckley, 2021). The dark region in the center of the disk is the Aphrodite Terra, a high land on Venus. The bright streaks are caused by the sunlight reflected by charged particles.

Venus, the second-brightest object in the night sky, has been an important part of human culture since the earliest of times. It served as a prime source of inspiration for various writers, poets, philosophers, but most importantly, as a key object of study for nearly three millennia. Due to similarities in size, mass, composition, and distance to the Sun, Venus was known as Earth's sister planet. However, with the advancement of technology in the mid-20th century, various aspects of the planet slowly came into light and this picture changed drastically. In 1967, Venera 4 became the first probe to perform the in-situ measurements of a planet's atmosphere other than Earth. Since then, there have been many successful missions to Venus including 10 flybys, 21 landers/probes/balloons, 5 gravity assists, 8 orbiters (Taylor et al., 2018), and several future missions are in planning. The latest observation of Venus nightside during a flyby by Parker solar probe in July 2020 is shown in Figure 1.1.

Now, it is established knowledge that Venus has an average surface temperature of 737 K with a surface pressure of 92 bar. Carbon Dioxide (96.5%) and Nitrogen (3.5%) are the major components of its atmosphere. Although similar in size to Earth with a radius of ~0.950 Earth radii, it has a very long sidereal rotational period equivalent to 243.0212 Earth days (Campbell et al., 2019). The planet rotates in a retrograde direction with an axial tilt of 2.64°, making it the only planet in the solar system to have a retrograde rotation. The sidereal orbital period of Venus is 224.701 Earth days, thus one year on Venus is equivalent to 0.92 Venusian days.

In spite of the emphasis on Venus during the early space exploration days through the Mariner, Venera, Pioneer, VeGa missions, along with the more recent missions like Magellan, Venus Express, Akatsuki, it remains an object of mystery and curiosity. It provides an example of terrestrial planet formation and evolution which is substantially different from Mercury, Earth, and Mars. Numerous compelling questions remain about Venus and its relation with other terrestrial planets. Studying Venus is also important for a better understanding of comparative planetology along with exoplanet characterization. The retrograde rotation of Venus is another unexplained phenomenon. The lack of magnetic field, and the current surface condition raises more questions about the interior and surface evolution of the planet. Unlike Earth, not having plate tectonics, the current state of volcanic activity remains unknown. This creates a need for investigations for a possible relationship between planet interior, surface, and the extreme conditions of deep the atmosphere.

In the absence of new missions, the research can still be pursued via utilizing previous observations in novel ways along with new ground-based observations, and experimental studies. Such studies not only advance the state of knowledge but also continue to provide new information that can help guide requirements for future missions. In this report we focus on the investigation of the thermal structure of the deep atmosphere of Venus using near-infrared observations from Akatsuki and Venus Express spacecraft. The Section 1.1 provides the background for this study.

1.1. Need for investigations of the deep atmosphere of Venus

Having the densest atmosphere among the four terrestrial planets, Venus is under the constant coverage of clouds, which makes the observation of surface and deep atmosphere a very difficult task. This is why the planet has been targeted by a number of probes, balloons, and landers to perform in-situ observations. However, due to the extremely hostile conditions, the thermal structure, particularly below 12 km, is not well known.

The vertical coverage of the thermal structure provided below 12 km altitude by the Venera landers and probes was limited (Seiff et al., 1985). The temperature sensors of all 4 Pioneer Venus descent probes failed at 12.5 km above the surface in 1980 (Seiff et al., 1980). In 1985, VeGa 2 probe acquired the first and only reliable temperature profile below this altitude (Linkin et al., 1986). However, these measurements showed large negative values of static stability below 7 km altitude, implying unrealistic convective heat transport in that region (Seiff, 1987). This temperature profile can be explained by a gradient in the composition of the atmosphere with the abundance of Nitrogen gradually decreasing to near-zero at the surface (Lebonnois and Schubert, 2017). Simulations using the global circulation model of Venus have been carried out to check if such a gradient can be sustained in the atmosphere of Venus (Lebonnois et al., 2018). However, the mechanism required to naturally form such a composition gradient is currently not quite clear. One of the possible explanations can be a diffused degassing of Carbon dioxide from ongoing low volcanic activity(Cordier et al., 2019). In this context, it would be interesting to understand whether the temperature gradient observed by Vega 2 is a global phenomenon.

In 1984, the NIR spectral windows of the atmosphere of Venus were discovered (Allen and Crawford, 1984) which allow us to probe the atmosphere at various altitudes and observe surface thermal emission. The surface temperature is governed by atmospheric temperature due to the lack of direct sunlight and the intense greenhouse effect, which limit the local heating and cooling of the surface. This means the temperature of the atmosphere can be inferred from observations of surface temperature. Thus, the data from the recent Akatsuki mission, the Venus Express mission along with observations from ground-based telescopes can be used to construct a global map of the surface temperature. A comparison of this map with the thermal map from the near-surface atmospheric dynamics generated by Lebonnois et al. (2018) can tell us if the predictions of composition gradient match the reality. This comparison is the primary aim of the research described by this report.

Such a map of observed surface temperatures can be correlated with the topography to generate the thermal profile of the deep atmosphere. This profile can be used to suggest a possible update in the Venus International Reference Atmosphere (VIRA) model (Kliore et al., 1985). The map of the observed surface temperatures is also important to be able to accurately derive the surface emissivity, which will allow a more accurate mapping of surface composition. The VIRA temperature profile has been used for this purpose so far, however, it is too simplistic and might result in an altitude-dependent bias in the estimation of surface emissivity (Hashimoto et al., 2009). Lastly, the near-IR instruments onboard both the Akatsuki and Venus Express missions were not optimized for observations in the surface observing windows. This work can be used to emphasize the importance of surface observing windows and it can be further used to provide support for the selection of an optimized near-infrared instrument onboard upcoming Venus missions.

1.2. Structure of the Report

The temperature structure of the deep atmosphere of Venus is briefly reviewed along with the predictions of the global circulation model from Lebonnois et al. (2018) in the Chapter 2. Chapter 3 provides information on the near-IR observations from the Venus Express (VIRTIS) and Akatsuki (IR1) missions. The noise present in the IR1 dataset and the processing steps developed to reduce this noise are discussed in Chapter 4. The development of the atmospheric radiative transfer model is described in Chapter 5. The surface temperatures are retrieved from the IR1 and VIRTIS dataset in Chapter 6. The main conclusions from this thesis report are highlighted in Chapter 7.

In addition to above, the reader is redirected to Appendix A for a brief review on the atmosphere of Venus. The Appendix B explains some theoretical aspects required for Chapter 2. Appendix C lists the orbits of Akatsuki mission containing useful observations which are described in Section 4.1. Lastly, high resolution and enlarged versions of the surface temperature maps that are discussed in Chapter 6 are provided in Appendix D.

Also, it should be noted that the altitude values of the surface features mentioned in this report are referenced with a planetary radius of 6051 km except noted otherwise. For simplicity of modeling, in Chapter 5 the altitude values are referenced with a planetary radius of 6048 km.

2

Thermal Structure of the Deep Atmosphere of Venus

The physical properties of the atmosphere of Venus, recorded via various instruments onboard various missions to Venus are collectively stored into **VIRA** (Venus International Reference Atmosphere) (Kliore et al., 1985). The vertical thermal structure of the VIRA model was divided into three main parts which differ from each other in terms of the type of exploration methods required and the physical conditions inside. They are listed below:

1. **0–40 km:** Exploration only via direct measurements.
2. **40–60 km:** Exploration via direct measurements and radio occultation.
3. **60–100 km:** Exploration via direct measurements, radio occultation, accelerometry, and IR-spectrometry

This chapter deals with the thermal structure of the first part mentioned above, i.e., from 0 to 40 km. Below the 30-35 km altitude, the refraction strongly bends the radio beams which prevents the determination of the atmospheric profile using radio occultations. Thus, in-situ measurements are necessary for the effective measurement of the thermal properties. In VIRA, Seiff et al. (1985) developed the thermal structure of the lower atmosphere by combining the in-situ observations from Venera probes (8 to 12) and four Pioneer Venus probes which are discussed in Section 2.1. VeGa-2 lander provided the first reliable measurements below 12 km altitude, indicating a highly unstable region near the surface which is described in Section 2.2. Key features of LMD Venus GCM are highlighted next in Section 2.3, which was used by Lebonnois and Schubert (2017) to provide a possible explanation for the VeGa-2 measurements (Section 2.4). To test this theory, a novel method is proposed in Section 2.5. Various aspects of the atmosphere of Venus are briefly reviewed in Appendix A. The theoretical background required for this chapter is provided in Appendix B.

2.1. The development of VIRA profile for the Lower Atmosphere

As a part of the Russian **Venera** program, a total of 8 probes successfully landed on the surface of Venus, gathering the in-situ information. The temperature profiles recorded by Venera 8 to 12 along with the Pioneer sounder probe is shown in Figure 2.1. Although the temperature measurements were successfully taken till the surface, the measurements disagreed by up to 55 K at an altitude of 40-30 km. At the surface, the measurements showed a scatter of up to ±6 K. This wide range of measurements at the 30-40 km altitude indicated a measurement uncertainty (Avduevskij et al., 1976, 1979, Avduevsky et al., 1983). The static stability derived from the Venera 10,11,12 is shown in Figure 2.2. It can be observed that the vertical resolution of the Venera measurements was lesser than that of Pioneer Venus probe measurements (explained next). Also, the scarcity of the static stability measurements below the 12 km altitude is evident.

In 1978, as part of the **Pioneer Venus** program, four entry probes (named Large/Sounder, Night, Day, North) plunged into the atmosphere of Venus at four different locations and provided simultaneous measurements from an altitude of 126 km. However, the temperature sensors of all 4 probes failed beyond 630 k - 40 bar atmospheric condition, which is nearly at 12 km altitude from the surface. The static stability derived from the Pioneer Sounder and North probe is shown by the solid lines with white points in Figure 2.1. It can be observed that the measurements are limited till the 12 km altitude.

While generating the VIRA model of the atmosphere below 12 km, a weighted average of the extrapolated data from Pioneer Venus probes and Venera 10 lander was taken (Seiff et al., 1985). As the measurements from Pioneer Venus were extrapolated, more weightage was given to Venera 10 measurements. The temperature and static stability profile of VIRA is shown in Figure 2.3 and Figure 2.4 (red dashed lines) respectively. It can be observed that the model retains the observed stability structure. Over time, through various ground-based and spacecraft observations, many modifications were made in the upper atmosphere models of VIRA, however, for the lower atmosphere part below 35km, the VIRA model was unchanged due to lack of new in-situ observations (Limaye et al., 2018a). A brief review of the thermal structure of the atmosphere of Venus at higher altitudes is provided in Section A.1.

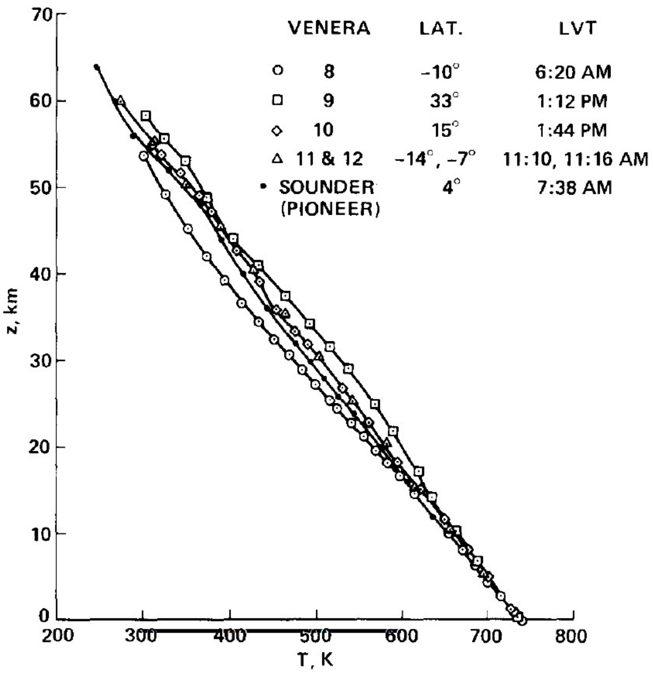

Figure 2.1: Temperature profiles from Venera 8 to 12 and Pioneer Sounder Probe (Seiff et al., 1985)

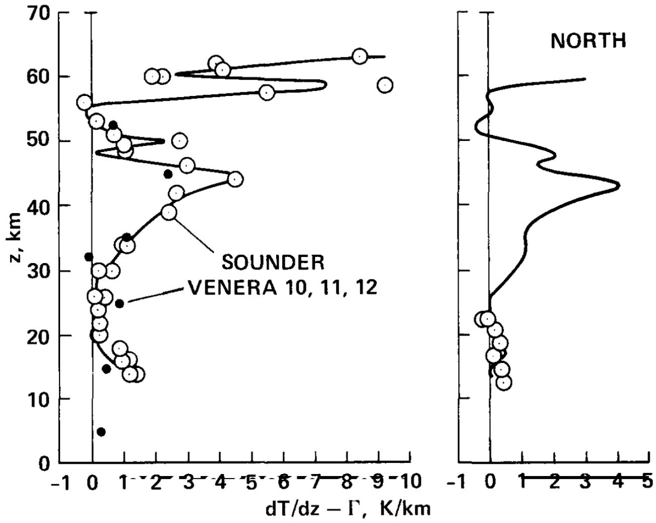

Figure 2.2: Static stability profiles from Venera 10 to 12 and Pioneer Sounder and North Probes (Seiff et al., 1985)

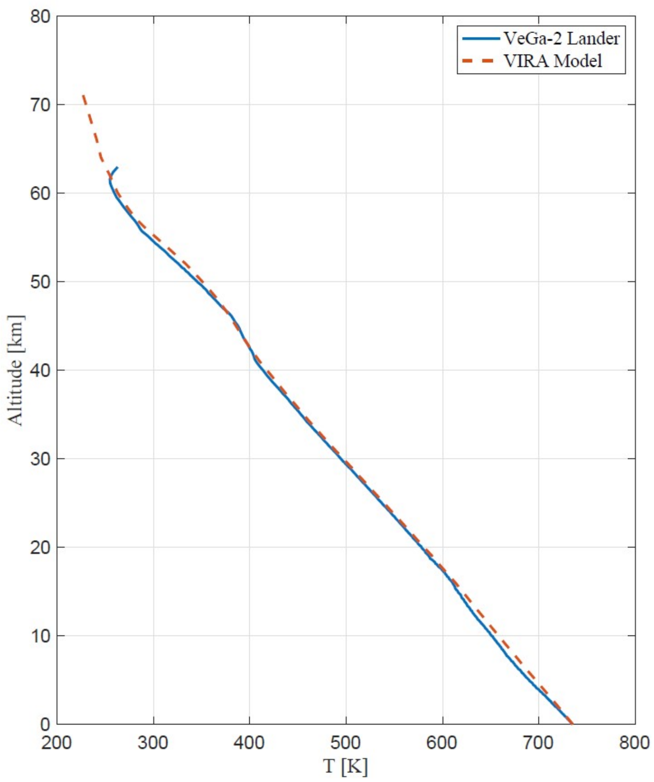

Figure 2.3: Temperature profiles measured by VeGa-2 (solid line) and the temperature profile in the VIRA model (dashed line) (Dutt and Limaye, 2018)

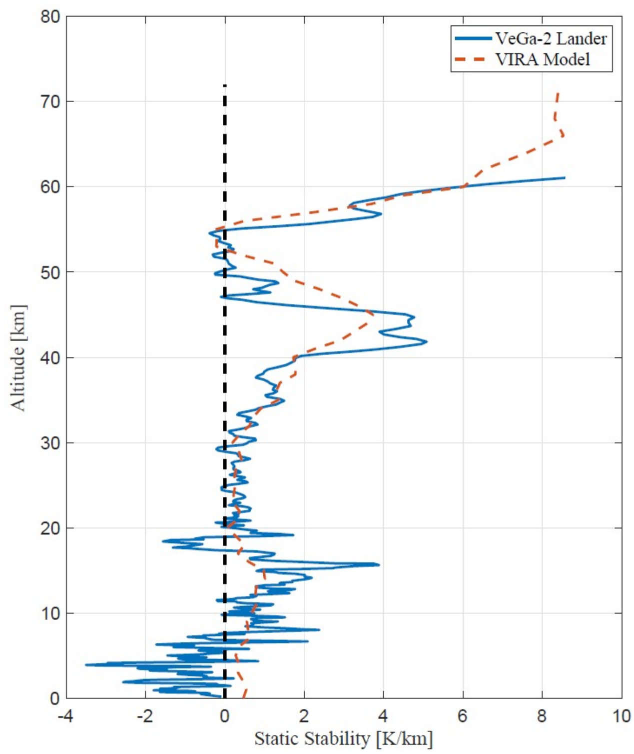

Figure 2.4: Static stability profiles from VeGa-2 and VIRA, calculated by using GREG2008 mixture model by Dutt and Limaye (2018)

2.2. The in-situ measurements from the VeGa-2 Lander

In 1985, the **VeGa-2** lander touched down at the Aphrodite Terra and became the first lander to successfully provide a reliable and high resolution temperature profile below the 12 Km altitude (Linkin et al., 1986). The atmospheric measurements were taken with the help of two temperature sensors (T_1, T_2) and three pressure sensors (P_1, P_2, P_3). The temperature sensors were designed such that they have short but different time constant, and are stable against mechanical loads and corrosive action of the environment. The sensor T_1 was a bar platinum wire, double-wound on a ceramic form and had a time constant of 0.1 sec. The sensor T_2 was also made of a platinum wire which was placed inside a ceramic shield, and had a time constant of 3 sec. The measurement range for both the sensors extended from 200 to 800 K, with a measurement accuracy of $\pm$0.5 K. Similarly, all the three pressure sensors had a different design with an operating range of 0-2, 0-20, 2-110 bar and an absolute measurement accuracy for 1 mbar, 10 mbar, and 500 mbar for sensors P_1, P_2, and P_3 respectively. The surface measurements at the landing site were 733$\pm$ 1 K, 89.3$\pm$ 1 bar(Linkin et al., 1986).

A comparison of the temperature and static stability profiles taken by the VeGa 2 lander and that of VIRA is shown in Figure 2.3 and Figure 2.4. Here, the static stability profile is recalculated by Dutt and Limaye (2018) based on the GREG2008 mixture model using 96.5% Carbon dioxide and 3.5% Nitrogen for Venus. These results are similar to the static stability profiles obtained by Linkin et al. (1986), based on 100% Carbon dioxide approximation used by Seiff et al. (1980) with the gas properties taken from Hilsenrath (1960). It can be observed that the VeGa-2 profile, even though measured 6.5 years later, is remarkably similar in the altitude range of 35-20 km with that from the Pioneer Venus Probe (used for VIRA calculations). However, it becomes highly negative below 7 km altitude and returns to near-zero value on the surface. Thus, although at the surface the atmosphere seems stable, a super-adiabatic layer lies above the surface centered at 4 km altitude. This unstable layer indicates highly unrealistic heat transport near the surface.

By using the ground-based observations in the near-IR spectral windows at 1.18 µm, Meadows and Crisp (1996) suggested stability in the near-surface layer of the atmosphere till 6 km altitude. This contradicts the stability profile measured by VeGa-2. The radiative surface heating on Mars causes an unstable layer near the surface with highly active convection up to 9 km altitude (Spiga et al., 2010). However, this mechanism is not expected on Venus, given that only 2% of solar radiation reaches the surface (Read et al., 2016). Thus, due to the lack of explanation of the VeGa-2 profile, it was not incorporated into VIRA.

2.3. LMD Venus GCM by Lebonnois et al. (2010)

Global Circulation Models (GCM), based on computational fluid dynamics, are used to simulate the dynamical processes inside a planetary atmosphere with varying temporal and spatial resolution. GCMs are important tools to study the atmospheric temperature structure along with the atmospheric dynamics and circulation, and they have played an important role in understanding the characteristic features of the atmosphere of Venus (Sánchez-Lavega et al., 2017). Various GCMs for the atmosphere of Venus have been developed in recent years which are recently reviewed in Lewis et al. (2013). Section A.3 provides a brief review of the global circulation and dynamics in the atmosphere of Venus.

One of the most challenging aspects of the development of the GCM for Venus is to include the full radiative transfer calculations which are required for more realistic simulations of the atmospheric thermal structure. The primary inputs for these calculations include a priori temperature profile and the cloud optical thickness distribution which is determined by the structure and properties of clouds, atmospheric composition, and the spectral properties of constituents.

Lebonnois et al. (2010) presented a GCM for Venus, called the LMD Venus GCM, which was based on the LMDZ model for Earth (Hourdin et al., 2006). (LMD stands for Laboratoire de Météorologie Dynamique.) The important features of this model are listed below:

- This model includes the topography with basalt like thermophysical properties.
- The solar heating rates are taken from the look-up tables provided by Crisp et al. (1996) which are computed as a function of solar zenith angle. The diurnal cycle is then accounted for by interpolating to get the correct solar zenith angle for each GCM grid point.
- The dependence of specific heat capacity ($c_p(T)$) on temperature is taken into account which is important for the atmosphere of Venus. This changes the definition of the potential temperature, θ, which is discussed in Subsection B.1.2.
- The radiative transfer calculations are based on the Net Exchange Rate (NER) matrix formalism used by Eymet et al. (2009). In this method, the heating rate of a particular layer is calculated as the sum of radiative net exchanges with all other atmospheric layers, including the surface and space. The NER exchange coefficient matrix is calculated assuming NER between two layers is equal to an optico-geometric exchange coefficient multiplied by the difference between the Planck functions of the two layers. This matrix is then used in the GCM to compute the temperature profile self consistently.

- The Lebonnois et al. (2010) GCM used a horizontal resolution of 48 longitudes × 32 latitudes, on 50 vertical levels, from the surface up to 95 km. The resolution was upgraded to 96 longitudes × 96 latitudes by Lebonnois et al. (2016).

- To add the effects associated with PBL, a boundary layer scheme based on Mellor and Yamada (1982) which physically represents the unstable regions was introduced in Lebonnois et al. (2016) GCM. This scheme has been successfully used for LMD GCM for Titan (Lebonnois et al., 2012).

2.4. The composition gradient proposed by Lebonnois and Schubert (2017)

To assess the stability of the temperature profile provided by VeGa-2, Lebonnois and Schubert (2017) use the potential temperature profile (Equation B.16) as shown in Figure 2.5. The almost constant potential temperature denotes that the atmosphere is marginally stable, e.g., in the altitude ranges 55-50 km and 32-20 km, which can also be seen as near-zero values in the static stability profile shown in Figure 2.4. The slope of the profile becomes strongly negative below 7 km which indicates high instability as discussed earlier.

This temperature profile was indicated by the two temperature sensors T_1, T_2 of Vega-2 with simultaneous measurements. The design and the time constants of both sensors were different (Section 2.2), hence, the probability of a systematic error occurring in both the sensors resulting in a continuous negative gradient from 7 km altitude to the surface is very low. The potential temperature and thus, the stability is calculated from Equation B.16 and Equation B.19 using the assumption that the mean molecular mass (μ) remains constant, which is the general case for homogeneous planetary atmospheres. However, if we include the possibility of varying composition and assume that the near-surface layer is marginally stable, then it would result in a vertical gradient in μ which varies from 44.0 g/mol at the surface to 43.44 g/mol at the 7 km altitude. Lebonnois and Schubert (2017) introduced this composition gradient into the Lebonnois et al. (2016) GCM of Venus which showed stability in the near-surface layers. The derivation for the equation of potential temperature (θ) and the static stability (S) when μ is changing with respect to altitude is given in Section B.2.

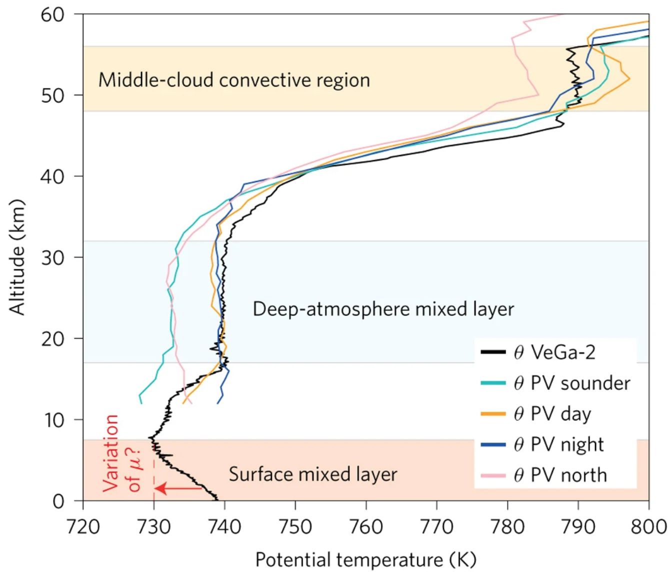

Figure 2.5: Altitude vs Potential Temperature plot of VeGa-2 and Pioneer Venus probes (Lebonnois and Schubert, 2017)

The μ at surface obtained above, i.e. 44.0 g/mol, denotes the composition of almost pure CO_2. Thus, it can be inferred that N_2 content in the atmosphere decreases from 3.5% above the 7 km altitude to almost zero near the surface following a gradient of 5 ppm/m. However, before accepting this theory, a physical explanation of the origin of such a temperature gradient is necessary. The possible hypothesis that could explain this gradient are tested below:

- A high pressure equilibrium separation of CO_2-N_2 under super-critical conditions was experimentally demonstrated by Espanani et al. (2016), Hendry et al. (2013). The pressure range for these experiments was above 100 bar, but the temperature was maintained near 298 K. Thus, the temperature conditions were clearly different from that in the deep atmosphere of Venus. Cordier et al. (2019) investigated this process in the Venusian context by using molecular dynamics simulations based on an appropriate equation of state for the binary mixture of CO_2/N_2. Their results showed that the phase separation based on molecular diffusion alone is unlikely.

- Lebonnois et al. (2020) tried to investigate the homogeneity of CO_2/N_2 gas mixtures experimentally. The experiment was carried out using 70 cm long pressure vessel with 8.7 cm diameter, under a pressure of 100 bar, with temperature ranging from ~296 to ~735 K. They couldn't arrive at a firm conclusion about potential phase separation, however, the experiment suggested that the compositional gradient can last for a long period of time against molecular diffusion, but it would be affected by turbulence and circulation. Using the LMD Venus GCM (Lebonnois et al., 2016), it was found that the average amount of N_2 near the surface would increase by 1% just in three Venusian days (Lebonnois et al., 2018).

- Thus, due to lack of support from density-driven hypothesis, an extrinsic mechanism that could sustain such a gradient for longer time scales is necessary. Cordier et al. (2019) suggest a diffuse degassing of CO_2 from a low volcanic activity. It could be possible, this activity was a local event in the vicinity of the landing site of VeGa-2. However, if such out-gassing was a global event Cordier et al. (2019) estimate that it would result in a 10 mbar increase in the pressure of atmosphere of Venus every Earth-year, which is a significant amount as it would correspond to an increase of ~1 Earth atmosphere in about every 1000 Earth years. Thus, a strong sink for CO_2 would be required, however, the possibility of such a sink is highly unlikely with known geological processes.

- Lebonnois et al. (2020) consider another hypothesis of SO_2 outgassing from the surface, setting up a composition gradient with a 2.8% mole fraction of SO_2 at the surface decreasing to roughly 0.01% at the altitude of 7km. However, due to the lack of a known SO_2 sink in the near-surface layers, such a gradient would be difficult to maintain against the dynamical mixing.

As seen above, a physical explanation of the composition gradient is still not available. Further complicating the matters, Peplowski et al. (2020) reported the first measurement of N_2 content in the 60-100 km altitude range to be 5±0.4%. This amount was ~40% higher than the amount measured below the altitude of 50 km which is 3.5%. This discovery defies the earlier models of the homogeneous composition below the lower mesosphere of Venus and supports the possibility of chemically distinct regions in the atmosphere of Venus. And thus, supporting the theory of composition gradient in the deep atmosphere. Nevertheless, due to the absence of both direct measurements and the physical explanation for the compositional gradient in the deep atmosphere, new in-situ compositional measurements of the deep atmosphere are required. Another method based on near-IR observations that could verify the theory of the composition gradient is discussed in Section 2.5.

2.5. Investigation of the composition gradient using Near-IR observations

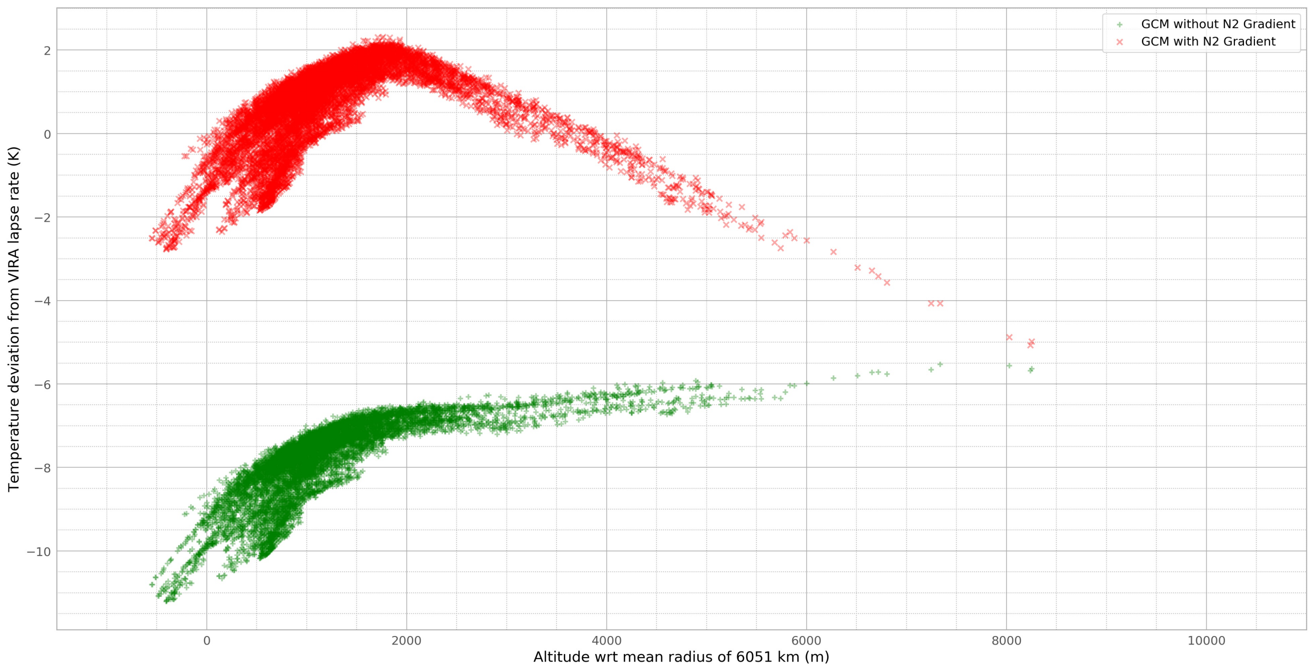

Figure 2.6: The plot of temperature deviation against the altitude for the GCM with and without the proposed N_2 gradient.

Lebonnois et al. (2018) provide the results generated from the GCM model with and without the proposed N_2 gradient. The results from both the GCMs are in the form of a grid of 96 latitudes x 96 longitudes and are simulated for 48 hours of Venusian time (2 Venusian days). The reported diurnal variation in the surface temperatures is less than 3 K (Lebonnois et al., 2016, 2018). We take the time average of these results to generate the global surface temperature maps from both the GCMs. The scatter plots of deviation of the surface temperature averages with respect to VIRA temperature profile against the surface altitude are shown in Figure 2.6. The red markers denote the results from the GCM model with the N_2 gradient while green markers denote the results from the GCM model without the proposed N_2 gradient (i.e. the normal atmospheric composition). Both the scatter plots have a small offset with respect to the VIRA profile. This offset is attributed to the radiative balance in the GCM which is explained in Garate-Lopez and Lebonnois (2018), Lebonnois et al. (2016). Considering this as a model artifact, we adjust both the plots for this temperature offset and focus on the trend shown by both the plots. The adjusted surface temperature plots from both the GCMs are shown in Figure D.4 and Figure D.5. It can be observed that both plots show a similar trend till 2 km altitude. Above this altitude the plot of the GCM without N_2 shows a nearly constant temperature with respect to VIRA with a small increase as we move towards higher altitudes. However, the plot of GCM with N_2 becomes strongly negative moving towards higher altitudes.

The J-band spectral windows of the atmosphere Venus (Subsection 5.1.1) allow us to observe the thermal emission from the surface of Venus, which can be used to retrieve the surface temperature and create a global thermal map. Lecacheux et al. (1993) report that the thermal emission in 1 μm window, coming from the surface, is consistent with the surface temperature in equilibrium with the atmospheric temperature at that altitude. Thus, by correlating the observations in this spectral window with the topography, a global temperature profile can be generated. This profile can then be compared against the temperature deviation plot (Figure 2.6) discussed above. The comparison can be made for specific highlands, including the VeGa-2 landing site, and globally as well. Based on this comparison, the validity of the proposed composition gradient can be tested. To be able to compare the surface temperature profiles of specific regions, we need high resolution near-IR observations which are usually provided by the space missions as compared with the ground-based observations. The near-IR observations that are used in our study are discussed in the next in Chapter 3.

3

Observations

Since the discovery of near-IR spectral windows by Allen and Crawford (1984), there have been various space-based and ground-based observations of the nightside of Venus. The Galileo/NIMS (Near-Infrared Mapping Spectrometer) provided the partial mosaics of the nightside of Venus in pre-selected 17 wavelengths including 0.94 and 1.18 μm (Carlson et al., 1991). During the Cassini-Venus flyby, the VIMS instrument captured a single 10s integration of the night-side spectra covering 0.35 to 1.05 μm (Baines et al., 2000). The VEx/VIRTIS and Akatsuki/IR1 provided the highest spatial resolution observations of the nightside of Venus and are used for our study.

The ground-based observations were mainly focussed on the 1.7 and 2.3 μm windows and are utilized to study cloud variability and derive abundances of various species (Allen, 1987, Allen and Crawford, 1984, Bailey et al., 2008, Bell et al., 1991, Bézard et al., 1990, Crisp et al., 1991, de Bergh et al., 1995, Iwagami et al., 2008, Marcq et al., 2005, Meadows and Crisp, 1996, Ohtsuki et al., 2008). Our study requires observations in surface observing 1 μm window which were taken by Arney et al. (2014), Bailey et al. (2008), Lecacheux et al. (1993), Meadows (1992). The spectroscopic imaging observations taken by Arney et al. (2014) are especially useful for this study as they cover a wavelength range of 0.96 to 2.47 μm. Although the spatial resolution of the ground-based observation is lower than the space-based observations, it is possible to conduct these observations on regular intervals. Thus, in future, our study can be extended using the past and new ground-based observations.

In this study, we mainly focus on the space-based observations. The observations from Venus Express mission are discussed in Section 3.1. Then the observations from the Akatsuki mission are described in Section 3.2.

3.1. Venus Express Observations:

The Venus Express (VEx) spacecraft was inserted into an orbit around Venus in April 2006, with science goals pertaining to the investigation of the atmosphere, the plasma environment, and the surface (Titov et al., 2006). The orbit was elliptical with an apocenter roughly 66,000 km above the South Pole and a pericenter 250-350 km above the North Pole. The spacecraft was equipped with two imaging instruments that observed in the NIR wavelengths, the Venus Monitoring Camera (VMC) and the Visible and Infrared Thermal Imaging Spectrometer (VIRTIS).

VMC was a multispectral imager with four objectives, having narrow bandpass filters, sharing four quadrants on the same CCD. It observed in UV band centered at 365nm, in Visible band centered at 513nm, and in NIR bands 965nm and 1000nm with a bandwidth of 40nm (Markiewicz et al., 2007a). VMC successfully operated in orbit around Venus until November 2014 covering the full diurnal cycle of Venus more than four times Titov et al. (2012). The observations at 1.0 μm from VMC cover the highlands near the equatorial region, however, the efficiency of the detector at this wavelength was much lower (∼ 2%) (Basilevsky et al., 2012) which makes them less suitable for our study.

The **VIRTIS instrument** was a dual instrument with two channels taking input through two separate telescopes. The first channel called VIRTIS-M operated in two modes:(1) VIRTIS-M-VIS operated as a mapping spectrometer in the visible range,i.e., from 0.28 to 1.1 μm with a spectral sampling of 1.9nm. (2) VIRTIS-M-IR operated as a mapping spectrometer in the infrared range (1.02 to 5.19 μm) with a spectral sampling of 9.8 nm. The instantaneous field of view (IFOV) of the slit used for this channel was 0.25x0.64 mrad (Piccioni et al., 2007). The second channel known as VIRTIS-H was a high-resolution spectrometer (1.84 to 4.99 μm.) with a spectral sampling of 0.6 nm.

The VIRTIS-M-IR mode observed the surface in three spectral windows at 1.02, 1.1, and 1.18 μm from May 2006 till Oct 2008, covering nominal mission phase and first mission extension, when due to the failure of the cryocooler the operations had to be stopped. Due to a highly elliptical orbit, the field of view and the dwell time was much shorter near the North Pole. Thus, the coverage of the Southern Hemisphere was much better than that obtained for Northern Hemisphere. The VIRTIS-M-IR dataset has been used by various authors for surface and near-surface atmospheric studies (Arnold et al., 2015, Barstow et al., 2012, Bezard et al., 2009, Cardesín-Moinelo et al., 2020, Haus and Arnold, 2010, Kappel, 2014, Kappel et al., 2012, 2015, 2016, Limaye et al., 2017, Marcq et al., 2009, Mueller et al., 2008, 2017, 2018, 2020, Titov et al., 2012).

3.1.1. VIRTIS Data Preparation

The data from VIRITS-M-IR channel is presented as three-dimensional cubes with 431 bands (b) representing the spectral dispersion of light across the detector, 256 sample (s) representing the spatial direction along the instruments slit. The third dimension of lines (l) is created by the movement of a scanning mirror between readouts of the detector. The calibrated dataset shows some artifacts that need to be corrected.

The processed dataset is received from Mueller et al. (2020) that was used for the surface emissivity studies. This dataset was constructed by extracting the observations at 1.02 µm (VIRTIS band 0). The observations were corrected for limb darkening using the method provided by Mueller et al. (2008). The cloud optical thickness variations are corrected by using the radiance at 1.31 µm (VIRTIS band 29). To exclude the effect of the twilight, the pixels with the solar incidence angle less than 100°are discarded. The highest quality data is selected by limiting the emission angle to 70°. The individual observations are map projected using Lambert's azimuthal equal-area projection centered on the South pole and are combined by taking a median of all the different observations of the same location. The best quality pixels are selected by discarding the pixels with less than 20 observations and a standard deviation greater than 0.0045 $W/m^2/um/sr$.

3.1.2. Discussion

A map of the brightness temperature created by using this dataset, merged with the Magellan altimetry map, is shown in Figure 3.1. Here, an equirectangular projection is used. A strong negative correlation of the global brightness temperature with the altimetry data can be observed which is shown in Figure 3.2. The altitude range of the observations is limited up to 4km as the observations only cover the Southern hemisphere and the highlands are primarily situated in the Equatorial region (~6-8 km altitude) and Northern latitudes (~11km altitude).

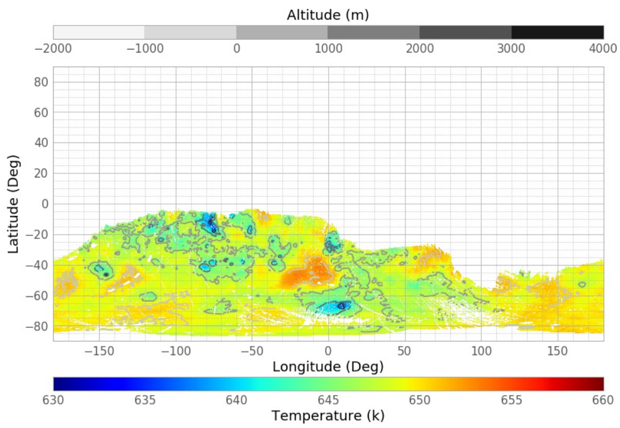

Figure 3.1: Brightness Temperatures retrieved using VIRTIS-M-IR data merged with the Magellan surface topography map. The gray-scale corresponds to topography while colour-scale denotes the temperature (Mueller et al., 2020)

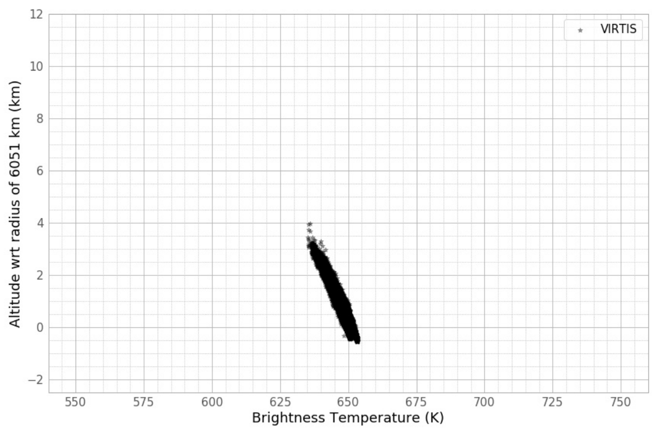

Figure 3.2: The scatter plot of altitude vs temperature based on the brighness temperature map shown in Figure 3.4 (Mueller et al., 2020)

3.2. Akatsuki Observations:

The Akatsuki spacecraft, also known as the Venus Climate Orbiter (VCO), was inserted into an orbit around Venus in 2015 after an orbit insertion failure in 2010 (Nakamura et al., 2016). The new orbit had an apoapsis altitude of 360,000 km, a periapsis altitude of 1000-8000 km, and a period of 10 days 12 hrs. The spacecraft is equipped with five science instruments, out of which two were infrared cameras, known as the 1µm camera (IR1) and the 2µm camera (IR2).

The IR1 camera was designed to investigate the lower part of the atmosphere and the surface on the nightside along with the middle and lower clouds on the dayside. It started taking observations in Dec 2015, however, due to electronic malfunction the data acquisition was stopped in Dec 2016 (Iwagami et al., 2018). The nightside observations are made in three bands (0.9 µm, 0.97 µm, 1.01 µm) and the dayside observations are made in one band (0.9 µm). This is achieved by a six-position filter-wheel with four narrow band interference filters, one shutter, and one diffuser. The standard exposure for the nightside filters was 30.8 sec. Here, three images are taken simultaneously which requires a total time of 92.4 sec for the nightside filters. This introduces a shift in the images taken from distances lesser than 54,000km from the surface of Venus. The final image is generated by taking a median of these three images after an onboard dark subtraction. The detector consists of four quadrants which are read separately. From the three in-flight alignment checks, and unwanted drift in the line of sight is observed. To overcome the error introduced by this drift, the limb-fitting techniques described by Ogohara et al. (2012) are used to generate accurate geometry files for all the observations.

The IR1 observations started on December 07, 2015, with the first observing orbit called r0001. After a malfunction of the electronics on December 07, 2016, the data acquisition was stopped. Thus, the IR1 observations are limited to this period of 1 year around Venus and 34 observing orbits(orbits r0001 to r0034). The observations in the orbits r0001 and r0004 to r0011 were taken by switching off one or two of the four quadrants on the detector. No observations are taken in the 0.9 and 1.01 µm channels from orbits r0012 to r0019. From the orbit r0021 onwards the bright dayside of Venus was pushed outside of the field of view of the camera.

3.2.1. IR1 Data Products

The Akatsuki IR1 dataset which is in the form of imaging observations is available in three levels which are explained below:

- **Level 1:** This level provides the raw data in the form of counts (Unit: ADUs).
- **Level 2:** This level provides the calibrated data in the form of physical values (Unit: mW/cm^2/µm/sr/(ADU/s)). The level name is appended after completing one or a group of processing steps. The suffix 'c' corresponds to the dataset after applying the calibration process shown below.
- **Level 3:** This level provides the equirectangular map projections of the observations using the corrected geometry information given by Ogohara et al. (2017). The suffix of this level corresponds to the suffix of the level 2 data which is being map projected.
- **Geometry Information:** This dataset contains the geometry information (latitude, longitude, emission angle, incidence angle, etc.) for all observations. In Chapter 4 we develop a new process for correction of the noise in the IR1 Level 2c dataset. Then we use this geometry information to manually project the processed observations onto the map of Venus (with 0.5 x 0.5°resolution) and create the corresponding level 3 dataset. To project the observations onto this map, we use the Clough-Tocher 2D interpolator program (Alfeld, 1984, Nielson, 1983).

These three levels of the IR1 data are shown in Figure 3.3 along with the calibration process designed by Iwagami et al. (2018) that is used to generate the level 2c data from the level 1b raw data. This process is shortly described below:

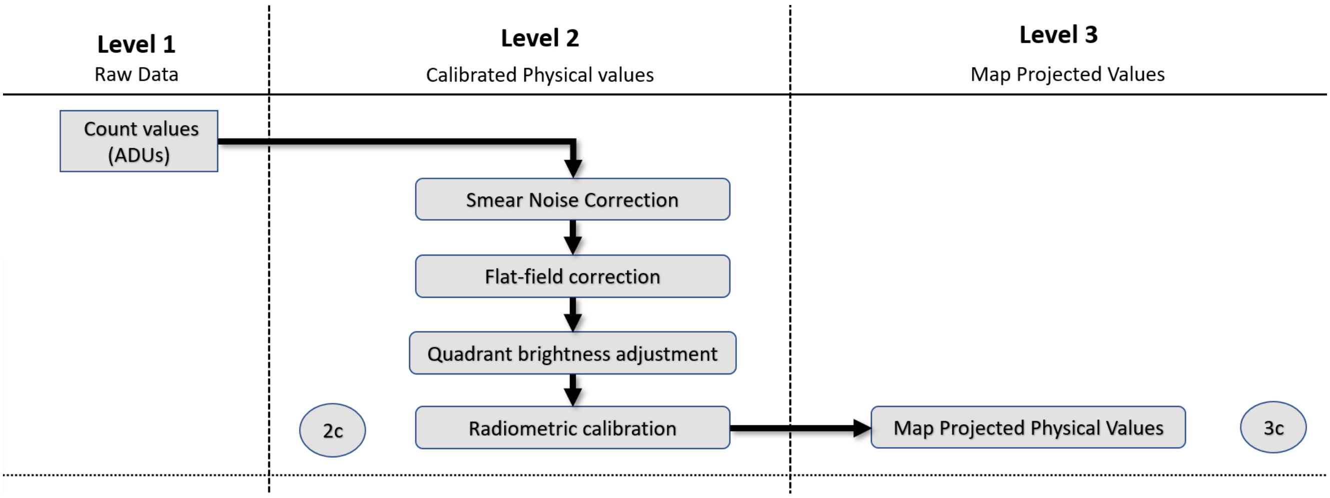

Figure 3.3: The three levels of the IR1 dataset and the calibration process developed by Iwagami et al. (2018) for the IR1 Level 2 data.

1. **Smear noise correction:** During the charge transfer the IR1 camera appears to take an unwanted short exposure that introduces a smear-like noise. This is corrected by subtracting the radiance that is seen in the sky surrounding the Venus disk so that the sky becomes dark. The method described in Iwagami et al. (2018) corrects for the major part of smear noise, however, in many images a gradient can still be observed in the background sky.
2. **Flat-field correction:** The flats taken with the help of the diffuser are available for intermediate orbits. The diffuser obtains the flat field with a spatial scale of 1°, using the dayside of Venus as the light source (Iwagami et al., 2011). However, Iwagami et al. (2018) use four day-side exposures of Venus at 0.9 µm, when the disk of Venus fills the Field of View of the camera and combines them to create a master flat. This approach seems to have worked better.
3. **Quadrant brightness adjustment:** The detector of the IR1 imager is divided into four quadrants which are read separately. At the boundaries of these quadrants, some discontinuity can be observed in the image, which might be due to slightly different gains during readout or secondary effects from the smear noise. Murakami et al. (2018) provides a correction method for this by introducing a relative sensitivity correction process for every quadrant.

While this effect is prominently seen in the dayside images taken at 0.90 µm, the nightside images are not much affected. Hence, this correction is applied only to the dayside images.

4. **Radiometric calibration:** Iwagami et al. (2011) utilized laboratory measurements for radiometric correction, however, due to the presence of smear noise, this calibration was no longer valid. Thus, Iwagami et al. (2018) use observations of six stars to calculate sensitivity coefficients for all the four channels of IR1 imager. For 1.01 µm channel, this coefficient is 1.35±0.91 $\mu W/cm^2/\mu m/sr/(ADU/s)$, where ADU is analogue to digital conversion unit. Because of the large uncertainty (±67%) of the sensitivity coefficient, a new calibration procedure is required.

3.2.2. Discussion

The additional time spent in space due to the orbit insertion failure could have resulted in a degradation in the quality of the camera by increasing the number of dead pixels. Fortunately, such degradation was not observed in the images. While the dayside observations during the initial period provided good contrasts, the nightside observations in all the filters were contaminated by the bright dayside of Venus. The reason for this contamination was the electric charge overflowed from the bright dayside of Venus into the nightside on the sensor. To avoid this a procedure was applied after July 21, 2016, which required specific planning to push the dayside of Venus out of the field of view of the IR1 Camera.

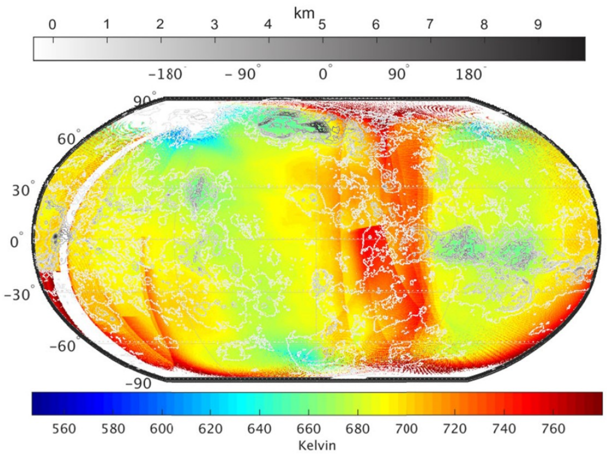

Figure 3.4: Brightness Temperatures retrieved using IR1 data merged with the Magellan surface topography map. The gray-scale corresponds to topography while colour-scale denotes the temperature (Singh, 2019)

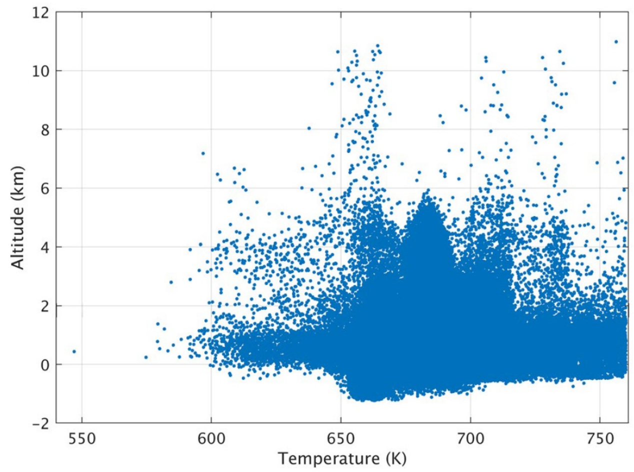

Figure 3.5: The scatter plot of altitude vs temperature based on the surface temperature map shown in Figure 3.4 (Singh, 2019)

Singh (2019) analyzed the observations and reported that the observations earlier than 16th July are washed out due to contamination from the light coming from the dayside. He used the observations from 16 July 2016 to 7 Dec 2016, to create a map of brightness temperatures merged with the Magellan topography map which is shown in Figure 3.4. This map was created by binning the data into 0.5°x 0.5°sized bins. It is evident from the scatter plot of brightness temperature versus altitude, shown in Figure 3.5, that no conclusive relationship can be observed between the two as opposed to that observed from the VIRTIS data (Figure 3.2).

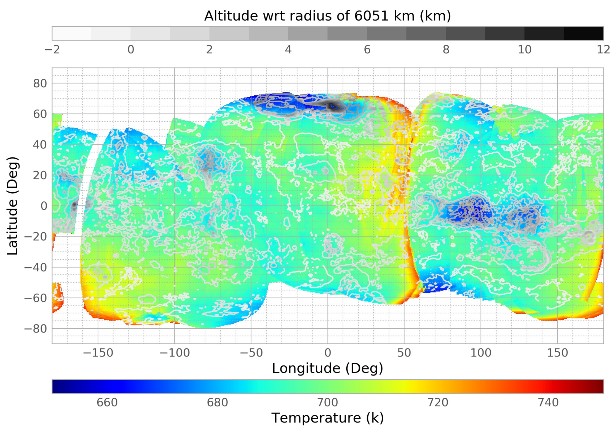

Figure 3.6: Brightness Temperatures from the IR1 data. The colour-scale denotes the temperature while the gray-scale corresponds to topography from the Magellan Altimetry database

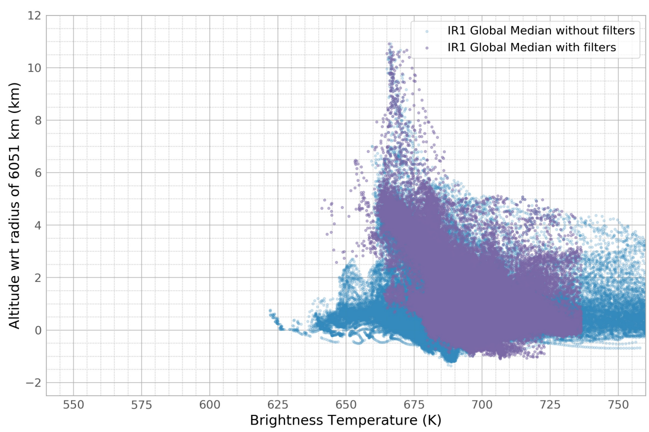

Figure 3.7: The scatter plot of altitude vs temperature based on the surface temperature map shown in Figure 3.6

While generating all the global altitude vs radiance scatter plot in our study, we use the following procedure:

1. Apply the required processing steps on the level 2 data.
2. Convert the data into level 3 data, by projecting onto an equirectangular map with 0.5 x 0.5° resolution (similar to Singh (2019)).
3. Take median of the level 3 data set to generate the global map as shown in Figure 3.6.
4. Use the Magellan topography map (binned to 0.5 x 0.5° resolution) to generate the scatter plot altitude vs radiance.

We selected the observations in a similar way as Singh (2019) and the resulting altitude vs radiance scatter plot is shown in Figure 3.7 by the blue dots. As opposed to Figure 3.5, we can observe some negative correlation between altitude and radiance apart from the effects induced by straylight and limb-darkening. We then apply the following additional limits while processing the data:

1. Upon inspection, it is found that even the observations from 16 July 2016 to 7 Dec 2016 also contain some part of the bright crescent of Venus. This introduces stray light of a magnitude that is still severe for our computations. Thus, to reduce the effect of this stray light, an upper limit of 0.05 $\mu W/cm^2/\mu m/sr$ is applied to all the observations.
2. Similar to the processing of VIRTIS data, a lower limit of 100° is applied to the incidence angle which removes the pixels in the twilight zone and an upper limit of 70° is applied to the emission angle which removes the pixels that are highly affected by the limb-darkening.

The map of brightness temperatures merged with the Magellan topography map (Ford and Pettengill, 1992) created by using the above processing steps is shown in Figure 3.6. From the scatter plot shown by violet dots in Figure 3.7 a weak dependence of the brightness temperature on the altitude can be observed which is completely different from Figure 3.5. However, the values of brightness temperature and the slope of the data are still different than those produced from the calibrated VIRITS data (Figure 3.2). Also, the standard deviation of the IR1 data is more as compared to that with VIRITS data. Thus, it can be concluded that, in spite of the procedure to push the dayside out of the field of view, observations are still contaminated and the effect of this contamination cannot be mitigated by using the simple processing steps mentioned above. Given that the IR1 observations contain the high-lands, e.g., Aphrodite Terra and the Maxwell Monts, they are important for our study. Thus, the contamination present in the observation is first studied which is discussed in Section 4.2. To make use of the IR1 observations, additional processing steps and a new calibration method is designed which is explained in Section 4.3.

4

Data Processing

In the previous chapter, we observed that the IR1 nightside data is highly contaminated. The primary reason for this contamination is the charge overflowed from the bright dayside of Venus to the night side on the sensor. Although, a special procedure was applied from orbit r0021 onwards to leave the dayside out of the field of view of the camera we observe that a small part of the dayside is still present in these images which affects the observations. In this chapter, we first study and delineate the effect of the stray light coming from the dayside in Section 4.2. Then develop a data processing pipeline to minimize this effect in Section 4.3. We also show that the observations taken in orbits earlier than the r0021, which were not used by Singh (2019), can be made useful by using this new pipeline. Lastly, a new radiometric calibration procedure is set up in Subsection 4.3.5.

4.1. Selection of the Data

The observations in the Akatsuki dataset are organized by the orbits in which they were taken. No observations were taken in the 0.9 and 1.01 μm filters from orbits r0001 to r0003 and r0012 to r0019. The observations in the orbits r0004 to r0011 were taken directly looking at the complete disk of Venus. In this method, the quadrants containing the bright crescent of Venus were overexposed and got saturated. Also, the charge overflowed into neighboring quadrants resulting in a heavy noise. These observations are here termed as **Type I** observations. The examples of the extreme cases of Type I observations are shown in Figure 4.1. Such extreme cases are heavily affected and are not used in our analysis. The Type I observations were reported to be highly contaminated for the use by Singh (2019) and were not used in their analysis.

From the orbit r0021 onwards the bright dayside of Venus is left outside of the field of view of the camera. This method reduces the stray light and slightly better observations are obtained. These observations are termed as **Type II** observations. Combined both the types, a total of 45 observations are used in our analysis which are listed in Section C.1

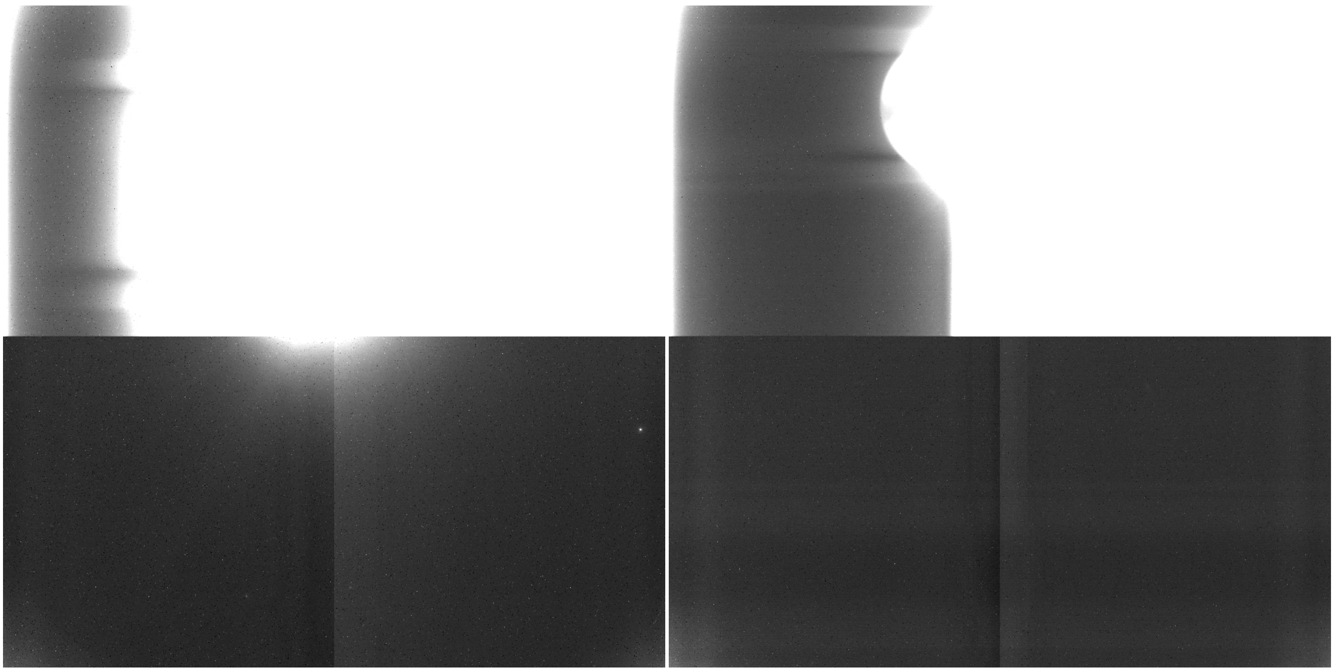

Figure 4.1: Example observations by the IR1 camera (Murakami et al., 2018) that are severely affected by the stray light

4.2. The contamination present in the calibrated IR1 Data

Before discussing the contamination, we identify the best or the least affected observation out of the 45 observations discussed above. This observation will be used as a reference to identify the different types of noises. A plot of observation

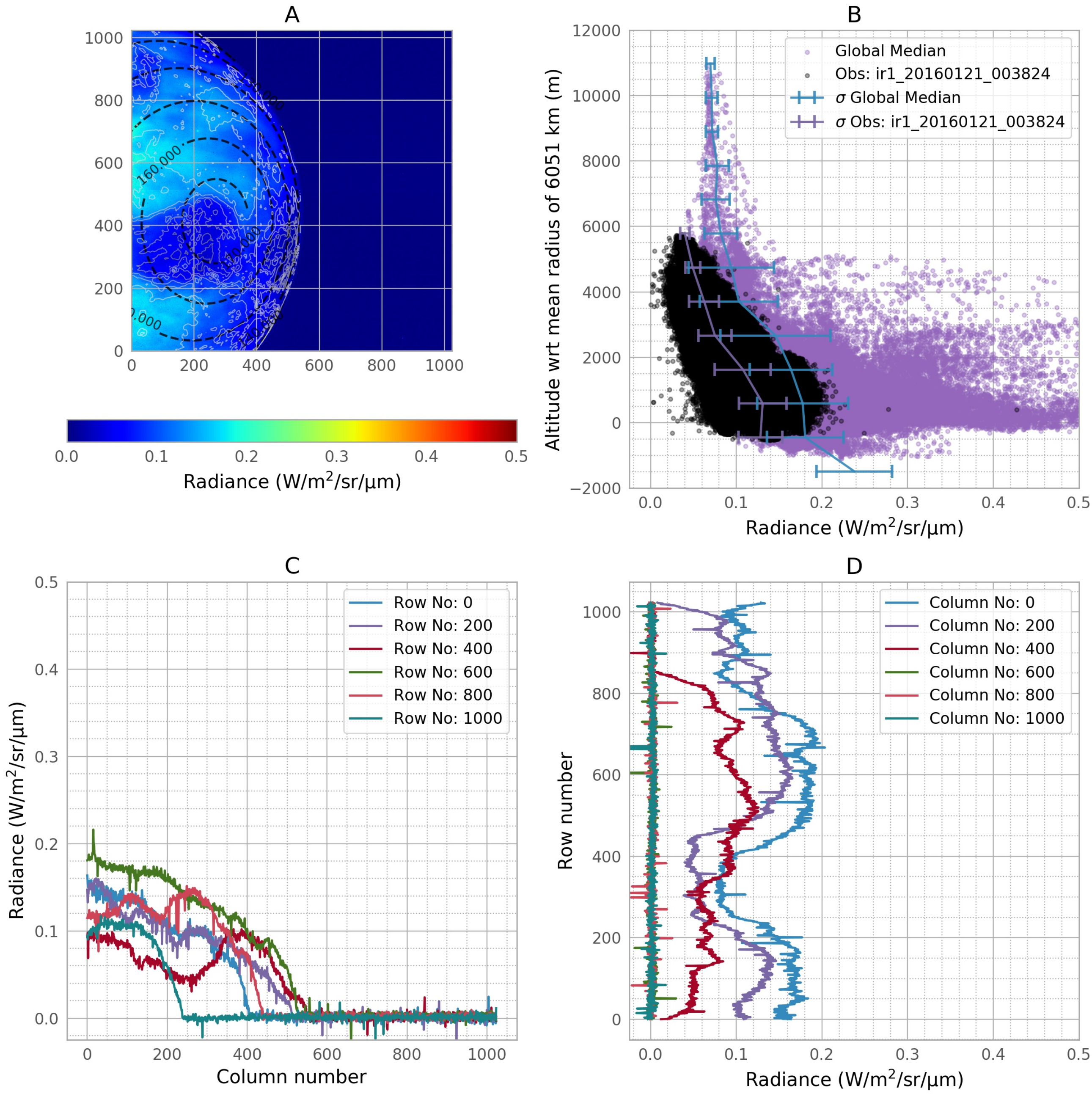

Figure 4.2: (A) The plot of the observation ir1_20160121_003824_101, the dashed lines indicate the contours of incidence angle, the solid white-grey lines show the topography features on the surface of Venus, (B) The black scatter points show the corresponding altitude vs radiance scatter plot on top of the global median scatter plot of level 2c dataset, (C) Shows the line plot of five rows in the image shown in (A), similarly (D) the line plot of five columns. It should be noted that the radiance scale is same for all the plots (0.0-0.5 W/m^2/sr/µm)

- ir1_20160121_003824_101 along with the topography (solid) and incidence angle contour lines (dashed) is shown in Figure 4.2(A). This observation covers only the region of the nightside which has incidence angles greater than 120°and does not contain any region from the bright dayside of Venus. Any secondary reflections from the dayside are also not observed. Thus, there is no indication of any straylight in this image. Figure 4.2(C) and (D) show the plot of the radiances in five rows and columns from this image. From these plots, a clear distinction can be observed between the disk of Venus and the sky. Also, the brightness of pixels observing deep space is within the noise level indistinguishable from zero. Figure 4.2(B) shows the scatter plot of altitude vs radiance obtained from this observation as compared to the global median plot shown in the Figure 3.7. It can be observed that this observation shows lower radiances at all altitudes as compared to the global median. This is due to the absence of effects associated with the stray light. Based on these factors we define this observation as the best observation in this dataset.

All remaining observations show varying amounts of noise due to the stray light. After careful observation, it is found that the conditions at the time of observation affect the type and the amount of noise introduced due to the stray light. Thus, we study the effect of the stray light separately for both the types of observations discussed in the previous section.

Subsection 4.2.1 talks about the noise in the Type I observations that are taken by directly looking at the disk of Venus (i.e. before the orbit r0021). The noise in the Type I observations that are taken by pushing the bright dayside of the Venus outside the FOV of the camera is explained in Subsection 4.2.2.

4.2.1. Type I Observations

As discussed above, this method was used for the observations before r0021 orbit and it introduces a heavy noise in the images. A typical example of this is the observation - ir1_20160131_152121 and it is shown in the Figure 4.3. While taking this observation the upper and lower left quadrants got saturated observing the bright crescent of Venus (from incidence angle 70 to 90). These quadrants are overexposed as shown in Figure 4.3(A).

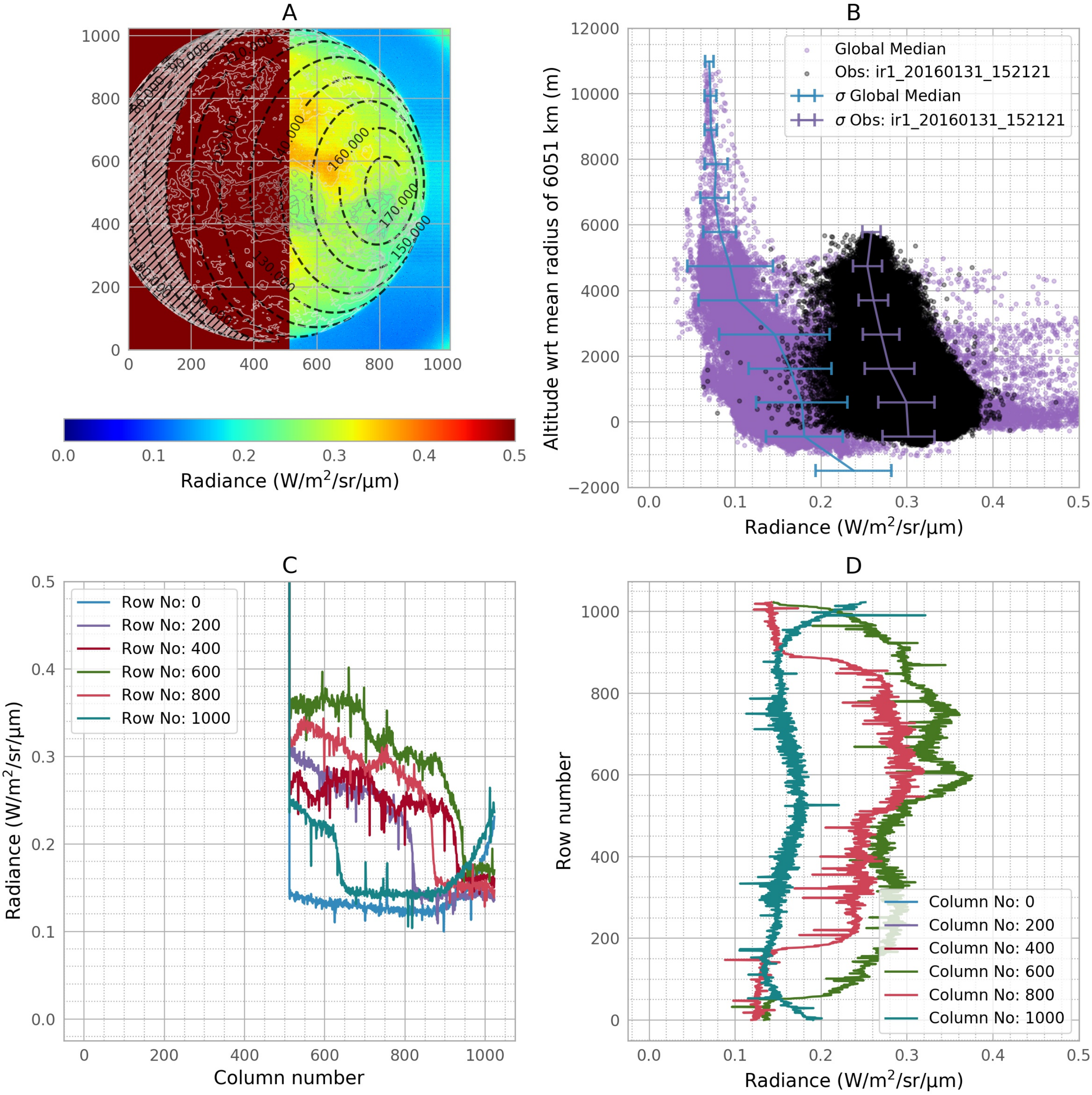

Figure 4.3: (A) The plot of the observation ir1_20160131_152121, the dashed lines indicate the contours of incidence angle, the solid white-grey lines show the topography features on the surface of Venus, (B) The black scatter points show the corresponding altitude vs radiance scatter plot on top of the global median scatter plot of level 2c dataset, (C) Shows the line plot of five rows in the image shown in (A), similarly (D) the line plot of five columns. The radiance scale is same for all the plots (0.0-0.5 $W/m^2/sr/\mu m$)

Figure 4.3(B) shows a clear offset between the global median scatter plot and the scatter plot from the observation. Similarly, from Figure 4.3(C) and (D), a significant amount of the radiance can be observed in the sky. Based on this it can be concluded that a heavy bias was imposed onto the entire image which affected both the disk and sky portions of the image. A possible reason for this could be the charge transfer from the area on the sensor corresponding to the day-side to the other parts of the image. Careful observation of Figure 4.3(A) shows groups of rows that are alternatively bright and dark. From this, it appears that this type of noise is also transferred horizontally along a row as opposed to the smear noise which appears in the form of vertical smears.

From Figure 4.3(D) a gradient can be observed in the sky with a maximum value in the middle of the image (row 512) which decreases as we traverse towards the outer edges (row 0 and 1024). We term this as a first-degree noise which can be represented by a linear relation. Similarly, the bias is termed as zeroth degree noise. Apart from these two effects, a presence of a small non-linear component is indicated by the large scatter of the radiances at all the altitudes from the Figure 4.3(B). Lastly, vignetting effect (increased brightness near the corners of the image)is also observed from Figure 4.3(A), (C), and (D), however, this does not directly affect the disk part of the image. A procedure to correct for these effects by using the sky brightness is discussed in Section 4.3.

4.2.2. Type II Observations

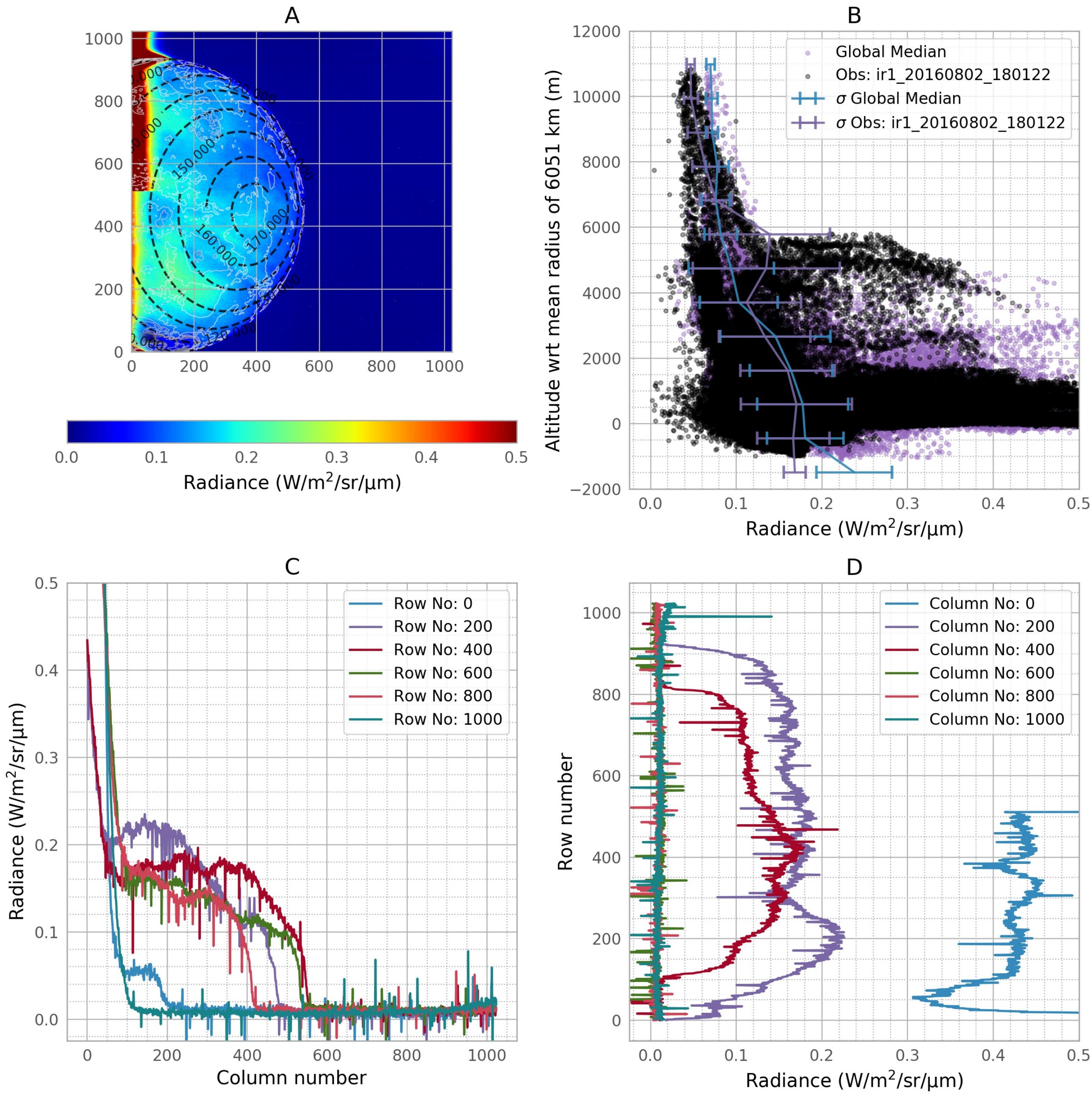

Figure 4.4: (A) The plot of the observation ir1_20160802_180122_101, the dashed lines indicate the contours of incidence angle, the solid white-grey lines show the topography features on the surface of Venus, (B) The black scatter points show the corresponding altitude vs radiance scatter plot on top of the global median scatter plot of level 2c dataset, (C) Shows the line plot of five rows in the image shown in (A), similarly (D) the line plot of five columns. It should be noted that the radiance scale is same for all the plots (0.0-0.5 W/m^2/sr/µm)

This type of observation was used from orbit r0021 to avoid the presence of the bright dayside of Venus in the field of view of the camera. However, it was not fully successful and a small part of the bright dayside was still present in all of the observations. Apart from this, secondary reflections of the bright crescent were also introduced onto the sensor. This had a severe effect on all of the observations which introduced nonlinear noise varying as per the amount of dayside and/or the intensity of the secondary reflection present in the image.

For example, the Figure 4.4(A) shows the plot of the observation - ir1_20160802_180122_101 which was the first observation taken in 1.01 µm filter after this correction procedure was applied. However, from Figure 4.4)(A), it can be observed that a small part of the bright crescent and the twilight zone (incidence angle < 100°) was still present in the lower and upper left corners (area filled by white colour with black hatching lines). This resulted in a heavy vertical charge transfer which over-exposed the first few columns (from the left side) rendering them completely useless. From these affected columns a horizontal charge transfer can be observed. However, the effect is more problematic as compared to that observed in Subsection 4.2.1 given the proximity of the affected area with the useful observations. The horizontal charge transfer introduces a noise that is nonlinear in nature and affects the pixels in the close vicinity of the affected columns. The effect decreases non-linearly as we traverse away from the affected columns (Figure 4.4(C) and (D)). Given that this effect is non-linear a direct estimation is difficult. The altitude vs radiance scatter plot (Figure 4.4(B)) shows the severity of this effect which results in the horizontal spread of the data along the positive X-axis (increase in radiance) for all the altitude levels as compared to the global median. Apart from this non-linear effect, the linear effect and a small bias (discussed in Subsection 4.2.1) are also observed in small amounts from Figure 4.4(B), (C), and (D).

4.2.3. Summary

In summary we identify a total of four types of noises that are present in the level 2c dataset which are highlighed below:

1. **Bias:** The stray light from the day side of the Venus imposes a uniform bias on the entire image. This is denoted in Equation 4.1 by Ba.
2. **Linear effect:** While a column-wise correction has been already applied to the level 2c database in the form of smear-noise correction, a vertical gradient is still observed in the sky part of the image. This is denoted by L_y.
3. **Non-linear effect:** A non-linear effect is prominently observed in the Type II observations in vicinity of the bright crescent and the affected area. This is denoted by $NL_{x,y}$
4. **Vignette:** Vignetting is another non-linear effect observed in the sky of some observations, however, it does not appear to be affecting any parts of the disk in those observations. This is denoted by $V_{x,y}$

$$N_{x,y} = NL_{x,y} + L_y + Ba + V_{x,y} \tag{4.1}$$

The total noise ($N_{x,y}$) present in an observation is given by Equation 4.1. The contribution from the three main sources varies as in all the observations and thus, an adaptive procedure is developed for accurate estimation and subsequent removal of the noise which is explained in the next section.

4.3. Processing of the IR1 Data

We develop a new procedure to correct for the above-discussed noise which is shown in Figure 4.5. In this figure, the circles indicate the level of the dataset after applying the mentioned processing step. Here, we first recreate the level 2c dataset from the level 1b dataset by using the process set up by Iwagami et al. (2018) which is described in Subsection 3.2.1. Then we use this level 2c dataset to apply the new correction steps which are described in the next subsections. The level of the dataset is appended at every step from 2c to 2h. The corresponding map projections of the dataset (level 3c to 3h) are used to generate the global median scatter plots. The colours of individual levels shown in Figure 4.5 indicate the colours used for the corresponding altitude vs radiance scatter plots shown in Figure 4.7 to Figure 4.11.

4.3.1. Sky brightness correction (Level 2d, 3d)

As discussed in the earlier section, the linear effect appears in the form of a vertical gradient in addition to the bias. These effects are particularly noticeable in the sky part of the image. Thus, we design a sky-brightness correction procedure, in which first the sky is extracted from the image. Then the median of an individual sky row is calculated and subsequently subtracted from all the elements of that row (the disk and the sky). This procedure is repeated for all rows of the image. The magnitude of sky radiance obtained after this correction is found to be sufficiently less as compared with the level 2c database. Also, a similar correction for all the columns has been already applied to the level 2c database in the form of smear-noise correction (Subsection 3.2.1). Thus, another column-wise sky brightness correction is not applied. The database after applying this correction is termed as **level 2d** database.

The effect of applying the sky brightness correction on the type - I observation, ir1_20160131_152121, is shown in Figure 4.6. By comparing with Figure 4.3, a significant change in the sky can be observed which leads to near-zero values for

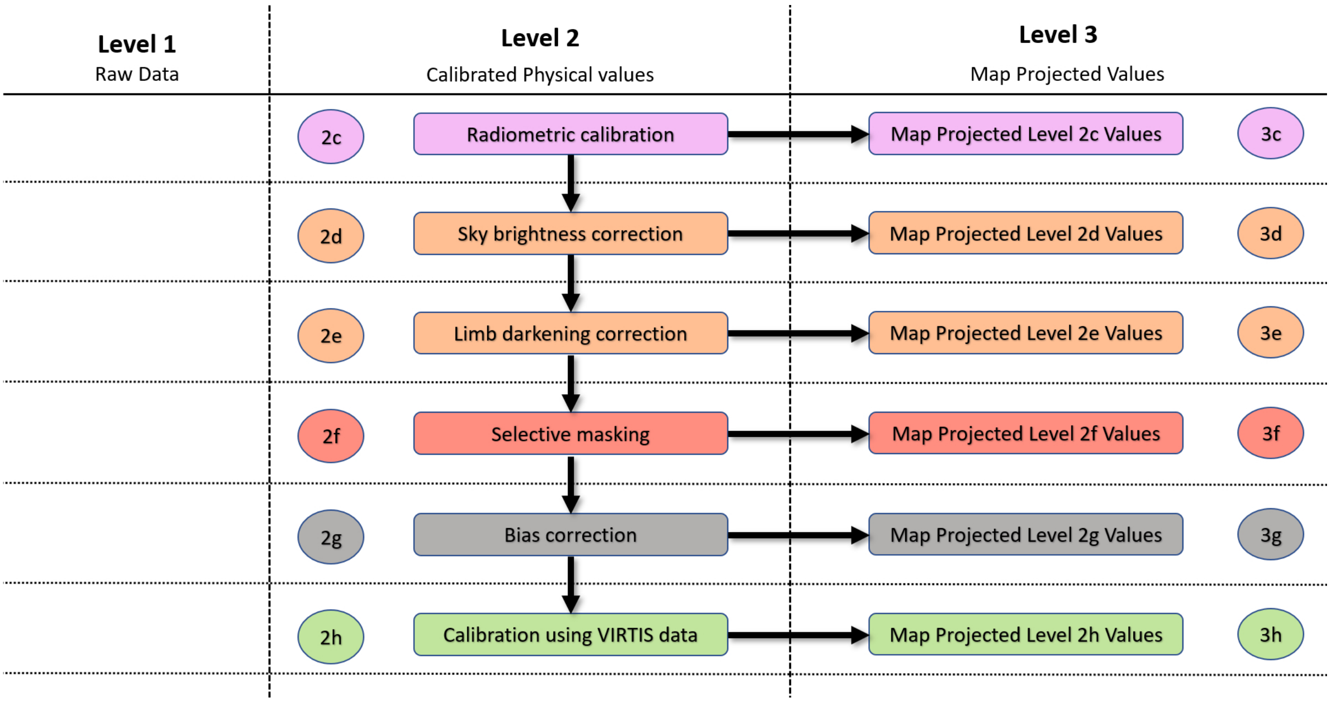

Figure 4.5: Flowchart of the new data processing pipeline. The values given in the circles indicate the level of the dataset after completing the corresponding processing step. The colours of individual levels are consistent with the colours used for the corresponding altitude vs radiance scatter plots shown in Figure 4.7 to Figure 4.11.

most of the sky region. Although the vignetting can still be observed in the sky, it does not affect the radiance values of the disk and thus, remains uncorrected.

4.3.2. Limb darkening correction (Level 2e, 3e)

For the Venusian atmosphere, the extinction scale height in the uppermost cloud layer primarily governs the observed limb darkening. Various cloud retrieval studies state that the major source of cloud variability is located in the lower cloud decks (Esposito et al., 1997, Grinspoon et al., 1993, Ragent et al., 1985, Titov et al., 2018). While we vary the particle number density in the lower cloud decks, the cloud top altitude is kept constant in our model of the atmosphere (Subsection 5.2.3). Thus, the modelled limb darkening remains constant in our atmospheric radiative transfer model.

We use the synthetic limb darkening function ($P(\xi)$) from Mueller et al. (2009) given in Equation 4.2. This function is governed by ξ which represents the cosine of the emission angle. Next, we correct the observed radiances ($I(\xi)$) at each pixel by dividing them by limb darkening function $P(\xi)$ calculated at corresponding cosine of emission angle ξ to get the nadir radiances ($I(1)$) as given by Equation 4.3 (Mueller et al., 2009). Further, the filters of incidence angle, emission angle, and maximum radiance (described in Subsection 3.2.2) are now embedded into the database. While doing so the sky part of the observations is also removed and the database now represents only the useful part of the disk. The database after applying these corrections is termed as the **level 2e** database.

$$P(\xi) = 0.31 + 0.69\xi \tag{4.2}$$

$$I(1) = I(\xi)/P(\xi) \tag{4.3}$$

A comparison of the altitude vs radiance scatter plots of the IR1 global median of level 3c and 3e databases is shown in the Figure 4.7. This comparison is important as the global median plots indicate the quality of the entire dataset. The scatter points belonging to the altitudes higher than 6 km correspond to the region of Maxwell montes which is typically observed at a higher emission angle (50 -70 °) and thus, is highly affected by the limb darkening. Thus, the shift of radiance after limb darkening correction can be most prominently observed for the higher altitude regions in Figure 4.7.

4.3.3. Selective masking (Level 2f, 3f)

The non-linear effect discussed in Subsection 4.2.2 is more difficult to correct. This noise affects all the pixels in the vicinity of the bright crescent and the corresponding affected columns. A simple way to remove this noise could be to directly use a maximum radiance filter. However, as it can be observed from Figure 4.4(C) and (D), the effect has a different magnitude in each row, thus, a row-wise maximum radiance filter would be required. But, in some parts of the image,

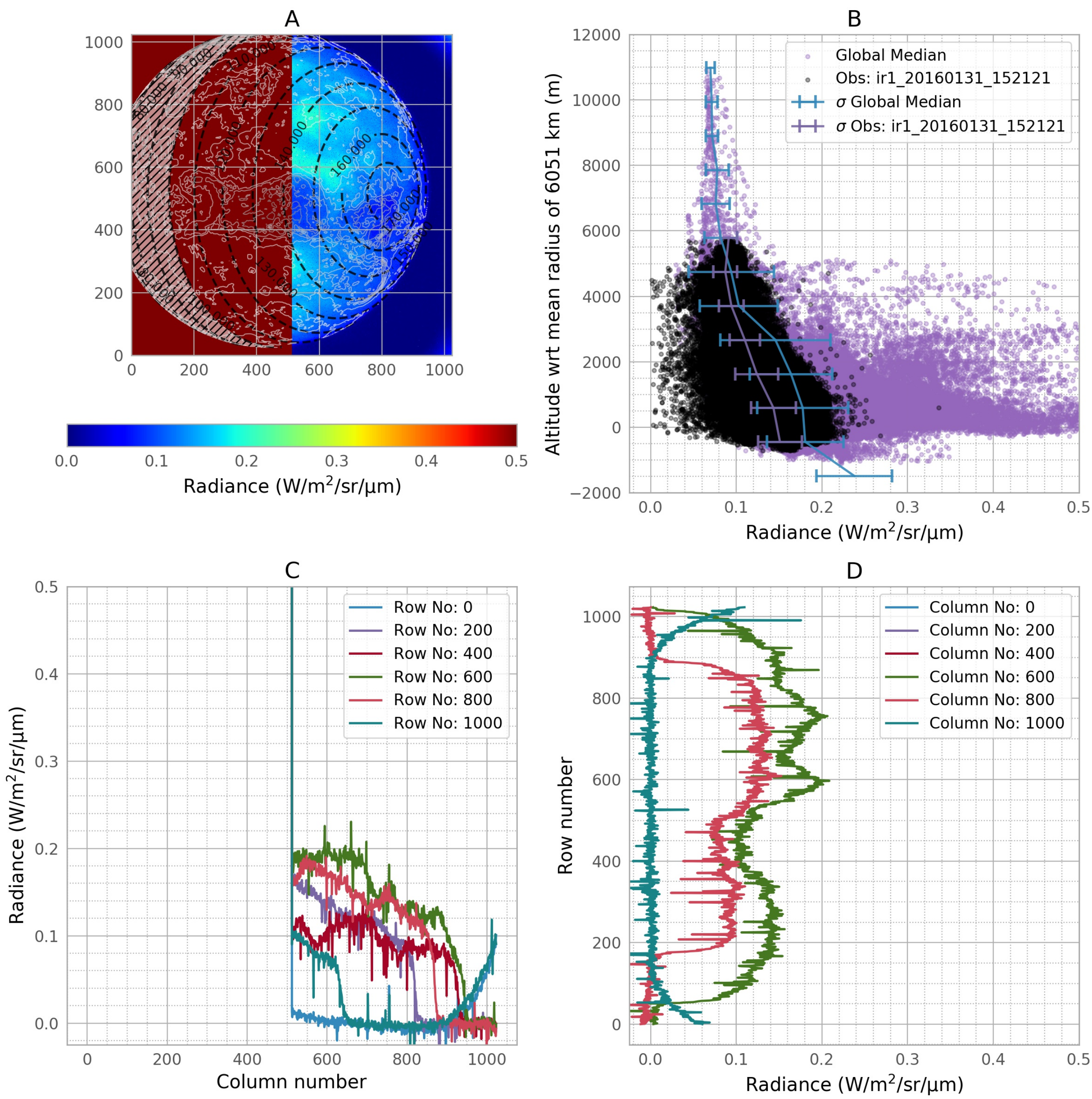

Figure 4.6: (A) The plot of the observation ir1_20160131_152121, the dashed lines indicate the contours of incidence angle, the solid white-grey lines show the topography features on the surface of Venus, (B) The black scatter points show the corresponding altitude vs radiance scatter plot on top of the global median scatter plot of level 2c dataset, (C) Shows the line plot of five rows in the image shown in (A), similarly (D) the line plot of five columns. The radiance scale is same for all the plots (0.0-0.5 $W/m^2/sr/\mu m$)

the areas corresponding to affected pixels belong to high-lands and thus have lower radiances than those belonging to low-lands. This affects the estimation of maximum radiance value for the particular row, and thus, such a filter cannot be used.

Thus, we opt for a manual method in which first the affected areas of the image are carefully studied and subsequently masked out. While selecting the affected area manually it is possible that we also reject a small part of the unaffected data. However, this method is found to give the best results after extensive experimentation. The database after applying this correction is termed as the **level 2f** database.

The effect of applying this correction on the type - II observation, ir1_20160802_180122_101, is shown in Figure 4.9. Figure 4.9(A) shows the useful part of the image which remains after applying the mask on the affected area. Also, the sky region, and the part of the disk below 100°incidence angle and above 70°emission angle have been already removed in the earlier processing step (Subsection 4.3.2). This is why the row and column plots ((C) and (D)) shown in earlier figures are no longer needed. Comparing the Figure 4.9(B) with Figure 4.4(B), the combined effect of applying sky-brightness, limb darkening correction, and masking can be directly observed. Figure 4.8 compares the altitude vs radiance scatter plot of

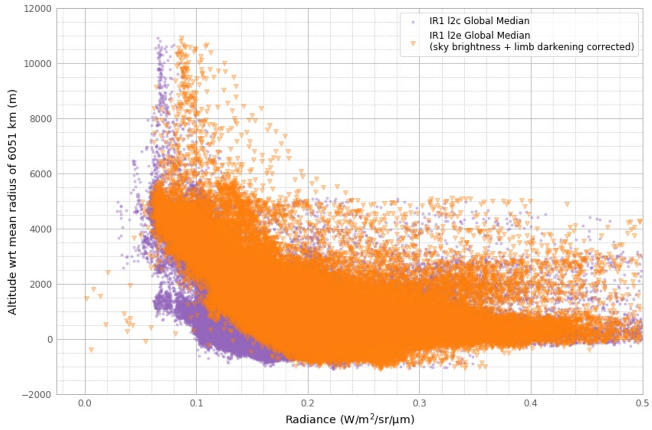

Figure 4.7: The scatter plots of altitude vs radiance of level 3c dataset (violet dots) and level 3e dataset (orange triangles)

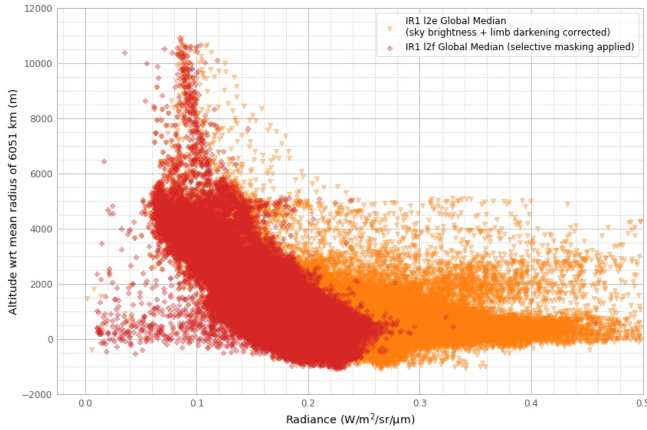

Figure 4.8: The scatter plots of altitude vs radiance of level 3e dataset (orange triangles) and level 3f dataset (red diamonds)

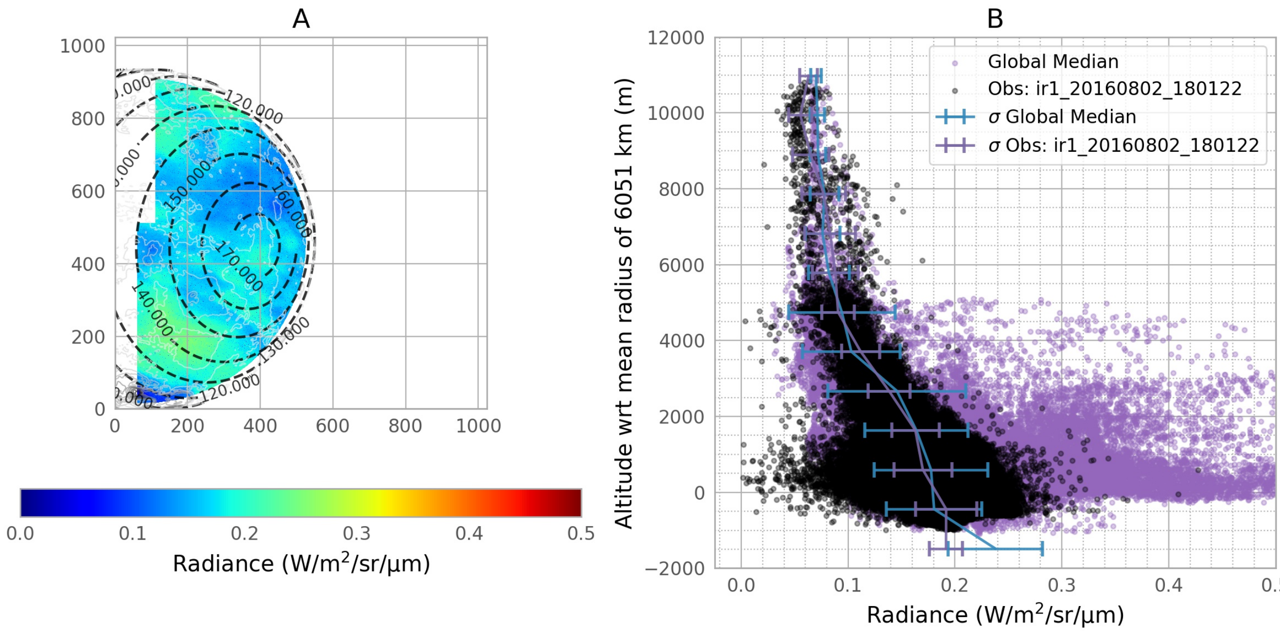

Figure 4.9: (A) The plot of the observation ir1_20160802_180122_101 (level 2f), the dashed lines indicate the contours of incidence angle, the solid white-grey lines show the topography features on the surface of Venus, (B) The black scatter points show the corresponding altitude vs radiance scatter plot on top of the global median scatter plot of the level 3c dataset. The radiance scale is same for all the plots (0.0-0.5 $W/m^2/sr/\mu m$)

the global median of the level 3e and 3f databases. The horizontal streaks of the scatter points which are mainly caused due to the noise induced by stray light are now removed from the dataset and only the useful data remains.

As discussed above, we apply masks on the data to generate the level 2f dataset. These masks have sharp edges that are parallel to the (x and y axes) edges of the image. When this masked data with sharp edges are projected on the map of Venus to generate the level 3f dataset the noise appears around the border of the projected data. In this study, we term this noise as the 'interpolation noise'. In the lower left corner of Figure 4.8, some loose scatter points can be observed that were not present earlier in Figure 4.7 which are attributed to the interpolation noise. These points are a result of the interpolation procedure (discussed in Subsection 3.2.1 and Subsection 3.2.2). As discussed in Section 6.2, this noise does not have any major effect on the results.

4.3.4. Bias correction (Level 2g, 3g)

The sky-brightness correction (Subsection 4.3.1) corrects for most of the bias induced on the images, however, after careful observation of the altitude vs radiance scatter plots of individual observations, some offset is still observed between various observations. For the observations during the same orbit, thus having the same cloud features, and containing the same surface features, e.g. the Maxwell montes or the Aphrodite terra, this offset is not expected. Such offset between observations of the same region but in different orbits is also not expected given the high thermal inertia of the deep atmosphere of Venus Limaye et al. (2018a). The offset indicates the presence of a residual bias in the image which is still present after the sky-brightness correction. In the scatter plot of level 3f (red diamonds) shown in Figure 4.8, the stream of the data points above 6 km altitude appears to be shifted towards the higher radiance side and the 5-6km altitude range shows lower radiance values than the higher altitudes, e.g. 10 km. This is primarily caused by the residual bias in the images.

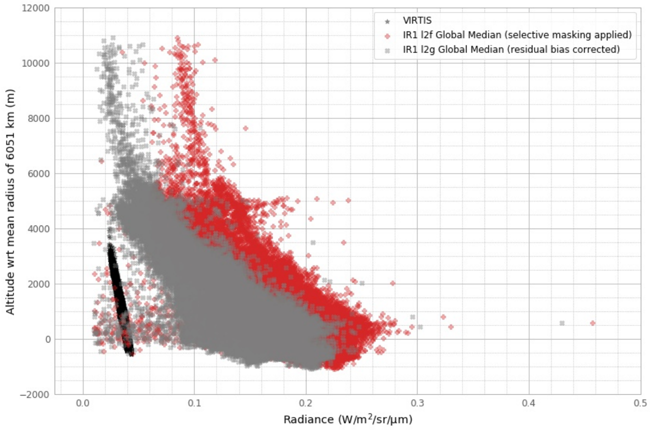

Figure 4.10: The scatter plots of altitude vs radiance of level 3f dataset (red diamonds), level 3g dataset (grey crosses), and VIRTIS dataset (black stars)

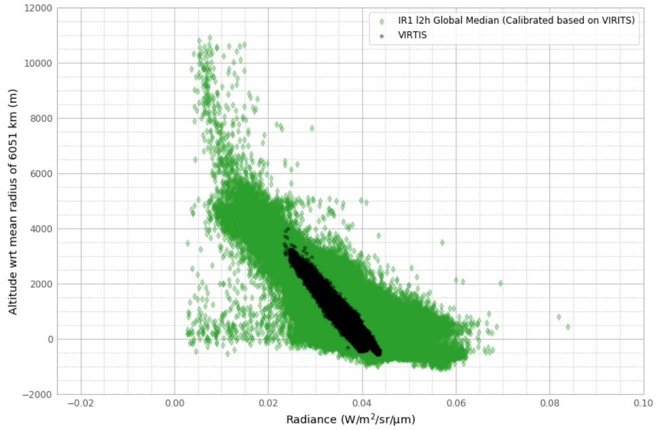

Figure 4.11: The scatter plots of altitude vs radiance of calibrated level 3h dataset (green diamonds) and VIRTIS dataset (black stars)

Thus, we design a procedure to correct the dataset for the residual bias. The observation - ir1_20160121_003824_101 which is the least affected observation of the dataset (Section 4.2) is used as the reference. In this procedure, we first bin the data of the individual observations into altitude intervals of 1 km. Now, a median is calculated for all the altitude bins. The violet line shown in the (B) part of Figure 4.2, Figure 4.3, Figure 4.4, Figure 4.6, and Figure 4.9 shows the trend-line generated by taking a median of the data binned in the altitude intervals of 1 km along with the standard deviation of each bin. Next, the difference between the corresponding altitude bins of the reference observation and the observation under consideration is found out. A median value of this difference is termed as the bias correction offset for the observation under consideration which is then subtracted from all of the images.

We use the median value of the difference of the altitude bins which ensures that extreme values of the difference are avoided which arise for the highly affected observations which are characterized by the horizontal spread of the scatter points at a given altitude. Furthermore, a single correction offset is subtracted from the entire observation at all the altitude levels which ensures that the altitude vs topography relation is still preserved after applying this correction.

The scatter plot of the global median of Level 3g database (shown by the grey crosses in Figure 4.10) serves as an indicator of the quality of the entire dataset. The database now has a lower standard deviation at all the altitudes and what appeared to be different branches in the level 3f dataset now line up. The branch extending up to 10 km is now lining up with the bulk of the data. Similar to the level 3f dataset, the presence of interpolation noise can be observed near the lower-left corner of Figure 4.10.

4.3.5. Calibration of the IR1 Data (Level 2h, 3h)

From Figure 4.10 it can be observed that the IR1 radiances are still several times higher than that from the processed VIRTIS dataset. The likely reason for this is the uncertainty of ±67% in the radiometric sensitivity coefficient as mentioned in Subsection 3.2.1. Thus, we need a new calibration procedure to make use of the IR1 data.

We develop a procedure to calibrate the IR1 dataset by using the processed VIRTIS dataset. In Subsection 4.3.4 we used the observation - ir1_20160121_003824_101 as a reference to correct for the residual bias in the dataset. Similarly, we use this observation as a reference to calculate a new calibration coefficient. First, the VIRTIS dataset and the ir1_20160121_003824_101 are binned into the altitude intervals of 1 km. Then we divide the altitude bins of the VIRTIS dataset by the corresponding altitude bins of ir1_20160121_003824_101. Next, we take a median of this division which serves as the calibration coefficient for the entire dataset. In the last step, we multiply the entire IR1 dataset by this calibration coefficient which completes the calibration of the dataset. The value of the calibration coefficient comes out to be 0.2772. After applying this procedure, the dataset is termed as **level 2h** dataset.

It should be noted that the central wavelength of the observations from the IR1 camera is 1.008 μm with an FWHM of 40 nm (Iwagami et al., 2011). However, the VIRTIS band-1 observations have a central wavelength of 1.017 μm with an FWHM of 15.75 nm (Mueller et al., 2020). Although both of the central wavelengths occur on the same flank of the 1 μm window, the magnitude of radiances observed are slightly difference. For the current study, we are directly calibrating the IR1 observations using VIRITS observations and later we use the central wavelength of VIRITS to find out the surface temperatures from the IR1 dataset. Another approach could be to find out the scaling factor between the convoluted radiances at the two mentioned central wavelengths and further adjust the IR1 dataset. In this case, the central wavelength of the IR1 dataset should be used to find out the surface temperatures. However, as discussed in Subsection 6.1.1 the results from the atmospheric radiative transfer model (Chapter 5) show that the radiances at the two wavelengths have almost the same ratio at all altitudes, so that the first approach is sufficiently accurate.

The comparison of the level 3h dataset with the VIRTIS dataset is shown in Figure 4.11. It can be observed that the IR1 dataset is now within the same magnitude range as that of the VIRTIS database. While the VIRTIS dataset shows more of a linear trend, the IR1 dataset shows a non-linear trend which is predicted by the radiative transfer simulations (Section 5.3). As mentioned in Subsection 3.1.2, the VIRTIS dataset was corrected for cloud variations by using the simultaneous observations in the 1.31 μm window and such correction was not possible for the IR1 dataset. Thus, While we have minimized the noise emerging due to the stray light, the standard deviation of the IR1 dataset is still higher than that of the VIRTIS dataset which is due to the lack of correction for localized cloud optical thickness variations.

4.4. Discussion

While the VIRTIS dataset covers the Southern hemisphere of Venus, the surface altitude range in this region is limited to 3.5 km. The IR1 dataset covers the equatorial region which includes high-lands like the Aphrodite Terra, Maat Mons, and the Ishtar Terra in the North. Thus, the IR1 dataset is essential for our study to generate the surface temperature vs. altitude relation above 3.5 km. However, as reported by Iwagami et al. (2018) and Singh (2019), the dataset is heavily contaminated and also has an uncertainty of ±67% in calibration. In order to study the effect of the contamination, we divide the dataset into two types (Section 4.2). The 'Type I' observations observe the complete disk of Venus which includes the bright dayside along with the nightside, while 'Type II' observations primarily look at the nightside (with a small portion of the dayside). To study the noise in the data, we first process the raw data (level 1b) by recreating the pipeline given by Iwagami et al. (2018) to get the calibrated physical values from the data (level 2c). Based on the study, we divide the noise present in the level 2c data into four types which are: a bias, a gradient, a nonlinear effect, and vignetting.

In Section 4.3, we develop a procedure to reduce the above-discussed noise which includes the sky-brightness correction, selective masking, residual bias correction, and calibration of the data based on the VIRTIS dataset. As shown in Figure 4.7, the range of the radiances of the level 3c dataset starts from 0.05 W/m^2/sr/μm and extends beyond 0.5 W/m^2/sr/μm. After applying our procedure, the radiance range is reduced to 0.005 to 0.07 W/m^2/sr/μm which is comparable to the VIRTIS observations. Thus, the procedure developed in Section 4.3 successfully mitigates the noise levels in the data and converts the data into a more usable format. Lastly, because of high contamination Singh (2019) had not used the Type I observations that are also made useful after applying our procedure.

The standard deviation of the processed IR1 dataset (Level 3h) is much higher When comparing with the VIRTIS dataset (Figure 4.11). The primary reason for this is that the IR1 dataset could not be corrected for the localized cloud optical thickness variations that were corrected in the VIRTIS dataset. Also, it can be observed from Figure 4.11 that the scatter of the IR1 data increases as we go from higher altitude level towards lower altitude regions. The main reason for this is that the observations at higher altitudes are fewer in comparison with those at the lower altitude. Also, even after applying all the corrections mentioned above a few observations at the lower altitude still exhibit some effect of stray light. Given that we are considering the quality of the entire dataset, we include these affected observations while making this scatter plot which explains the observed shape.

4.5. Future Work

After applying the selective masking procedure, the mapped dataset, i.e., the level 3f and onwards, shows the interpolation noise (explained in Subsection 4.3.3). As explained in Section 6.2 and Section 6.4, this noise has no major effect on the radiance vs altitude and temperature vs altitude relation. So, we do not correct this noise in the current study. However, for any future studies where such noise could pose a problem, it can be easily corrected by using an edge detection algorithm. We identify the 'canny' feature in 'skimage' package of Python to be highly suitable for this task.

5

Atmospheric Radiative Transfer

The most effective way to remotely study the atmospheres of other planets is to observe their absorption, reflection, and emission spectra, either from an orbiting spacecraft or with ground-based telescopes. The UV, visible and near-IR spectra can be used to observe clouds and hazes while thermal emission spectra are useful to constrain the temperatures, gas, and aerosol abundances (Irwin et al., 2008). The atmospheric spectral windows play an important role while studying the thermal emission spectra and are discussed in Subsection 5.1.1.

The simplest way to interpret the observed spectra is to choose its best match among a range of synthetic spectra which are calculated from a probable set of atmospheric parameters. This process is carried out in the form of (1) radiative transfer model or forward model combined with (2) retrieval codes. The radiative transfer code generates a synthetic spectrum based on an assumed atmospheric structure. The retrieval code then compares the observed and synthetic spectra and makes adjustments to the assumed atmospheric parameters to minimize the difference between both spectra. In our study, only the radiative transfer or forward code is required to generate a synthetic map of thermal emission from the surface of Venus. In this study, we use the radiative transfer code from Wauben et al. (1994) which is shortly discussed in Subsection 5.1.2. Using this code an atmospheric model is set up which is described in Section 5.2. Lastly, we use the synthetic spectra created for Mueller et al. (2020) using the atmospheric model described in Tsang et al. (2008) for the validation of our atmospheric model which is explained in Section 5.3.

5.1. Background

5.1.1. Atmospheric Spectral Windows

When remotely observing the surface of a planet covered by an atmosphere, various components of the atmosphere affect the intensity of electromagnetic radiation through processes like absorption and scattering. In attenuating the radiation, absorption plays a dominant role over scattering (Lillesand and Kiefer, 1979). Absorption occurs at particular wavelengths and is a characteristic of the various absorbing gases present in the atmosphere. Absorption, while allowing us to detect the presence of different species in the atmosphere, puts limitations on the wavelength range that is useful for any remote sensing application. The spectral region where the atmosphere allows transmission of electromagnetic radiation from the surface and lower atmosphere with minimal absorption or distortion can be defined as an *atmospheric spectral window.*

Characterizing the deep atmosphere of Venus was one of the most challenging aspects because of the planet-wide constant cloud coverage that obscures the radiation from the surface at Visible wavelengths. Observing with the Anglo-Australian Telescope, Allen and Crawford (1984) first detected anomalously bright radiation between 1.69 to 1.77 µm and 2.18 to 2.50 µm from the night side of Venus. Later, Allen (1987) showed that the radiation centered at 2.3 µm was coming from an altitude of 48 km within the major cloud layer, and the origin of the 1.74 µm radiation was possibly even deeper in the atmosphere. Subsequently, the thermal emissions at 1.09, 1.18, 1.27, 1.30, and 1.01 µm were discovered and later confirmed during the 1990 Galileo Venus flyby (Allen, 1990, Carlson et al., 1991).

First ground-based observations of thermal emission from the surface of Venus, centered at 1.0 µm, were obtained by Lecacheux et al. (1993). It was demonstrated that within this atmospheric window, the effect of cloud optical thickness variation on the observed radiances is small enough to discern the surface topography features. Also, the surface emissivity variation has an upper limit of 10% on the variation of observed radiances. Most importantly, the thermal emission of the surface was found to be consistent with the surface temperature in equilibrium with the atmospheric temperature of that altitude. Lecacheux et al. (1993) also predicted the spectral windows allowing the transmission of the thermal emission from the surface in the sub-micron region at 0.85 and 0.90 µm. These were confirmed by the VIMS instrument onboard the Cassini spacecraft during its Venus flyby (Baines et al., 2000). The altitude range of the largest sensitivity of all the available windows in the atmosphere of Venus is summarized in Table 5.1.

The spectrum observed in all of the atmospheric windows contained valuable information on cloud layers and gas species in the deep atmosphere. A detailed spectroscopic analysis of the atmospheric windows was carried out by Pollack et al. (1993), deriving information on abundance, mixing ratios, and, vertical-gradients of some of the species observed below the cloud layers. Kamp et al. (1988) used radiative transfer model to analyze previous observations, confirming that the near-IR emissions could originate from the thermal emission of the gases in the lower atmosphere of Venus. Subsequent modeling efforts(Arney et al., 2014, Bézard et al., 1990, Chamberlain et al., 2013, Crisp, 1989, Haus and Arnold, 2010, Kamp and Taylor, 1990, Taylor et al., 1997, Tsang et al., 2008) gradually improved the understanding of the altitudes that

Table 5.1: Altitudes of largest sensitivity of NIR Spectral Windows of Venus

Window (μm)	Depth
0.85	Surface
0.90	Surface
1	Surface
1.10	0-15 km
1.18	0-15 km
1.28	0-30 km
1.31	10-50 km
1.74	10-30 km
2.3	20-45 km

are probed in various windows. Carrying out this analysis further, Knicely and Herrick (2020) demonstrated the use of these windows for an aerial mission flying at a nominal altitude of 40km and also identified new potential windows for surface observation from this altitude.

In summary, the discovery of the NIR spectral windows provided a new way to sound the deeper parts of the atmosphere of Venus using remote observation tools, which previously depended on in-situ observations. The observations that were taken by VIRTIS (Piccioni et al., 2007) and VMC (Markiewicz et al., 2007b) onboard the Venus Express mission, along with the IR-1 and IR-2 cameras onboard the Akatsuki mission (Peralta et al., 2017) utilize these atmospheric windows. Thus the factors affecting the emission in these windows are important for our study. Lastly, Lecacheux et al. (1993) showed that the surface was in thermal equilibrium with the atmosphere at that altitude. Thus, retrieving the surface temperature from the full topography range would allow predicting the atmospheric thermal profile in that region which provides the foundation for our current study.

5.1.2. Radiative Transfer Code

Throughout the years, a number of general-purpose radiative transfer codes have been developed, utilizing various multiple scattering algorithms, different methods for molecular line absorption, including or excluding the effects of polarization. They have been used for different planetary and exoplanetary atmospheres, for retrieving a variety of different parameters.

At the core of our atmospheric radiative transfer model, we use the code from Wauben et al. (1994). This code is based on the adding-doubling method (de Haan et al., 1987) and can be used for the calculations of polarized thermal radiation in plane-parallel, vertically inhomogeneous atmosphere. Along with the illumination by a unidirectional beam of light at the top of the atmosphere, the code considers the thermal emission from isotropically radiating internal sources and a ground surface below the atmospheres.

The code considers a multi-layered atmosphere. For each layer, the main parameter that are required are:

1. Single scattering albedo of the atmospheric particles.
2. The depolarization factor for Rayleigh scattering
3. The ratio of molecular optical thickness to the total optical thickness
4. The total optical thickness (molecular and aerosol optical thickness)
5. The expansion coefficients (of scattering matrix) for the cloud particles
6. The thermal emission from the internal sources
7. The thermal emission from the surface (required only for the ground layer)

Thus an atmospheric model which accurately computes all the above parameters for each layer of the atmosphere is required to run the simulations (discussed in the next section). The code provides output in the form of reflection and transmission matrices at the interfaces of all the layers along with the upward and downward radiation field at the number of internal radiation field levels specified within a layer for both cases of illumination mentioned above. We are primarily interested in the upward radiation field at the top. For faster calculations, we turn off the options to output the polarized radiation and the internal radiation field.

5.2. Setup of the atmospheric radiative transfer model

5.2.1. Atmospheric Model

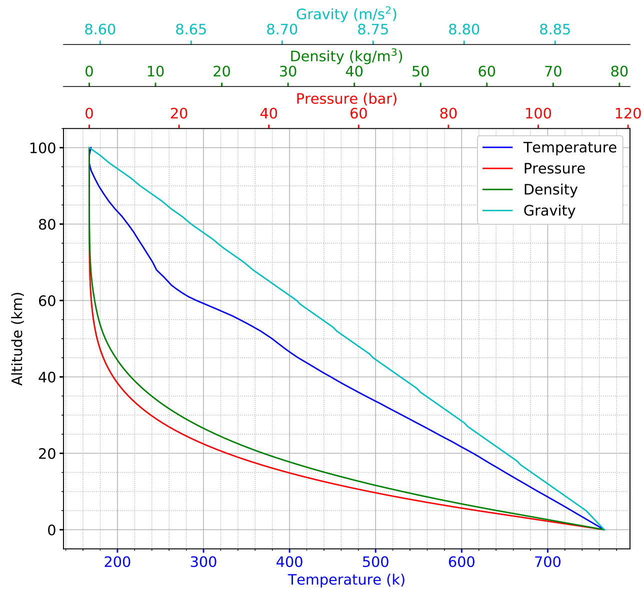

Figure 5.1: Atmospheric profiles derived from VIRA (Seiff et al., 1985)

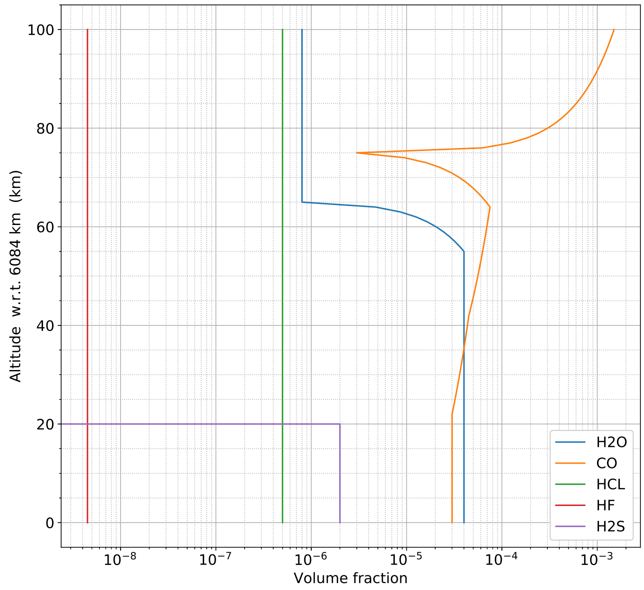

Figure 5.2: Gas abundances

In our model, the atmosphere is discretized by layers of thickness of 1km from the surface up to 100 km altitude. The pressure, temperature, gravity, and density profiles from the Venus International Reference Atmosphere (VIRA) (Seiff et al., 1985) are used that are shown in Figure 5.1. Within a layer, it is assumed that these quantities vary linearly with respect to the altitude and the values of these quantities interpolated at the midpoint of the layer are used wherever required in the layer-based calculations. The eight dominant absorbing species - CO_2, H_2O, CO, HCL, HF, H_2S, OCS, SO_2 are considered for the molecular absorption. The abundances of H_2O, CO, HCL, HF are taken from Bézard et al. (1990) and those of H_2S, OCS, SO2 are taken from Hunten et al. (1983). The abundance of CO_2 is constant and is equal to 0.965.

The altitude range of the surface of Venus extends from -2990 to 11520 m with respect to the mean planetary radius of 6051 km (Ford and Pettengill, 1992). We simulate this change by starting the lowest layer of the atmosphere at the pressure and temperature level corresponding to 6048 km and subsequently increasing the lower boundary till 6063 km to form a lookup table of observed radiances in one dimension and the starting elevation as the second dimension. The VIRA profiles start at a mean planetary radius of 6052 km corresponding to the temperature of 735.3 k and a pressure of 92.1 bar. Below this planetary radius, all the profiles are linearly extrapolated to the radius of 6048 km corresponding to a temperature of 765.7 k and a pressure of 114.7 bar.

5.2.2. Rayleigh Scattering

Rayleigh scattering by the two most abundant species, i.e., CO_2 (~ 96.5%) and N_2 (~ 3.5%), is considered throughout the atmosphere. The scattering cross-sections are calculated as per Hansen and Travis (1974). The refractive index of CO_2 is taken from Haberle et al. (2017) and that of N_2 is taken from Bates (1984). The depolarization factor of CO_2 is 0.09 and that of N_2 is 0.03 (Hansen and Travis, 1974). The depolarization factor of the combined atmosphere is calculated to be 0.879 as a weighted average and the weights assigned as per their respective volume fractions (Bates, 1984). The treatment of Rayleigh scattering in the model is verified by comparing the total optical thickness for Rayleigh scattering (B^m_{sca}) of the atmosphere against the value given in the literature. At 1 µm the B^m_{sca} is ~1.5 which is same as given in Pollack et al. (1993) and Haus and Arnold (2010). The variation of the scattering optical thickness of a particular layer (b^m_{sca}) with respect to altitude is shown in Figure 5.3 and the variation of B^m_{sca} with respect to wavelength is shown in Figure 5.9. The notation 'b' denotes the optical thickness at a particular layer while the notation 'B' denotes the total optical thickness of the atmospheric column.

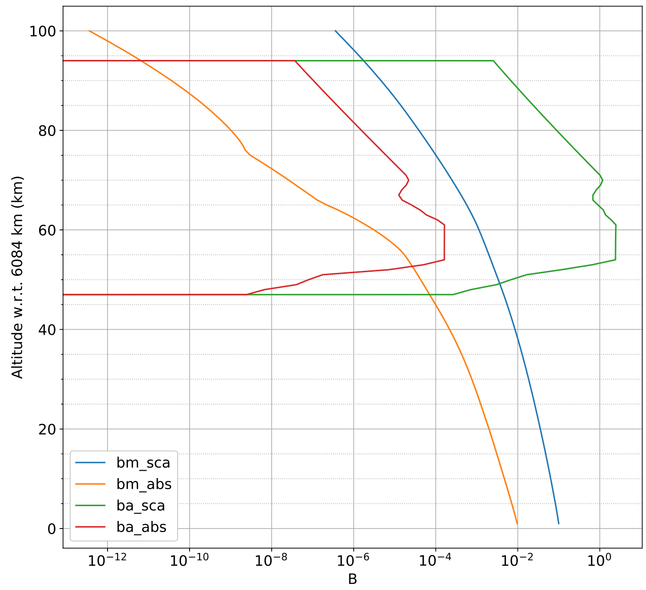

Figure 5.3: The optical thickness of the individual layers varying with altitude

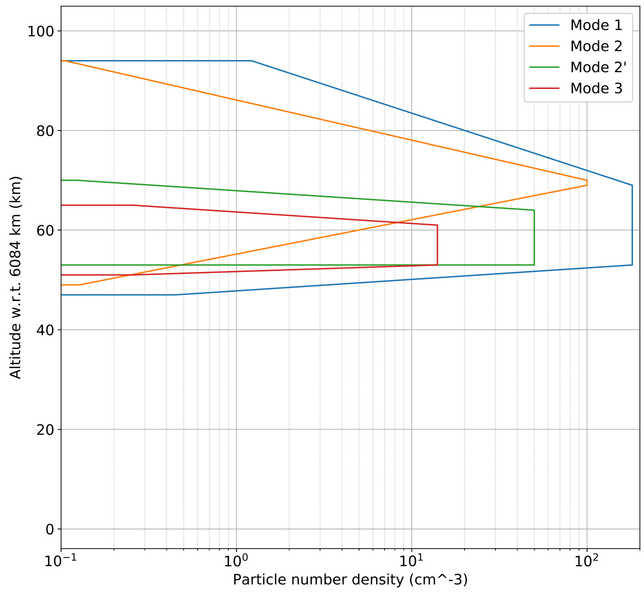

Figure 5.4: Particle number densities for all the four modes from the nominal cloud model of Haus et al. (2013)

5.2.3. Clouds and Mie Scattering:

Characterized by a global cloud cover, Venus shows a complex cloud system. The clouds are located in the altitude range of 45 to 75 km along with the haze layers extending above up to 90-100 km and down to ~30 km altitude (Titov et al., 2018). The Pioneer Venus dataset of cloud particle size distribution by Knollenberg and Hunten (1980) suggests a trimodal particle size distribution. The upper haze consists of sub-micron-sized Mode 1 particles along with Mode 2 particles which extends from 100-90 km to the upper cloud tops (70-62 km). The upper clouds also show a bimodal particle size distribution with Mode 1 and Mode 2 particles. Mode 2 is further divided into Mode 2 and Mode 2' (Pollack et al., 1993). The tropopause (58 km) separates the upper cloud from the middle and lower clouds (48-45 km) which are composed of four modal distributions and are the major source of cloud optical thickness. A clear separation is not observed between the middle and lower clouds. The lower haze extends below the lower cloud deck to 33 km and consists of more tenuous layers of particles. Also, there is a possibility of a near-surface haze layer at an altitude of 1-2 km indicated by the Venera 13, 14 descent probes (Grieger et al., 2004). A further review of the clouds and hazes in the atmosphere of Venus is provided in Section A.2

The Mode 2 particles show a chemical composition of concentrated sulfuric acid (75% H_2SO_4) which are produced photochemically (James et al., 1997, Taylor, 2006). There is also a mysterious UV absorber which allows us to trace the dynamic behavior of the upper cloud layer, however, its chemical origin is not yet known. Limaye et al. (2018c) suggests a possible biological origin for this UV absorber and warrant further investigation on this topic. The composition and the origin of the small Mode 1 particles, the large Mode 3 particles, the lower and near-surface hazes is not yet known (Limaye et al., 2018a). Thus, in our model, we follow the usual assumption that all the four modes have the same composition, viz., 75% H_2SO_4 (Haus and Arnold, 2010, Pollack et al., 1993, Tsang et al., 2008). The refractive indices for this composition are taken from Palmer and Williams (1975).

The complex cloud system described above has been included in previous radiative transfer models of Venus by using various cloud models (Arnold et al., 2008, Barstow et al., 2012, Crisp, 1986, Haus et al., 2013, Lee et al., 2012, Pollack et al., 1993, Zasova et al., 1996). We model the clouds using a four modal particle size distribution considering the modes 1,2,2',3 having modal radii of 0.3, 1.0, 1.4, 3.65 µm and a variance of 1.56, 1.29, 1.23, 1.28 respectively (Pollack et al., 1993). The particles are considered to be homogeneous spheres and the number densities are taken from the nominal cloud model used by Haus et al. (2013). At 1 µm, this model gives a total cloud optical depth $(B_a)of \sim 35$ which is closer to an average retrieved cloud optical thickness of 34.7 from VIRTIS measurements (Haus et al., 2013). Another reason for selecting this cloud model is that the cloud particle distributions of all four modes can be described by simple analytical expressions given in Haus et al. (2013). Various other cloud models provide a lower cloud optical thickness (~28), and thus, a cloud factor of 1.3 to 1.8 w.r.t the initial cloud model was required to explain the observed radiances Haus et al. (2013). Here, the 'cloud factor' or the cloud optical thickness factor is defined as the factor which is multiplied to the particle number densities of Mode 2' and Mode 3 particles in order to increase the total cloud optical thickness (Barstow et al., 2012). For example, Mueller et al. (2020) use the cloud model from Barstow et al. (2012) with a cloud factor of 1.75 to simulate the band 0 radiances from VIRTIS-M-IR. We also include the cloud model from Barstow et al. (2012) in our study which is used in Section 5.3.

Mie scattering theory was used to calculate the microphysical parameters of the cloud particles using the code by De Rooij and Stap (1984). The code calculates the expansion coefficients of the scattering matrices in generalized spherical functions for a single mode of particle distribution at a given layer. We modify this code to consider a multi-modal particle distribution and a multilayered cloud model. Along with the expansion coefficients, the parameters like scattering and extinction cross-sections and efficiency, single scattering albedo are also calculated. The dependence of optical thicknesses of aerosol particles in a particular layer (b^a_{sca} and b^a_{abs}) with respect to altitude at 1-micron is shown in Figure 5.3. The dependence of the total optical thicknesses for entire atmospheric column (B^a_{sca} and B^a_{abs}) with respect to wavelength is shown in Figure 5.9.

Shortward of the 1.5 µm region all four modes combined attenuate the radiation mostly as a grey absorber (Bézard et al., 1990, Meadows and Crisp, 1996). The H_2SO_4 particles show a nearly constant single scattering albedo over a narrow wavelength region (~0.999 for 1 µm window). Thus, the effect of various cloud modes and their properties on the radiation is almost wavelength independent and a nearly constant B^a_{sca} can be observed in Figure 5.9. Figure 5.7 shows the effect of increasing the cloud optical thickness on the 1-µm window. It can be observed that increasing the cloud optical thickness primarily attenuates the radiation and does not directly affect the spectral features for the reasons mentioned above.

Longward of 1.5 µm, the cloud particles show a non-grey behavior (Tsang et al., 2008). Changes in the cloud optical thickness heavily affect the shape of the simulated spectra for the 1.7 and 2.3 µm windows. For example, when the cloud optical thickness is higher than average, the added contribution from the cloud thermal emission has a similar impact on the spectral shape as that of decreasing the abundances of certain atmospheric species (Arney et al., 2014). Thus, using a full four-modal particle distribution allows the use of our atmospheric radiative transfer model for future studies concerning the 1.7 and 2.3 µm windows.

5.2.4. Spectral data for the absorbing species

For the 1 µm window, the dominant absorbing species are CO_2 and H_2O. Along with these, we also consider the absorption from four minor absorbing species which are CO, HCL, HF, H_2S. Additionally, the OCS and SO_2 gases are also added which affect the longward side of the 2.3 µm window. To calculate the absorption cross-sections, we primarily use the latest versions of the HITRAN and HITEMP datasets. These dataset provide parameters like the line intensities, air and self-broadening halfwidths, pressure shift of the line position, etc. It should be noted that the parameters are primarily calculated for the Earth's atmosphere and might need some modifications when applying to the atmospheres of other planets. Whilst HITRAN, being a high-resolution transmission spectral database, contains the lines from certain hot bands, it does not contain all the hot bands that are required for the calculation of accurate synthetic spectra of Venus (Pollack et al., 1993). The deep atmosphere of Venus is very hot and optically thick and the thermal emissions from this region escape between the strong CO_2 and water vapor bands. The hot bands, including overtones, combinations, and, differences, are termed as weak lines given their low intensity and become very important while modeling the shape of the atmospheric windows (Tsang et al., 2008). Sufficient information about these bands is provided by the HITEMP database. A comprehensive discussion involving older versions of HITRAN and HITEMP databases can be found in Pollack et al. (1993).

While developing the HITEMP2010 database (Rothman et al., 2010), the HITEMP1995 CO_2 database (Rothman et al., 1995) was replaced by a more accurate CDSD-1000 database (Perevalov and Tashkun, 2008). However, this database has gaps in the wavelength intervals at 8700 and 10000 cm^{-1} which coincide with the 1 and 1.1 µm windows. This can be observed from Figure 5.5 shown by the red curve. The HITRAN database was recently updated (Gordon et al., 2017) and now includes a number of lines in these intervals, however, they are still not enough to produce accurate absorption spectra (green curve). Thus, we take the spectroscopic line parameters of CO2 from the high-temperature CO_2 database that was computed specifically for Venus by Pollack et al. (1993) and provides missing spectral lines in the wavelength intervals at 8700 and 10000 cm^{-1} (blue curve). This database is referred to as the HITEMP-Venus database in this report. A detailed comparison between the two datasets can be found in Haus and Arnold (2010).

The spectral parameters of H_2O are taken from the HITEMP2010 database which is the most comprehensive high-temperature line database for H_2O. In this database, the line data for the principal isotopologue was taken from the BT2 line list (Barber et al., 2006) and has significant improvements comparing with HITEMP1995. However, the data for other isotopologues were taken from the HITRAN dataset. Given that water vapor absorption affects the 1 µm window shortward of 0.975 µm the HITEMP2010 database provides sufficiently accurate results for our study. The HITRAN 2016 (Gordon et al., 2017) also released a major update for HITRAN H_2O data and the absorption cross-section generated from both HITEMP2010 and HITRAN2016 are shown in Figure 5.6. It can be observed that the HITRAN2016 database (green line) produces a good match with the HITEMP2010 database for the spectral region of our interest. However, we continue using the HITEMP2010 database for consistency with other models and future use in other spectral windows. A more accurate database for the HDO isotopologue is available from Voronin et al. (2010) known as the VTT line list and we note here that for future studies involving the water-vapor retrieval using our model, the HDO data from HITEMP2010 should be replaced with the VTT line list.

The spectral parameters of CO are taken from the HITEMP2010 database while those of HCL, HF, H_2S, OCS, and SO2 are

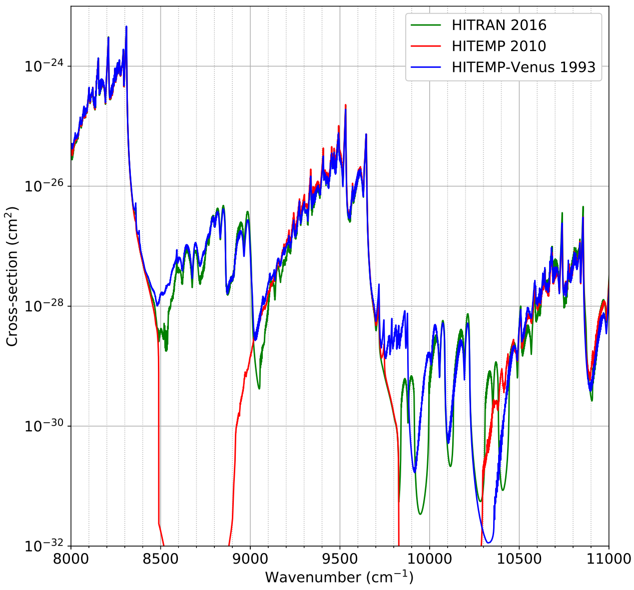

Figure 5.5: Comparison of the CO_2 absorption cross-sections using different databases at a pressure of 20 atm and temperature of 575 k

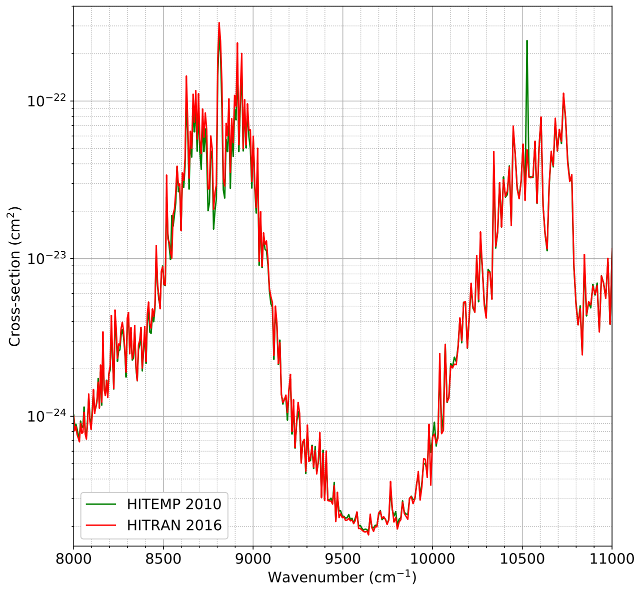

Figure 5.6: Comparison of the H_2O absorption cross-sections using different databases at a pressure of 20 atm and temperature of 575 k

taken from HITRAN2016 (Gordon et al., 2017). The abundance of these species is very low in the Venusian atmosphere (Figure 5.2) and the line data from the HITRAN2016 dataset is sufficient to produce an accurate Venus spectrum.

5.2.5. LINE SHAPE CALCULATIONS

In the deep atmosphere of Venus, the pressure and the temperature increases from 12 bar and 520 K at the ~35 km altitude to 92 bar and 735 K near the surface (at R = 6052 km). Because of these extreme conditions, the effects of thermal Doppler broadening and pressure broadening on the absorption line shapes become important. The Doppler broadening is best described by a Gaussian profile while the pressure broadening is best described by a Lorentzian profile (Goody and Yung 1989). In our model, we use the Voigt profile which is the convolution of both of these profiles. In the deep atmosphere of Venus, the pressure broadening dominates, and the Voigt profile reduces to a Lorentzian profile. The high pressures result in rotational inelastic collisions between atoms which causes a transfer of energy between rotational bands. This causes a transfer of line intensities onto each other and the lines get coupled which is known as the collisional line mixing or line coupling (Tsang et al., 2008). Because of the collisional line mixing, the lineshapes of CO_2 is best described by sub-Lorentzian line profiles (Burch et al., 1969) in which the optical thickness far from the line center decreases more rapidly than that predicted by the Lorentz profile, causing a narrowing of the line. This profile is commonly modeled as a product of the Lorentz profile and the function (χ) of the difference between the wavenumbers of the line center (ν_0) and wavenumber of the interest (ν) (Burch et al., 1969).

In the past, various authors have used different analytical functions to fit the χ function based on the lab measurements and observations (Bézard et al., 1990, Burch et al., 1969, de Bergh et al., 1995, Tonkov et al., 1996). The sub-Lorentzian profile is highly dependent on the line cut parameter used while calculating the function (χ). This is especially important for the 1.18 µm window and the flank of 1 µm window. It is observed that for these windows the behavior of CO_2 is less sub-Lorentzian than for the windows at 1.7 and 2.3 µm. We use the sub-Lorentzian profile given by Bezard et al. (2009) (Equation 5.1) for the windows shortward of 1.5 µm and that given by Tonkov et al. (1996) (Equation 5.2) for the remaining windows. We use the line cutoff at 120 cm^{-1} from the line center. For all the species other than CO_2, we calculate the full Voigt profile with a line cutoff at 120 cm^{-1}. The line-by-line absorption code from Stam et al. (2000) is used for these calculations.

$$
\begin{aligned}
\chi = &1, \quad |\delta\nu| < 3\mathrm{cm}^{-1} \\
&1.0510\exp(-|\delta\nu|/60), \quad 3 < |\delta\nu| < 60\mathrm{cm}^{-1} \\
&0.6671\exp(-|\delta\nu|/110), \quad |\delta\nu| > 60\mathrm{cm}^{-1}
\end{aligned}
\tag{5.1}
$$

$$\chi = 1, \quad |\delta\nu| < 3\text{cm}^{-1}$$
$$1.084\exp(-0.027|\delta\nu|), \quad 3 < |\delta\nu| < 150\text{cm}^{-1}$$
$$0.208\exp(-0.016|\delta\nu|), \quad 150 < |\delta\nu| < 300\text{cm}^{-1} \tag{5.2}$$
$$0.025\exp(-0.009|\delta\nu|), \quad |\delta\nu| > 300\text{cm}^{-1}$$

Because CO_2 is the most abundant gas, the broadening of half widths by CO_2 is important for the Venusian atmosphere and while calculating the lineshape of CO_2, we use the CO_2-CO_2 self-broadening half widths that are taken directly from HITEMP-Venus. For H_2O lineshape calculations CO_2–H_2O foreign-broadening is considered by multiplying the air-broadened half widths, taken from HITEMP2010, by a constant factor of 1.3 (Howard et al., 1956, Pollack et al., 1993). The HITRAN2016 includes the half widths for foreign-broadening by CO_2 for CO, HCL, HF which are used directly. However, in absence of foreign-broadening data for H_2S, OCS, and SO2, they have been air-broadened using the air-broadening half widths from HITRAN2016.

5.2.6. Collision-Induced Absorption

The high pressures in the deep atmosphere give rise to another source of absorption resulting from the collision and subsequent deformation of two non-polar molecules (Tsang et al., 2008). It is known as collision-induced absorption (CIA) or pressure-induced absorption. Here, the line strengths of the bands are governed by the probability of collisions between the molecules, and thus, they are determined by the square of the local number density of the gas (Burch et al., 1969). The long path length CO_2 along with extreme partial pressures in the deep atmosphere make the CO_2 continuum optical thickness an important parameter while generating the synthetic spectra. This is especially important when modeling 1.7 and 2.3 µm windows where the contribution of this optical thickness is very high (Pollack et al., 1993). Pollack et al. (1993) also discuss the contribution from H_2O continuum optical thickness (both the H_2O-H_2O and CO_2–H_2O). However, this contribution is less significant and it is usually not included while modeling the synthetic spectra. A number of laboratory experiments have been conducted to measure the contribution from the CO_2 CIA which is expressed in the form of a constant α ($\text{cm}^{-1}\text{amagat}^{-2}$) (Brodbeck et al., 1991, Moore, 1971, Moskalenko et al., 1979, Tonkov et al., 1996). However, the laboratory experiments were centered around the 2.3 µm region and were carried out at room temperature. In addition to this, the values of α derived from these experiments differ significantly from each other. Also, the temperature dependence of these values is difficult to estimate theoretically. When used to generate the synthetic spectrum of Venus, these values do not produce a good match (Pollack et al., 1993). Thus, it has been a common practice to find the value of α based on the difference between the observed and the simulated spectra. α has different values in different windows, however, it is assumed that α remains constant within a specific window (Pollack et al., 1993, Tsang et al., 2008).

The continuum optical thickness (B^m_{CIA}) is calculated as shown in Equation 5.3. Here, ρ is the particle number density of the layer expressed in amagat-cm and l is the layer thickness expressed in cm. As we increase the value of α, more optical thickness is added in the deep atmosphere which is the origin of the radiation in the spectral windows. This results in a decrease in the simulated thermal emission as shown in Figure 5.8. This effect is similar to that of increasing the cloud optical thickness shown in Figure 5.7. A difference in these two effects is that the change in CIA also affects the slope of radiance with respect to topography. This is a problem since the change of temperature with respect to topography is not well known and results in difficulty in estimating the value of α. Thus based on different cloud models used by various authors, different values of α are reported for various windows. For the 2.3 µm window the reported value of α ranges from a lower estimate of 2.5e-8 $\text{cm}^{-1}\text{amagat}^{-2}$ to an upper estimate of 7e-8 $\text{cm}^{-1}\text{amagat}^{-2}$ (Bézard et al., 1990, de Bergh et al., 1995, Pollack et al., 1993). The 1.7 µm window shows a similar variation in the reported values of α with a lower limit of 5e-9 $\text{cm}^{-1}\text{amagat}^{-2}$ to an upper limit of 8e-9 $\text{cm}^{-1}\text{amagat}^{-2}$.

$$B^m_{CIA} = \alpha * \rho^2 / l \tag{5.3}$$

This effect is further complicated for the 1 µm window beacuase of the additional sensitivity to the water vapor abundance. The strong water vapour band centered at 0.95 µm results in much lower values of α for this window, with a lower limit of 0 (no continuum) to an upper limit of 1.9e-10 $\text{cm}^{-1}\text{amagat}^{-2}$ (Arney et al., 2014, Haus and Arnold, 2010, Mueller et al., 2020).

The sub-Lorentzian profile and the line-cut criterion mentioned in the earlier section introduces another source of variability while estimating the value of α. For a chosen model of the sub-Lorentzian profile, as the line-cut parameter is increased, absorption is added from the lines that are farther away from the region of interest. Given that the emission windows are located between the strong absorption bands of CO_2, varying the line-cut parameter highly affects the optical thickness values which in turn affects the required value of α. The low values of absorption cross-sections for the wavelength interval around the 1 µm window, exacerbate the effect of the sub-Lorentzian profile and the line-cut criterion on thermal emission within this window.

5.2.7. Summary of the optical thicknesses

The earlier sections describe various sources of optical thicknesses that are present in the Venusian atmosphere and are important to consider while simulating the thermal emission. The optical thickness arising due to the scattering and absorption from the cloud particles (B^a_{sca} & B^a_{abs}) is treated as per the Mie scattering theory which is discussed in Subsection 5.2.3. The optical thickness produced by scattering of light by the gas particles (B^m_{sca}) is treated as per the theory of Rayleigh scattering (Subsection 5.2.2).

The most important, and at the same time, hardest to model is the optical thickness from absorption of light by the gases in the atmosphere (B^m_{abs}). The calculations of the spectral line shapes of absorbing species are discussed in Subsection 5.2.5 which are used to get the layer-wise absorption optical thickness from various gas species. Then the layer-wise contribution from the continuum optical thickness, b^m_{CIA} (discussed in Subsection 5.2.6) is added to get the final absorption optical thickness of that layer (b^m_{abs}). Figure 5.10 shows the layerwise absorption optical thicknesses of CO_2 and H_2O for five different layers in the atmosphere. It can be observed that with increasing depth in the atmosphere, the spectral features are smoothened out. The flat region between 0.96 to 0.98 µm in the CO_2 curves shows the direct contribution from the CO_2 continuum optical thickness. It can also be observed that shortward of 0.99 µm H_2O dominates the absorption spectrum.

Figure 5.9 shows the optical optical thickness of the entire atmospheric column for the wavelength range of 0.9 to 1.05 µm. Here, the total absorption optical thickness (B_{abs}) is calculated as the addition of B^a_{abs}, B^m_{abs}, and B^m_{CIA}. Similarly the total scattering optical thickness (B_{sca}) is calculated as the summation of B^a_{sca}, B^m_{sca}. While the total optical thickness of the atmosphere (B) is the summation of B_{sca} and B_{abs}. It can be observed that B^a_{sca}, B^a_{abs}, and B^m_{CIA} are either constant or nearly constant. B^m_{sca} decreases as we increase the wavelength and B^m_{abs} is highly variable which produces the distinct shape of the 1 µm window.

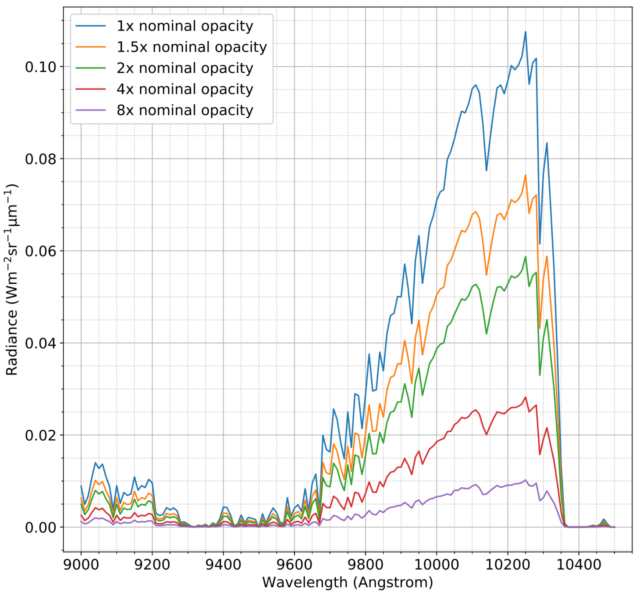

Figure 5.7: The effect of increasing the optical thickness of the entire cloud deck on the thermal emission within the 1 µm window

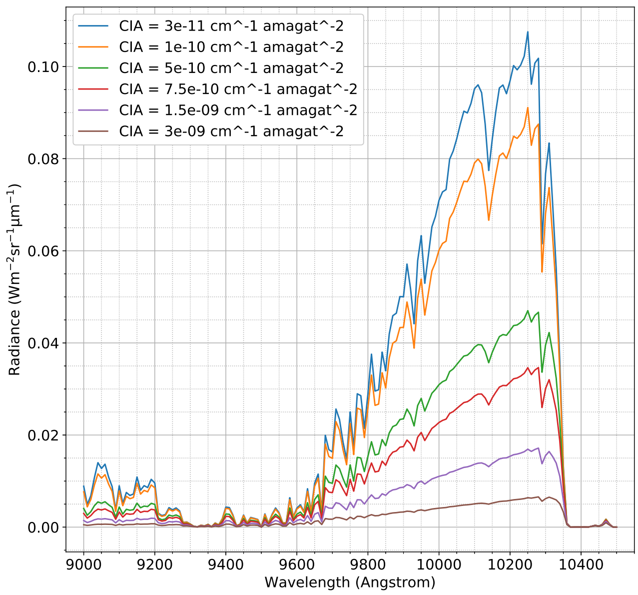

Figure 5.8: The effect of increasing the value of α on the thermal emission spectrum

5.2.8. Thermal Emission

Previous observations show that the temperature of the surface is in thermal equilibrium with the atmosphere at that altitude (Lecacheux et al., 1993). Thus, the temperature of the surface is considered to be equal to that of the lowest layer in the atmosphere. The thermal emission from the surface (L_{surf}) is calculated as shown in Equation 5.4. Here, A_g is the ground albedo and the $L(\lambda, T)$ is the spectral radiance at the given wavelength and temperature as per Planck's law.

$$L_{surf} = (1 - A_g) * L(\lambda, T) \tag{5.4}$$

Similarly, the thermal emission from the atmospheric layers (L_{atm}) is calculated as shown in Equation 5.5. Here, a is the single scattering albedo which is the ratio of scattering optical thickness of a layer (b_{sca}) to the total optical thickness (b) of that layer. Here, we express the radiance (L_{surf} and L_{atm}) in the unit of $Wm^{-2}sr^{-1}µm^{-2}$.

$$L_{atm} = (1 - a) * L(\lambda, T) \tag{5.5}$$

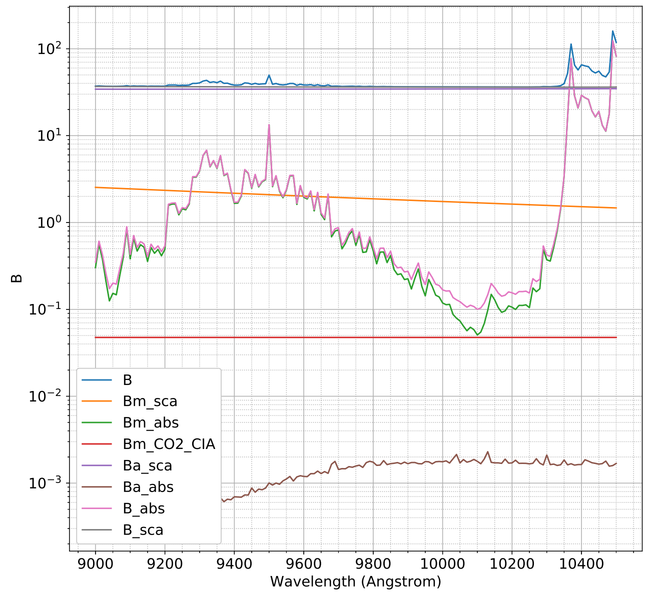

Figure 5.9: The optical thickness of the entire atmospheric column as a function of the wavelength

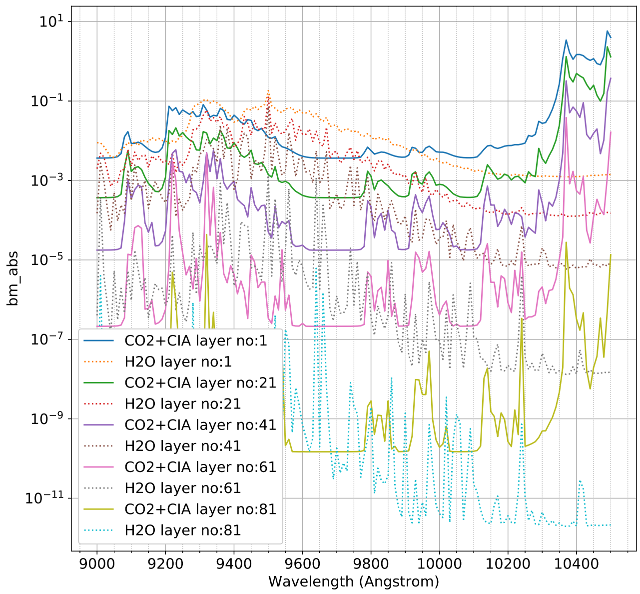

Figure 5.10: The absorption cross-sections of CO_2 and H_2O for five atmospheric layers

5.3. Validation

As described earlier in Subsection 5.2.5 and Subsection 5.2.6, there are at least six variables that affect the shape of the 1 µm window. These are:

1. Nominal cloud model (B_a)
2. H_2O spectral line shape
3. H_2O abundance
4. CO_2 Sub-lorentzian line profile (χ) and Line-cut criterion
5. CO_2 Continuum optical thickness (α)
6. Surface emissivity

Throughout the years, different authors have used different estimations of these variables while making a fit to the observations. We validate our model by using the spectrum generated by Tsang et al. (2008) which is available in the form of a look-up table with five dimensions. These are explained below:

1. Wavelength (1000 to 1350 nm)
2. Surface emissivity (0.2 to 1)
3. Topography (2 to 10 km w.r.t. 6048 km radius)
4. Cloud optical thickness factor for Mode 2' and 3 (0.25 to 8)
5. CIA coefficient (1e-10, 3e-9).

Tsang et al. (2008) use a cloud model similar to that of Barstow et al. (2012) which has a nominal cloud optical thickness of 28 which is much less than the cloud model from Haus et al. (2013). Thus, we extract their spectrum at the cloud optical thickness factor of 2 which gives a reasonable fit to the VIRTIS spectra (Mueller et al., 2020). Moreover, for the purpose of validation, we use the cloud model from Barstow et al. (2012) with a cloud factor of 2, and thus fixing one of the six variables listed above.

We further reduce the dimensions of the look-up table from Tsang et al. (2008) by extracting the spectrum at the surface emissivity of 1, and CIA coefficient of α = 1e-10 cm^{-1}amagat^{-2} which is plotted by the dotted lines in Figure 5.11. We use the same H_2O abundance, surface emissivity, CIA coefficient for our simulations. However, the line shape of H_2O is different given that we are using HITEMP2010 as compared with HITRAN2K used for the look-up table by Tsang et al. (2008). Additionally, we use a different sub-Lorentzian profile and line-cut criterion of CO_2.

We get a close match for the windows at 1, 1.1, 1.18, 1.27 and 1.31 µm which is shown Figure 5.15. Next, we use the relation of radiance with topography to validate our model. Figure 5.12 shows the plot of radiance vs topography extracted at the 1, 1.01, 1.02µm which shows a close match between the two spectra for the relation of radiance vs topography. This can be used as a validation for our model. Once validated, our model can be further used for future studies dealing with surface emissivity variations, gas abundance retrieval, and also for simulations of the radiation field as observed by a descending probe in the atmosphere of Venus. The modifications that might be required for the future use are discussed next in Section 5.4.

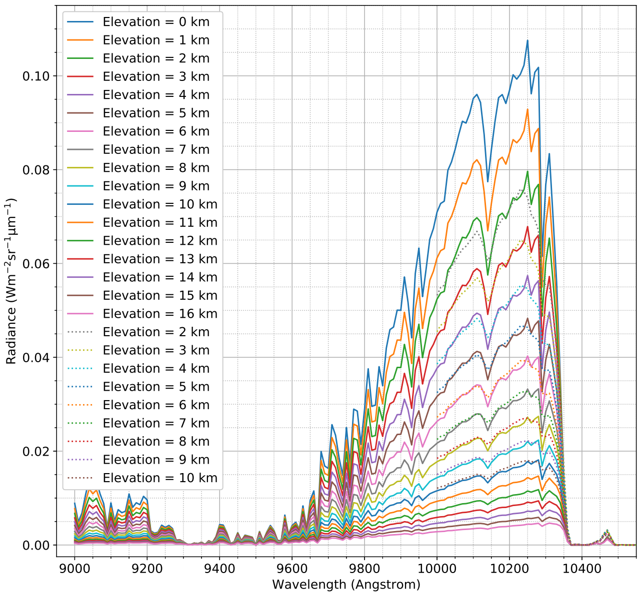

Figure 5.11: Thermal emission in the 1 µm window as compared with the Look-up table generated by Tsang et al. (2008).

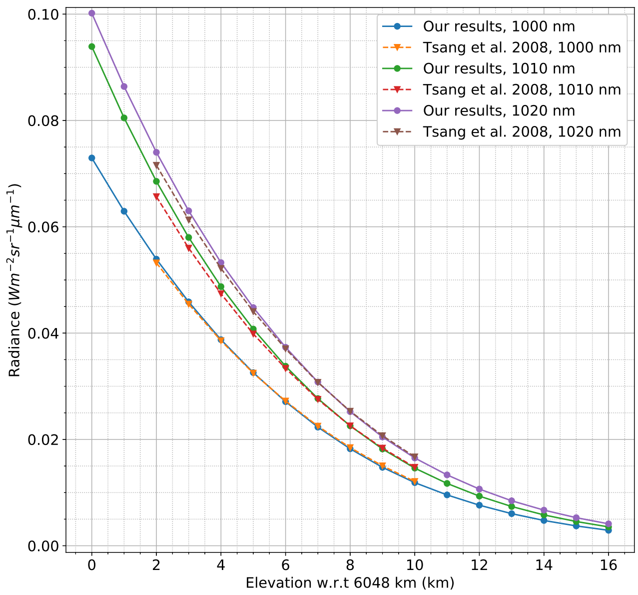

Figure 5.12: The effect of changing the surface surface elevation on the thermal emission within the 1 µm window

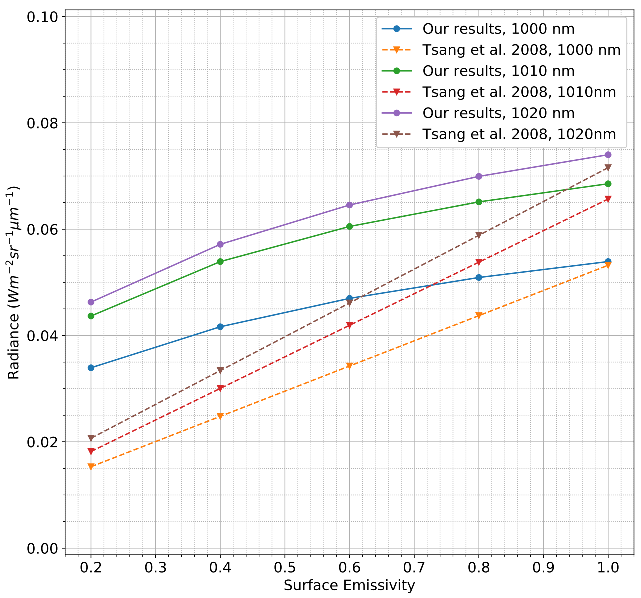

Figure 5.13: The effect of changing the surface emissivity on the thermal emission within the 1 µm window

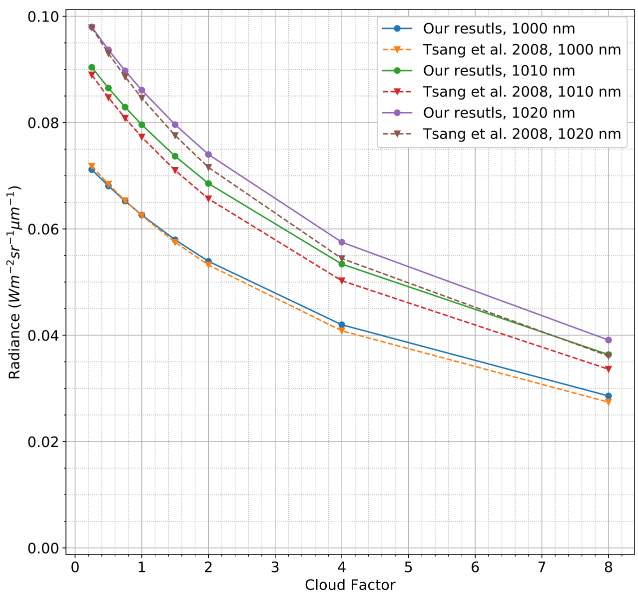

Figure 5.14: The effect of changing the cloud factor on the thermal emission within the 1 µm window

5.4. Future Work

Although we get a good match for the radiance vs. topography relation, we report a significant difference in radiance vs. emissivity relation. Figure 5.13 shows the plot of radiance vs emissivity at three wavelengths for our model and the model of Tsang et al. (2008). The plot is made for the same elevation (2 km), cloud factor (2) and same $\alpha(1e-10\ \mathrm{cm}^{-1}\mathrm{amagat}^{-2})$ as described in the earlier section. It can be observed that our model follows a nonlinear relation as opposed to a linear

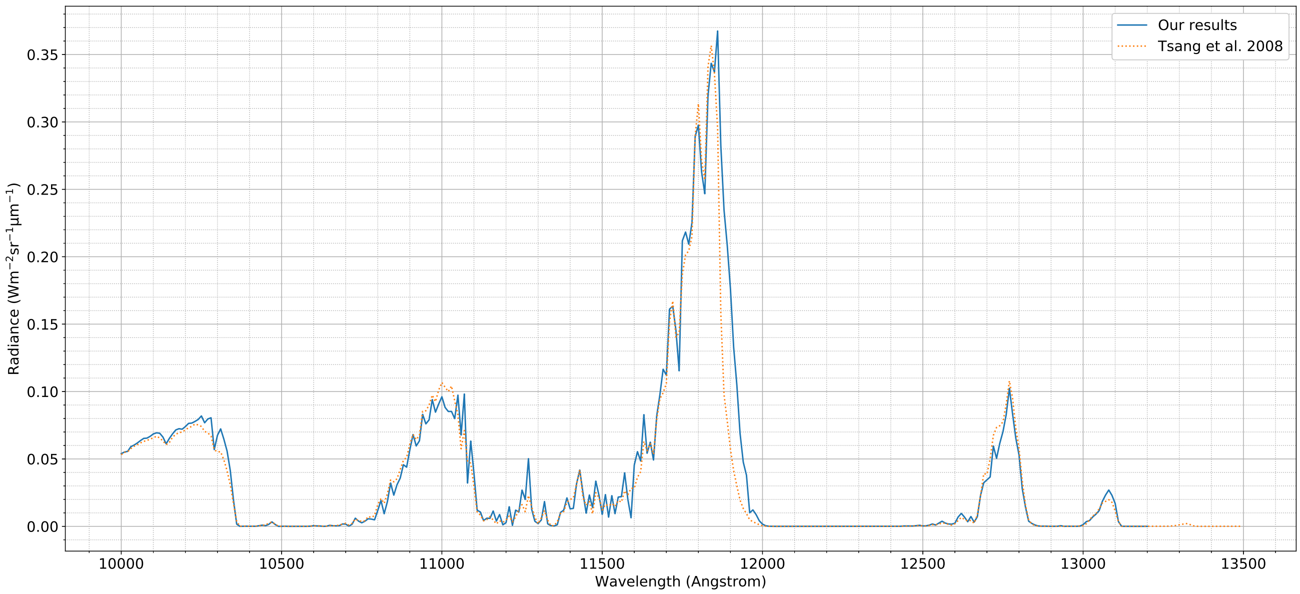

Figure 5.15: Thermal emission in the 1 μm window as compared with the Look-up table from Tsang et al. (2008).

relationship observed from the model of Tsang et al. (2008). While a nonlinear relation between the radiance vs emissivity is expected (Mueller et al., 2020), our model significantly overestimates the radiances for lower emissivity values. A possible reason for this might be multiple cloud surface reflections as described in Hashimoto (2003). Another possible reason might be that for the 1 μm window, our model underestimates the contribution of the surface-emission and overestimates the contribution of the radiation from the lower atmosphere. This behaviour needs to be investigated further for future use of our model dealing with surface emissivity variation studies.

Figure 5.14 shows the plot of radiance vs cloud factor at three wavelengths for our model and the model of Tsang et al. (2008). This plot is made for the same elevation (2 km), emissivity (1) and $\alpha(1e-10\ \text{cm}^{-1}\text{amagat}^{-2})$ as described in the earlier section. A small difference is observed between the radiance vs. cloud factor relation. As shown in Figure 5.15, we don't get an exact match for all the spectral features of the windows at 1.1 and 1.18 μm. There is a mismatch of the absorption features at the peak of the 1.1 μm window. Also, our model overestimates the radiance in the right flank of the 1.18 μm window. These differences can be accounted for by the differences in modeling of the spectral line shape used by both models. Thus, further work is required for future studies dealing with the retrieval of gas species using the emission in these windows.

6 Results

6.1. Surface temperature retrieval

In order to get an accurate surface temperature retrieval, it is important to first make an accurate estimation of the thermal emissions from the atmosphere of Venus. To simulate the instrumental effects, the estimated emission spectrum is convolved with the transmission profile of VIRTIS of Band 0 and IR1 1.01 μm filter which is discussed in Subsection 6.1.1. As discussed in Section 5.3, the thermal emission in the 1 μm window is dependent on various parameters. The effect of changing the model parameters on the retrieved temperatures is discussed in Subsection 6.1.3.

Once we have an estimate of the thermal emission, the deviation of the observed radiance with respect to the simulated radiance (at given topography)is used to retrieve the surface temperatures (explained in Subsection 6.1.2). From our simulations, we use the radiances at $\theta = 0$ or $\mu = 1$ (where θ is the angle made by outgoing radiation with respect to the normal of the atmospheric plane, and $\mu = \cos\theta$). Although the model simulates the radiances at a variety of μ directions, a separate computation is not required given that the effects of the observation geometry have been already corrected in Subsection 4.3.2 in the form of a limb darkening correction. Thus, every pixel in the observations (beyond level 2f) represents the corrected nadir radiances, i.e, the radiances observed at an emission angle of zero. The corrected dataset (level 2h) is ready for direct retrieval using the method discussed in Subsection 6.1.2.

6.1.1. Transmission Profiles

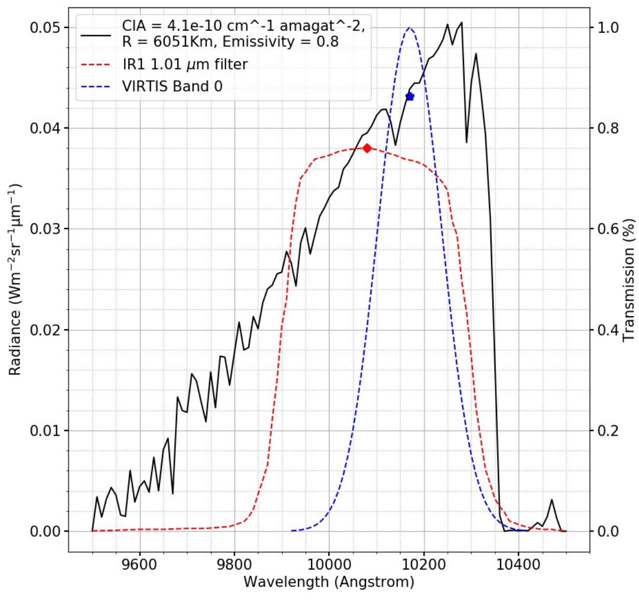

Figure 6.1: The transmission profile of IR1 1.01μm filter (red dashed curve) and VIRTIS Band 0 (blue dashed curve), on top of the simulated 1 μm window radiance at an elvation of 3 km (wrt 6048km). The radiance measured by IR1 in 1.01μm filter and VIRTIS Band 0 is shown by red diamond and blue star at the respective central wavelengths

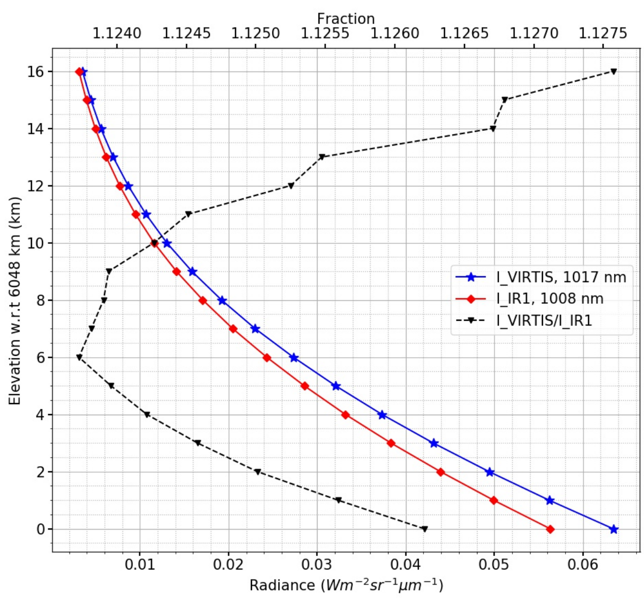

Figure 6.2: The elevation vs radiance profile as computed for (I_{IR1}) IR1 1.01 μm filter (red) and (I_{VIRTIS}) VIRTIS Band 0 (blue). The dashed black curve shows the fraction of I_{VIRTIS}/I_{IR1}

The transmission profiles of VIRTIS Band 0 and IR1 1.01 μm filter are shown in Figure 6.1. The VIRTIS Band 0 (shown by blue dashed cure)is centred at 1017 nm and has a shape of Gaussian distribution with an FWHM of 15.75 nm. The IR1 1.01 μm filter (shown by dotted red curve) has a slightly wider filter with an FWHM of 40 nm centred at 1008 nm. The solid black line shows the simulated spectra at starting elevation of z = 3km. The CIA coefficient used for this spectrum is $\alpha = 4.1e - 10\mathrm{cm}^{-1}\mathrm{amagat}^{-2}$ and the cloud factor (Subsection 5.2.3) is 2. The red and blue points indicate the radiance value after convolving this spectrum with the transmission profiles of IR1 and VIRTIS respectively.

The central wavelengths of IR1 1.01 μm filter and VIRTIS Band 0, and their transmission profiles are different from each other. Thus, the radiances observed by both instruments show some differences. Figure 6.2 shows the radiances as observed by IR1 (I_{IR1}) and VIRTIS (I_{VIRITS}) varying with the topography by red and blue curves respectively. These curves are computed by convolving the IR1 1.01 µm and VIRITS Band 0 profiles with the look-up table created by varying the starting elevation from 0 to 16 km while keeping all the other parameters (emissivity, cloud factor, CIA coefficient) the same. The dashed black line shows the ratio of I_{VIRTIS} to I_{IR1}. Given the non-linear nature of the simulated radiances, this ratio varies as we change the topography. Thus, there is not a single factor that can be used to derive I_{IR1} radiance from I_{VIRTIS} radiance for all the topography ranges. This is important given that in the final step of processing the IR1 observations (Subsection 4.3.5), we had scaled the improperly calibrated IR1 radiances based on the corrected VIRTIS radiances, i.e., up to the level of I_{VIRTIS} radiance profile. While doing so we use a single scaling factor for all the altitude levels. A logical next step would be to scale the IR1 radiances further down to the level of I_{IR1}. However, as the ratio between I_{VIRTIS} to I_{IR1} depends on the topography, there is no single factor that can be used to achieve this conversion. Given that using a scaling factor that depends on the topography might introduce unwanted altitude vs radiance trends in the data we do not correct the IR1 radiances further down to the level of I_{IR1}. This is why, while retrieving the temperature from IR1 observations, we use the I_{VIRTIS} look-up table calculated at 1017 nm. However, the scaling of IR1 radiances down to I_{IR1} level might be attempted in future, given that the maximum variation of ratio of I_{VIRTIS} to I_{IR1} is less than 0.3% which is much lesser compared to the actual noise present in the data.

6.1.2. The retrieval method

We use an approximate method to derive the surface temperature from the observed and simulated radiances. Consider a pixel of the observation having the radiance value R_{obs}, and an altitude z. At this altitude, we find the simulated radiance R_{sim} through interpolation from our look-up table (I_{VIRTIS}). This look-up table is generated by using the VIRA temperature profile (Seiff et al., 1985) as the input to the radiative transfer model (Section 5.2). This profile is denoted by $T_{VIRA}(z)$. We then find the relative deviation δR of observed radiance R_{obs} and simulated radiance R_{sim} as shown in Equation 6.1

$$\delta \mathrm{R} = \frac{\mathrm{R_{obs}} - \mathrm{R_{sim}}}{\mathrm{R_{sim}}} \tag{6.1}$$

The 1.02 µm window shows a small contribution from the atmospheric emission (Meadows and Crisp, 1996). Hence, the radiance at the top of the atmosphere is approximately proportional to the thermal emission at the surface. Therefore we can use the relative partial derivative of the Planck function to estimate the partial derivative of the observed radiance with respect to surface temperature. Thus, the relative partial derivative of the Planck function ($\delta B/\delta T(z)$) is calculated from a finite difference at the input surface temperature $T_{VIRA}(z)$ as shown in Equation 6.2.

$$\delta \mathrm{B}/\delta \mathrm{T(z)} = \frac{((\mathrm{B(T_{VIRA}(z) + 0.5K) - B(T_{VIRA}(z) - 0.5K)})/1\mathrm{K})}{\mathrm{B(T_{VIRA}(z))}} \tag{6.2}$$

Next, the temperature deviation from the input of the radiative transfer model (VIRA temperature profile) is found out as shown below,

$$\delta \mathrm{T} = \delta \mathrm{T}/\delta \mathrm{B} * \delta \mathrm{R} \tag{6.3}$$

Lastly, we add the input temperature at the altitude z ($T_{VIRA}(z)$) to the temperature deviation calculated above (δT) to get the value of surface temperature ($T_{surface}(z)$). This process is repeated for all the pixels in the observation (in a parallel way) to retrieve the surface temperatures from the entire observation. In future, the raditiave transfer model (Section 5.2) could be used to derive the partial derivative of observed radiance with respect to the surface temperature.

6.1.3. Sensitivity Study

For the final simulations, we use a surface emissivity of 0.8 which is consistent with the previous assumptions about average emissivity of the surface of Venus (Hashimoto, 2003, Haus and Arnold, 2010, Mueller et al., 2020). The cloud model is the same as that described in Section 5.3. Mueller et al. (2020) achieve a good fit for the VIRTIS spectra at $\alpha = 1.9e - 10\mathrm{cm}^{-1}\mathrm{amagat}^{-2}$ and a cloud factor of 1.75. This look-up table used by Mueller et al. (2020) is termed as the look-up table 'A' and the surface temperatures retrieved from the VIRTIS dataset by using this look-table are termed as 'VIRTIS A' temperatures. To get a better idea of the trend of the deviation of the retrieved surface temperatures, it is represented in the form of mean (shown by the dashed line) and standard deviation (shown by the blue shaded area) instead of showing the scatter plot in Figure 6.3. Here, first the data is binned into altitude intervals of 500 m and then the mean and standard deviation is calculated for all the altitude bins.

From Figure 5.13, it can be seen that our model produces higher radiance as compared with the look-up table from Mueller et al. (2020) for the emissivity of 0.8. Thus, we vary the value of α as 1.9e-10, 2.5e-10,4e-10 $\mathrm{cm}^{-1}\mathrm{amagat}^{-2}$ to increase the optical thickness and lower the radiance to match the look-up table from Mueller et al. (2020). For the above three values of α, we generate three look-up tables by changing the starting elevation from 0 to 16 km (w.r.t 6048 km) and convolving with the VIRTIS Band 0 profile as discussed in Subsection 6.1.1. These tables are termed as look-up table 'B',

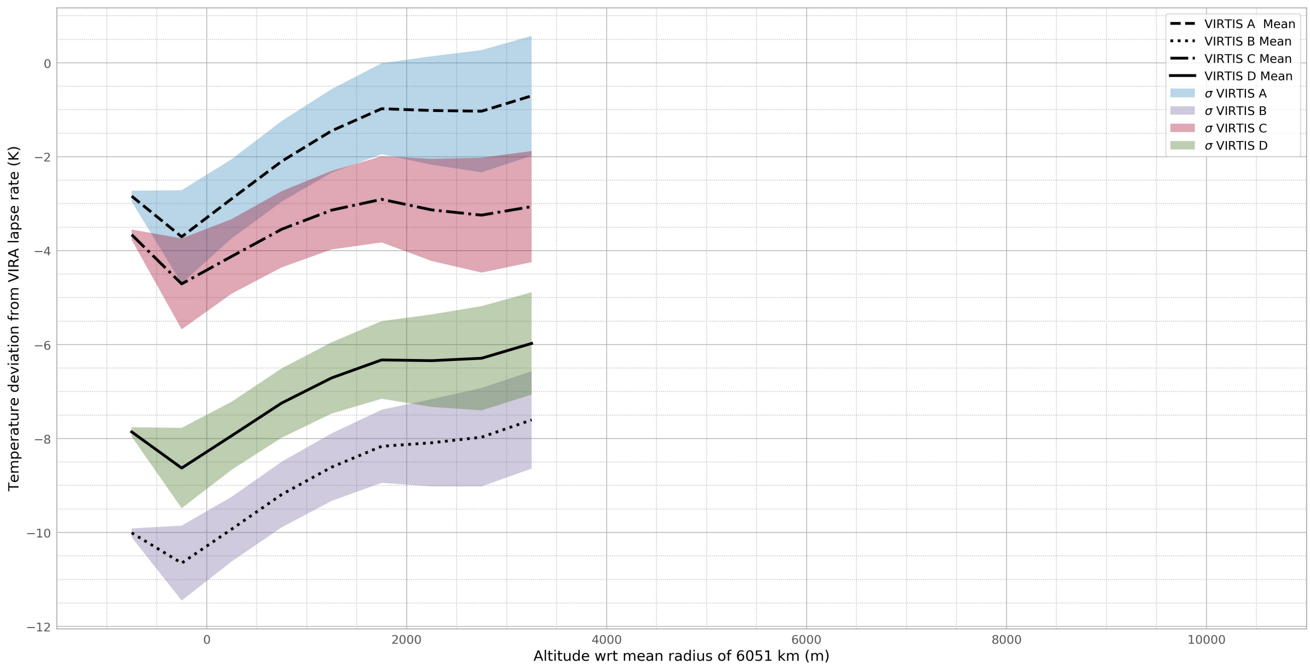

Figure 6.3: The plot of temperature deviation against the altitude for the temperature values retrieved from the VIRTIS dataset for the four cases discussed in the text.

'C', and 'D', for the α = 1.9 e-10, 2.5e-10,4e-10 $cm^{-1}amagat^{-2}$ respectively. The 'VIRTIS B', 'VIRTIS C', 'VIRTIS D' are the temperature results generated for the VIRTIS data by using these look-up tables.

As observed from Figure 6.3, the 'VIRTIS B' shows an offset of ~7 K in the retrieved temperatures as compared with 'VIRTIS A'. When increasing the α to 2.5e-10 $cm^{-1}amagat^{-2}$ (VIRTIS C), the offset with respect to the 'VIRTIS A' profiles is reduced to ~5.5 K. This offset is further reduced to ~2 K for α = 4e-10 $cm^{-1}amagat^{-2}$ (VIRTIS D). It can be observed that the increased value of α starts (slightly) affecting the trend of temperature deviation above 1.75 km altitude for 'VIRTIS D'. This effect seems to be smaller that 1 K per km.

Here, retrieving the absolute temperatures is not the aim given the uncertainty in the factors like α, surface emissivity emissivity, and cloud optical thickness, etc. However, we are primarily interested in the profile of temperature deviation with respect to the altitude which is similar for both the look-up tables 'A' and 'B' results. Thus, while retrieving the surface temperatures we use the look-up table 'B' and subtract the offset of 7 K from the temperature results.

6.2. Comparison of observed and modeled radiances

We now compare the altitude vs. radiance plot of the calibrated IR1 dataset (level 3h) against the results from the simulations and VIRTIS data in Figure 6.4. In spite of having large noise, a relation between altitude vs radiance of the IR1 data (green scatter points) can be directly distinguished which is similar to that of the simulated radiances (blue trend line) and the VIRTIS data (black scatter points).

When comparing VIRTIS radiances with the simulation results, it can be observed that the VIRTIS dataset shows a linear relation whereas simulation results show a non-linear relation. The difference between VIRTIS and simulated radiances is nearly constant for the altitude range of 3 to 1.75 km. This difference increases below the altitude of 1.75 km. This results in increasingly higher temperature deviation going from 1.75 to - 0.5 km altitudes as shown in Figure 6.3 and Figure 6.6.

The IR1 radiance plot (green) shows the presence of the interpolation noise (discussed in Subsection 4.3.3). The loose scatter points present on both sides of the scatter plot are due to this noise. They can be particularly observed in the lower-left corner of the plot, i.e., for altitude range 0 to 2 km and radiance range 0 to 0.02 $W/m^2/sr/\mu m$. Given a large number of data points in the 0-2 km altitude range, the effect of the interpolation noise on the trend of retrieved surface temperatures in this altitude range can be neglected.

This noise can also be observed at an altitude range of 9-10 km and a radiance range of 0.01 to 0.02 $W/m^2/sr/\mu m$ in the form of loose scatter points. Here, it is particularly important given that at this altitude the number of data points is much smaller compared to lower altitudes and thus even a small number of affected data points result in higher standard deviation in the temperature retrieval results shown in Figure 6.6.

Although the IR1 dataset has the above-mentioned interpolation noise and residual noise due to stray light, the dataset still shows the expected non-linear trend with the topography. The dataset extends the range of altitudes observed by

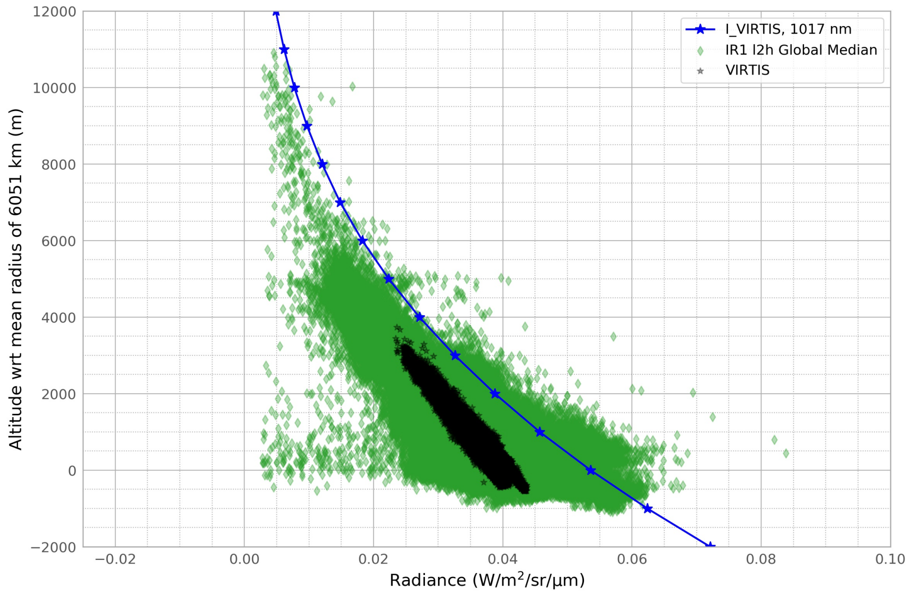

Figure 6.4: Altitude vs Radiance plot of calibrated (level 3h) IR1 dataset and VIRTIS Dataset shown by green diamonds and black stars respectively. The blue trend line represents the results from our atmospheric radiative transfer model at $\alpha = 1.9e-10\text{cm}^{-1}\text{amagat}^{-2}$, cloud factor= 1.75, and using the VIRTIS profile at 1017 nm.

VIRTIS and thus it is highly important for making conclusions about the temperature profile for the altitudes above 3 km.

6.3. Surface Temperatures

Figure 6.5 (A) and (B) show the surface temperature maps retrieved using the VIRTIS and IR1 dataset shown in Figure 6.4 respectively with a resolution of 0.5°x0.5°. The surface temperatures are retrieved by using the process described in Section 6.3. As discussed earlier, VIRTIS primarily observed the southern hemisphere, and thus only southern latitudes are shown in Figure 6.5. It can also be observed that the topography in this region shows altitudes less than 3 km. On the other hand, IR1 primarily observed the equatorial belt and some Northern and Southern regions. The IR1 observations cover all the main highlands, e.g., the Aphrodite Terra situated along the equator from ~50 to 150° East, the Ishtar Terra along with the Maxwell Montes (~11 km tall) in the North, and the Maat Montes (~8 km tall) at 160° West. The location of Ishtar Terra, Aphrodite Terra, and Maat Mons is shown by the blue, red, and violet rectangles in Figure 6.5 (C) respectively. Thus, IR1 data extends the coverage over much more of the surface, thereby extending the range of observed surface altitudes as compared to VIRTIS data.

Figure 6.5 (C) shows surface temperatures that are expected by using the VIRA temperature profile (Seiff et al., 1985). This plot is generated by interpolating the VIRA temperature profile over the Magellan topography dataset (GTDR) (Ford and Pettengill, 1992). Lastly, Figure 6.5 (D) shows the temperature results generated by the LMD Venus GCM with N_2 gradient (Lebonnois et al., 2018). For all the high altitude regions, i.e., Ishtar Terra, Aphrodite Terra the GCM temperature map (Figure 6.5 (D)) shows lower temperatures than the VIRA temperature map (Figure 6.5 (C)). While the temperatures for areas with an altitude range of 1-3 km appear to be similar, the area below 1 km altitude shows lower temperatures than the VIRA map. To get a clear idea of the temperature profiles the VIRA temperature map is subtracted from the GCM temperature map (for corresponding areas) and the scatter plot of this difference against the altitude is shown in Figure 6.6 by the red scatter points. This plot confirms that the temperature in the GCM maps is similar to that from the VIRA map for 1-3 km altitude range and the temperature difference increases we traverse toward higher and lower altitude ranges making a convex shape. Similarly, the scatter plot of temperature deviation of LMD Venus GCM model (without the N_2 gradient) with respect to VIRA temperature profile against the altitude is shown by the green scatter points in Figure 6.6. It should be noted that both the GCM plots have been adjusted for the temperature offset as explained in Section 2.5.

Comparing the VIRTIS temperature map (Figure 6.5 (A)) with the VIRA temperature map (Figure 6.5 (C)), it can be observed that the areas in the VIRTIS map with altitudes above 1 km show similar temperatures while the areas below 1 km altitude show lower temperatures than on the VIRA map. This can also be observed by the dashed line in the plot of temperature deviation against altitude, shown in Figure 6.6. Here, the scatter plot of temperature deviation against the altitude is shown in the form of mean and standard deviation of the data binned for the altitude interval of 500 m, similar to that discussed in Subsection 6.1.3. The VIRTIS trend line follows the scatter plot of GCM without the composition gradient till the altitude of 3 km. However, it is difficult to make a strong comment supporting either of the GCMs given that the scatter plots of both GCMs start diverging after an altitude of 3 km.

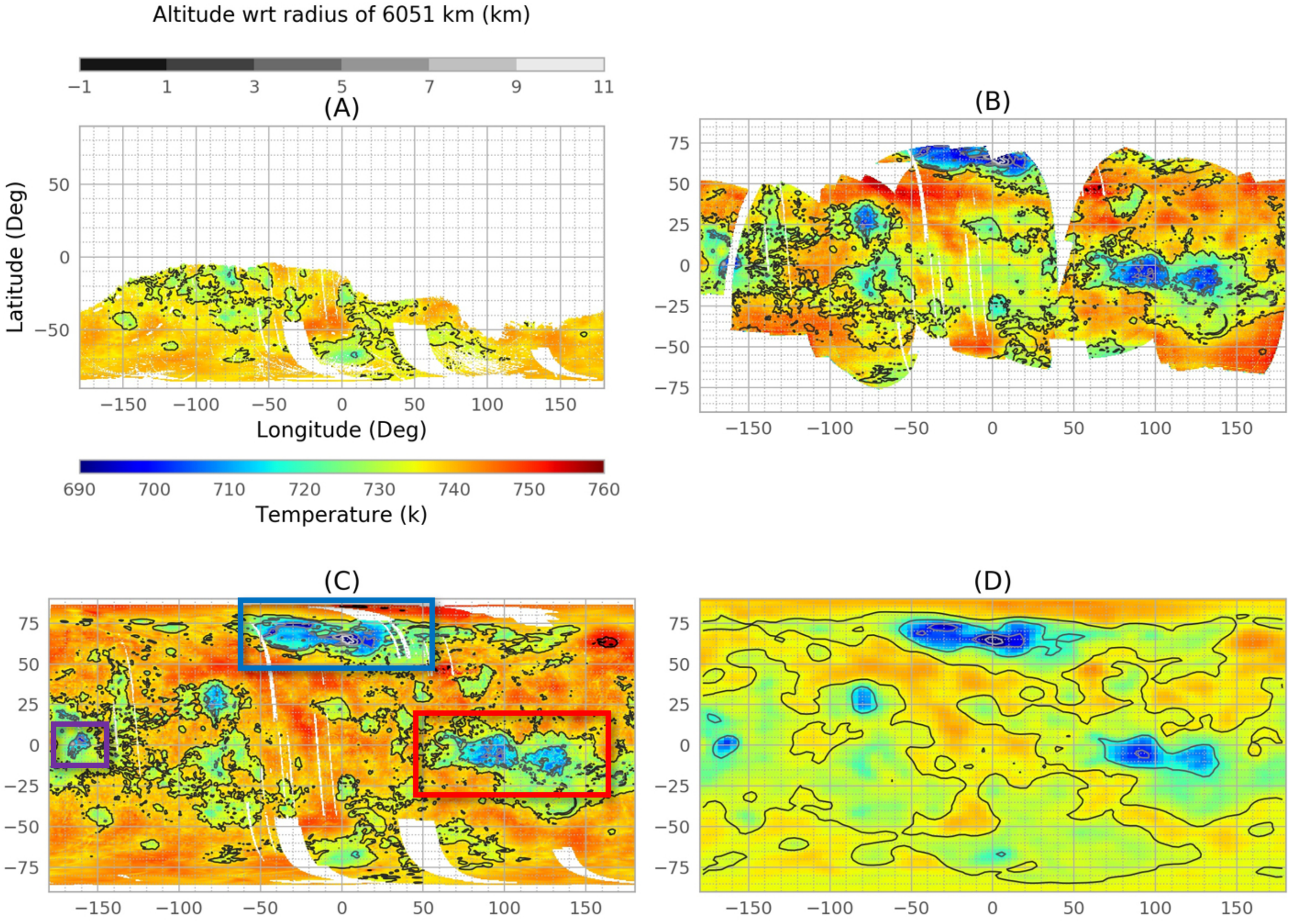

Figure 6.5: The maps of the surface temperature retrieved from (A) VIRTIS dataset and (B) from the IR1 dataset. (C) shows the surface temperature map based on the VIRA temperature lapse rate. (D) surface temperature map from LMD Venus GCM with the N_2 gradient. The altitude and temperature scales shown in sub-figure (A) apply to all four plots. Similarly, the y axis represents the latitude and the x axis represents the longitude for all the sub-figures. The blue, red, and violet rectangles in (C) show the location of Ishtar Terra, Aphrodite Terra, and Maat Mons respectively. The enlarged versions of all of these maps are provided in Appendix D.

For the altitudes above 3 km, i.e., the Aphrodite Terra and the Ishtar Terra, the IR1 map (Figure 6.5 (B)) shows lower temperature values than VIRA Map similar to that of GCM Map (Figure 6.5 (D)). Thus, the IR1 temperature map is more similar to the map of GCM with N_2 gradient for the altitudes higher than 3 km. The area covered by altitudes higher than 9 km is very small (the Maxwell Montes), and thus, a direct comparison via simple observation is difficult. For the altitude range 1-3 km, the IR1 temperature values are nearly similar to the VIRA map, however, there is much variability on the map. So we now refer to the plot of temperature deviation with respect to VIRA against altitude in Figure 6.6. The dash-dotted line shows the mean IR1 temperature deviation values and the blue shaded area shows the corresponding standard deviation. The IR1 trend line follows the scatter plot of GCM with N_2 gradient till 3 km altitude above which there is a dip in the temperature of about 5 K with respect to VIRA. The trend line continues showing variability above this altitude. It can be observed that the standard deviation of the IR1 temperature data increases with the altitude. The reason for this is that at lower altitudes changes in radiance produce smaller temperature deviation, however, as we go to higher altitudes a smaller change in radiance produces much higher temperature deviation. For example, the high standard deviation of the temperature values at 10 km altitude comes from the interpolation noise as discussed in Section 6.2.

Next, we extract the data at specific locations on the IR1 map to compare the regional and global trends. In the IR1 dataset, Aphrodite Terra was observed the maximum number of times (20 out of 45) and was relatively less affected by the stray light. Thus, this region produces the data with the lowest standard deviation. The temperature map of Aphrodite Terra, the corresponding radiance vs altitude scatter plot, and the temperature deviation vs altitude plots are shown separately in Figure D.6. The red solid line in Figure 6.6 shows the trend line from the Aphrodite Terra. While the line follows the scatter plot of GCM with N_2 gradient till 3 km altitude, a similar dip in the temperatures at 4-5 km altitudes is observed. Similarly, the blue and violet lines in Figure 6.6 show the temperature deviations from the Ishar Terra and Maat Mons respectively. These are shown separately in Figure D.7 and Figure D.8. A similar dip in the temperature in the 4-5 km altitude range can be observed from these trend lines. The mean surface temperature profile of these geographically separate regions is consistent within 2 K for the 4-5 km altitude range and within 6 K at other altitudes. Since it is expected

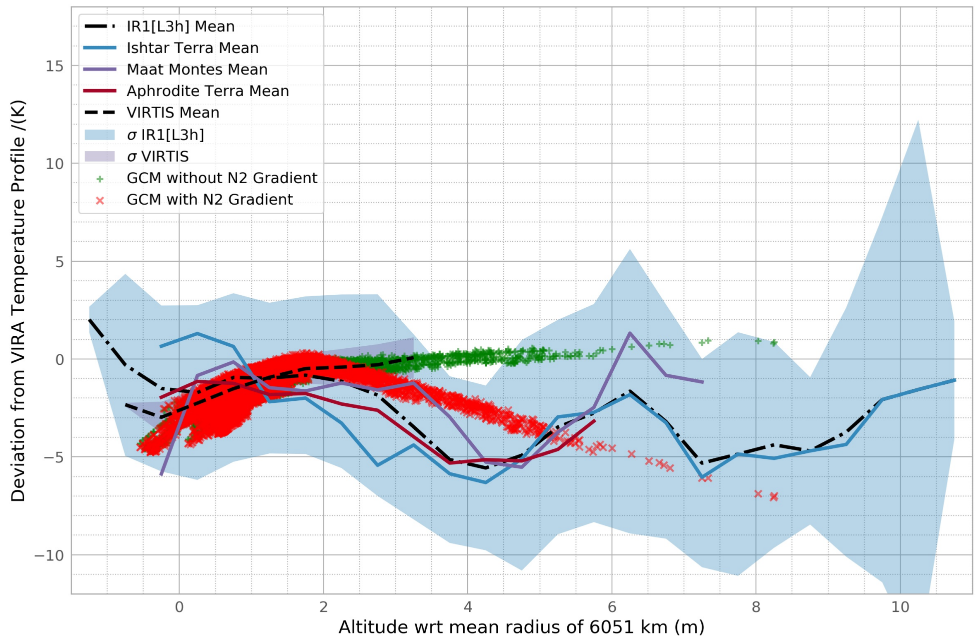

Figure 6.6: The plot of temperature deviation from VIRA temperature profile against the altitude. The red and green scatter points show the data from LMD Venus GCM with and without the N_2 gradient. The the mean and standard deviation of VIRTIS and IR1 temperature deviation data is shown by black dashed line with violet shaded area, and black dash-dotted line with blue shaded area respectively. The means of the temperature deviation data over the Ishtar Terra, Maat Mons, and the Aphrodite Terra are shown by the blue, violet, and red trend lines respectively.

(in absence of large emissivity variations) that the surface temperature profile is globally similar, e.g. as shown by the red or green scatter plots of GCM results, this similarity in the surface temperature profiles of geographically separate regions indicates much of the scatter in IR1 data is random noise.

6.4. Discussion

From the altitude vs. radiance scatter plot shown in Figure 6.4, it can be observed that spread of the IR1 data (green scatter points) increases from higher altitudes (~6km) to the lower altitudes (~0km). The primary reason for this is that the low lands cover a larger surface area than the high lands and thereby show a larger scatter. For all the altitude ranges the IR1 data show a much higher standard deviation than the VIRTIS data (black points). Apart from the residual effect of the straylight, this behaviour is primarily attributed to the number of observations along with the cloud optical thickness variations. The VIRTIS data had up to 200 observations of the same location for generating the global median map (Mueller et al., 2009), whereas, the IR1 data has a maximum of 20 observations of few locations and usually this number is less than 5. The IR1 data situation would have been much better if the initial orbit insertion had worked. Secondly, the VIRTIS data was corrected for the cloud optical thickness variations using the simultaneous observations in 1.31 µm window and this correction was not possible for IR1 data, given the lack of simultaneous observations in 1.31, 1.7 or 2.3 µm windows. Haus et al. (2014) report the drop in latitudinal average of the cloud optical thickness near the latitude of 50° South and North from VIRTIS data. Some areas in the IR1 temperature map (Figure 6.5(B)), near the 50 ° S and N latitude and below 1 km altitude, show higher temperatures than the VIRA temperature map. Thus, a correction for the latitudinal cloud optical thickness variations based on the average of the cloud optical thickness from Haus et al. (2014) might reduce the spread of the IR1 dataset in the lower altitude ranges. Secondly, as discussed in Section 5.3, the H_2O abundance also affects the radiances in 1 µm window. Among others, Hashimoto et al. (2008) and Arney et al. (2014) have derived maps of special variability of H_2O using spectroscopic imaging observations in the atmospheric window at 1.18 µm, with the reported variations between 20 to 45 ppmv. Such variability in H_2O abundance could be a minor cause for the higher spread of IR1 data. Lastly, Grieger et al. (2004) indicate a possible presence of a haze layer between 1-2 km altitude range. The effect of variability within this layer on the radiances observed at the top of the atmosphere warrants further studies and might be a possible cause behind the variability of near-IR radiances.

As observed from Figure 6.6, a temperature lapse rate smaller than VIRA is observed between 0 to 2 km altitude range by both the VIRTIS and IR1 dataset, and both the GCM results. This agrees with the results from Meadows and Crisp (1996), which show a smaller lapse rate in the range of -7 to -7.5 K/km than the VIRA lapse rate of -8 to -8.5 K/km (Seiff et al., 1985). The temperature deviation of VIRTIS data follows the GCM results till 3 km altitude and this topography range is not enough to make firm conclusions about supporting either of the two GCM results. The IR1 temperature data appears to follow the trend of the GCM model with the N_2 gradient, however, the temperature drops faster near the altitude range of 4-5 km. Following this dip in the temperature, the profile fluctuates as we go for the higher altitude range with a second dip in temperatures near the 7-9 km altitude range. Thus, both the VIRTIS and IR1 temperatures do not exactly match either of the two GCM results which indicates that the situation could be much more complicated than a simple gradient in the composition of N_2 (or lack thereof) used in the modelling.

From the IR1 data, we find an increased lapse rate between the 2 to 4.5 km altitude range. However, this can be also interpreted in terms of a change in surface emissivity. It has been previously known that the radio-thermal emissivity of the highlands undergoes abrupt changes with a decrease in the value of emissivity up to the lowest of 0.6 (Klose et al., 1992). Various studies explain this anomaly by a change in the composition of minerals between low lands and high lands. The required minerals with high dielectric constants can be a result of temperature-dependent chemical weathering between the rocks and the atmosphere at high altitudes (Brossier et al., 2021). Similarly, Hashimoto et al. (2008) find the highlands having lower emissivity at 1.18 μm as compared to the low lands. However they note that his low emissivity would disappear if the temperature lapse rate were 1 K/km steeper than the VIRA profile, which is less than the deviations from VIRA derived here. The change in the lapse rate observed between 2 to 4 km altitude for the Aphrodite Terra (red line in Figure 6.6) roughly coincides with the radio-thermal emissivity anomaly. This anomaly, reported by Brossier and Gilmore (2021), is thought to be caused by the presence of ferroelectric minerals for the altitude above 2 km at the Aphrodite Terra. The temperature deviation trend observed for Maat montes shows a similar change in lapse rate, but for the altitudes between 3.25 to 4.25 km. However, Klose et al. (1992) report that the Maat Mons notably lacks the emissivity anomaly due to weathering, indicating that this volcano is relatively young. Brossier et al. (2021) report the smaller volumes of ferroelectric minerals as compared to other volcanic mountains (Ozza and Sapas Montes) supporting the idea of younger volcanic activity. Thus, a change in the surface temperature profile for the same altitude range over two geographically different regions with different composition indicates that the IR1 surface temperature profile is dominated by atmospheric temperature.

6.5. Proposed Future Research

As described in the earlier section, the surface of Venus shows the regional variation of emissivity, based on a possible difference in mineral composition. Earlier studies of surface emissivity retrieval used the surface temperature determined by the VIRA temperature profile. However, this might result in an altitude-dependent bias in the estimation of surface emissivity (Hashimoto et al., 2009). Mueller et al. (2020) use the VIRTIS temperature map to analyze the surface emissivity variations. As discussed in Section 6.3 The IR1 temperature map extends both the surface coverage and the altitude range as compared to the VIRTIS map. This map can be used for future studies dealing with surface emissivity variations.

The IR1 temperature vs altitude profile significantly differs from the GCM with N_2 gradient for between the altitude range of 4-5 km. This indicates the actual situation in the atmosphere could be even different than the N_2 gradient used in the GCM by Lebonnois et al. (2018). Brackett et al. (1995) discuss a possible transport of volatile metal vapors from the hot lowlands to cold highlands on Venus. It would be interesting to test if the transport of volatile metal vapors can result in a composition gradient that can explain the IR1 temperature vs altitude profile.

The temperature profile of the deep atmosphere could also be important for studies dealing with the variations in the rotation rate of Venus. Recent studies (Margot et al., 2021, Navarro et al., 2018) talk about the mechanism of transfer of the atmospheric angular momentum to the solid planet to explain the variation in the rotation rate. The temperature profile of the lower atmosphere affects the planetary boundary layer and is a key parameter required for the GCM used for these studies. Thus, periodic (ground-based) observations of the nightside of Venus to observe the variations in temperature vs altitude profile might provide an important input to such studies.

As described above, an accurate surface temperature profile is important for Venusian studies. However, the instruments onboard the past missions were not optimized for the observations in the surface observing atmospheric windows. For studies dealing with surface emission, simultaneous observations in the 0.95 to 1.31 μm range are required. However, the IR1 instrument was an imager and VIRTIS was the flight spare for the Rosetta comet orbiter (Coradini et al., 1999). Thus, both were not optimized for surface emissivity studies. Based on the work described in this report, we would like to highlight the need for an instrument optimized for the atmospheric windows of Venus. An example could be the proposed Venus Emissivity Mapper (VEM) instrument (Helbert et al., 2013).

7

CONCLUSION

Given the extreme conditions in the lower atmosphere of Venus, various in-situ missions faced instrumental failures. As a result, the thermal structure of the deep atmosphere, particularly below 12 km is not well known (Limaye et al., 2018a). In the Venus International Reference Atmosphere (VIRA), the thermal structure of the atmosphere below 12 km altitude was constructed by extrapolating the data recorded in the upper atmosphere (Seiff et al., 1985). The VeGa-2 lander provided the only high resolution temperature measurements below 12 km altitude (Linkin et al., 1986). However, these measurements indicated a region of high instability below 7 km altitude. Given a lack of physical explanations, these measurements were not included in VIRA (Seiff, 1987). Lebonnois and Schubert (2017) tried to explain this temperature profile by proposing a gradient in the composition of the atmosphere in which the abundance of Nitrogen gradually decreases to zero at the surface. Various experimental and numerical studies were carried out to investigate the possibility of this gradient, however, they could not provide a physical explanation for this theory (Section 2.4).

Lebonnois et al. (2018) include this composition gradient in their global circulation model (GCM) (Lebonnois et al., 2010). A remarkable deviation is observed between the surface temperature results obtained from the GCM with and without the composition gradient above 3 km altitude as shown in Section 2.5. In the absence of a new in-situ mission, we have used the previous near-IR observations of Venus nightside to test the theory of the composition gradient. The VIRTIS instrument onboard the Venus Express provides a high resolution temperature map of the Southern hemisphere (Mueller et al., 2009). However, the altitude range of the observed surface is limited to be below 4 km. The high lands on Venus are observed by the IR1 imager onboard the Akatsuki orbiter in the same atmospheric window at 1 µm. Thus, the IR1 dataset is essential for this study.

However, due to the initial orbit insertion failure of the Akatsuki mission, the geometry at the time of observation was not ideal for the IR1 imager. Thus, the observations of the nightside were heavily contaminated by the bright straylight coming from the dayside. Also, the calibration had an uncertainty of ±67%. To study the noise in the observations, we first start by using the raw observations (level 1b) and recreating the entire data processing pipeline given by Iwagami et al. (2018) up to level 2c. We then divide the observations into two categories. The 'Type I' observations represent the observations that directly observed the bright dayside of Venus (along with the nightside). The 'Type II' observations represent the observations that were taken by applying a specific procedure to push the dayside of the Venus out of the field of view and only look at the nightside of Venus. We find that the Type I observations are characterized by a heavy bias along with a vertical gradient in the images. Vignetting is also observed in the sky portion of some images. The Type II observations primarily show a nonlinear gradient in the areas that are closer to the dayside of Venus.

After extensive experimentation, we develop a correction procedure to reduce the noise present in IR1 dataset (Section 4.3). This procedure includes sequentially a row-wise sky brightness correction, limb darkening correction, selective masking, and a residual bias correction. Lastly, the observations are cross-calibrated such that they align with the processed VIRTIS data from Mueller et al. (2020). At every step, the level of the dataset is appended, taking the dataset from level 2c (processed as per Iwagami et al. (2018)) to level 2h (final calibration as per our processing pipeline). The level 3c to 3h represent the corresponding observations projected on the map of Venus. Care is taken at every processing step not to introduce any artifacts, however, mapping of the level 2 f data introduces an interpolation noise. Fortunately, this noise has no major impact on the data or the retrieved surface temperatures.

To retrieve the surface temperatures from the near-IR observations, we develop an atmospheric radiative transfer model. At the core of this model, we use the radiative transfer code from Wauben et al. (1994) that calculates the polarized thermal radiation in a plane-parallel, vertically inhomogeneous atmosphere. We construct the atmosphere using VIRA pressure, temperature, gravity, and density profiles. Rayleigh scattering is considered throughout the atmosphere. We use the full four modal particle size distribution for clouds (Mode 1, 2, 2', 3). We use the cloud model from Barstow et al. (2012) for current study and also include the cloud model from Haus et al. (2013) for future studies. A separate Mie scattering code from De Rooij and Stap (1984) is used to calculate the scattering matrices of cloud particles in generalized spherical functions that required by the radiative transfer code. We model the absorption by considering eight major absorbing species (CO_2, H_2O CO, HCL, HF, H_2S, OCS, and SO_2). Appropriate high temperature spectral line datasets from Pollack et al. (1993), Rothman et al. (2010) are used with line shape from Bezard et al. (2009). The thermal emission is calculated as per the Planck's Law. To simulate the effect of topography on Venus, we generate the results in the form of a look-up table in which we vary the starting altitude of the atmosphere from 0 to 16 km altitude with respect to 6048 km planetary radius. We validate our model based on the look-up table used by Mueller et al. (2020) which was generated using the model described in Tsang et al. (2008). This table gives the values of thermal emission from the atmosphere of Venus for the topography range of 2 to 10 km altitude with respect to 6048 km. We find a close match for the radiance vs altitude relation from both the models. At the same time, we also report a difference in radiance vs surface emissivity relation obtained from both the models. Our atmospheric radiative transfer model can be further used for future studies dealing with surface emissivity variations, gas abundance retrieval, and also for simulations of the radiation field as observed by a descending probe in the atmosphere of Venus.

The thermal emission from the atmosphere of Venus is affected by multiple parameters (Section 5.3) out of which several parameters like the collision induced absorption (Subsection 5.2.6) and surface emissivity are unknown. We use the values of these parameters that were derived by Mueller et al. (2020) by fitting with the spectral measurements from VIRTIS data to generate the final look-up table (look-up table 'B' from Subsection 6.1.3). The final look-up table is then used to retrieve the surface temperature values from the VIRTIS and IR1 global radiance maps. We then represent the results in the form of a trendline of the deviation of the surface temperature values with respect to the VIRA temperature profile against the surface altitude. The results from the global circulation models are also presented in a similar format.

We find that the VIRITS and IR1 temperature trendlines agree with the results from both the GCMs from 0 to 2 km altitude, indicating a lapse rate lower than VIRA as previously indicated by Meadows and Crisp (1996). Because the VIRTIS temperatures are limited to altitudes up to 3.5 km, there is not enough information to firmly support either of the GCM trends. Above 2 km altitude, the IR1 temperatures fall even faster than the GCM with N_2 gradient and achieve a maximum deviation of ~5 K from VIRA profile between 4-5 km and 7-9 km altitude range. This indicates that the situation could be even more complex than a simple gradient in the composition of N_2.

At ~4 km altitude, a radiothermal emissivity anomaly is reported by observations from Magellan mission (Klose et al., 1992). To identify a possible relationship between the IR1 temperature drop at 4-5 km altitude range with this anomaly, we compare the temperature profiles from geographically different high lands on the surface of Venus, namely the Aphrodite Terra, the Ishtar Terra, and the Maat Mons, all of which show a similar deviation around the 4 km altitude region. While the Aphrodite Terra and the Ishtar Terra report the radiothermal emissivity anomaly, the Maat Mons does not show this anomaly. Yet we find similar temperature profiles from all three regions which indicates that the IR1 temperature profile is dominated by atmospheric temperature at that altitude.

In this way, we find that the IR1 temperatures differ significantly from the temperatures from GCM with and without the N_2 gradient. Thus, IR1 temperature profile neither fully supports the theory of N_2 gradient nor it endorses the lack of a composition gradient. This can be researched further by checking if the transport of volatile metal vapors (Brackett et al., 1995) can describe a composition gradient that can explain the IR1 temperature profile. Also, the IR1 surface temperature profile can be further used for surface emissivity variation studies, similar to the VIRTIS profile used by Mueller et al. (2020). As described in Section 6.5, the temperature profile generated from near-IR observations could also be an important input for the studies dealing with rotation rate variations of Venus. While both the IR1 and VIRTIS instruments were not optimized for the observation of surface emission, an optimized instrument could significantly improve the scientific returns. Based on this, we highlight the need of future near-IR observations with an instrument optimized for the surface observing atmospheric windows of Venus.

Bibliography

P. Alfeld, *A trivariate clough-tocher scheme for tetrahedral data,* Computer Aided Geometric Design **1**, 169 (1984).

D. A. Allen, *The dark side of Venus,* Icarus **69**, 221 (1987).

D. A. Allen, *Venus,* IAU Circular **4962** (1990).

D. A. Allen and J. W. Crawford, *Cloud structure on the dark side of Venus,* Nature **307**, 222 (1984).

B. M. Andreichikov, *Chemical composition and structure of Venus clouds from results of X-ray radiometric experiments made with the Vega 1 and Vega 2 automatic interplanetary stations.* KosIs **25**, 737 (1987).

G. Arney, V. Meadows, D. Crisp, S. J. Schmidt, J. Bailey, and T. Robinson, *Spatially resolved measurements of H2O, HCl, CO, OCS, SO2, cloud opacity, and acid concentration in the Venus near-infrared spectral windows,* Journal of Geophysical Research E: Planets **119**, 1860 (2014).

G. Arnold, D. Kappel, R. Haus, M. Ivanov, and L. T. Pedroza, *Retrieval and study of near-infrared surface emissivity maps of Themis Regio on Venus with VIRTIS-M (Venus Express),* in *European Planetary Science Congress*, Vol. 10 (2015) p. 160.

G. Arnold, R. Haus, D. Kappel, P. Drossart, and G. Piccioni, *Venus surface data extraction from VIRTIS/Venus Express measurements: Estimation of a quantitative approach,* Journal of Geophysical Research **113**, E00B10 (2008).

V. S. Avduevskij, N. F. Borodin, V. P. Burtsev, Y. V. Malkov, M. Y. Marov, S. F. Morozov, M. K. Rozhdestvenskij, R. S. Romanov, S. S. Sokolov, V. G. Fokin, Z. P. Cheremukhina, and V. I. Shkirina, *Automatic stations Venera 9 and Venera 10 - operating of the reentry vehicles and measurement of the atmosphere's parameters.* KosIs **14**, 655 (1976).

V. S. Avduevskij, N. F. Borodin, V. N. Vasil'Ev, A. G. Godnev, V. P. Karyagin, V. A. Kover'yanov, V. M. Kovtunenko, R. S. Kremnev, V. M. Pavlova, M. K. Rozhdestvenskij, V. I. Serbin, K. G. Sukhanov, G. R. Uspenskij, Z. P. Cheremukhina, V. S. Avduevskij, N. F. Borodin, V. N. Vasil'Ev, A. G. Godnev, V. P. Karyagin, V. A. Kover'yanov, V. M. Kovtunenko, R. S. Kremnev, V. M. Pavlova, M. K. Rozhdestvenskij, V. I. Serbin, K. G. Sukhanov, G. R. Uspenskij, and Z. P. Cheremukhina, *Analysis of the results of measurements of the parameters of the Venus atmosphere at the landing sites of Venera 11 and Venera 12.* KosIs **17**, 655 (1979).

V. S. Avduevsky, A. G. Godnev, Y. V. Zakharov, and others, *Estimation of Physical-Mechanic Properties of the Venusian Soil at Landing of the VENERA-13,-14,* Kosmicheskiye Issledovaniya **21**, 331 (1983).

J. Bailey, S. Chamberlain, D. Crisp, and V. S. Meadows, *Near infrared imaging spectroscopy of Venus with the Anglo-Australian Telescope,* Planetary and Space Science **56**, 1385 (2008).

K. H. Baines, S. K. Atreya, M. A. Bullock, D. H. Grinspoon, P. Mahaffy, C. T. Russell, G. Schubert, and K. Zahnle, *The Atmospheres of the Terrestrial Planets: Clues to the Origins and Early Evolution of Venus, Earth, and Mars,* Comparative Climatology of Terrestrial Planets (2013), 10.2458/azu_uapress_9780816530595-ch006.

K. H. Baines, G. Bellucci, J. P. Bibring, R. H. Brown, B. J. Buratti, E. Bussoletti, F. Capaccioni, P. Cerroni, R. N. Clark, A. Coradini, D. P. Cruikshank, P. Drossart, V. Formisano, R. Jaumann, Y. Langevin, D. L. Matson, T. B. McCord, V. Mennella, R. M. Nelson, P. D. Nicholson, B. Sicardy, C. Sotin, G. B. Hansen, J. J. Aiello, and S. Amici, *Detection of Sub-Micron Radiation from the Surface of Venus by Cassini/VIMS,* Icarus **148**, 307 (2000).

R. J. Barber, J. Tennyson, G. J. Harris, and R. N. Tolchenov, *A high-accuracy computed water line list,* Monthly Notices of the Royal Astronomical Society **368**, 1087 (2006).

J. K. Barstow, C. C. Tsang, C. F. Wilson, P. G. Irwin, F. W. Taylor, K. McGouldrick, P. Drossart, G. Piccioni, and S. Tellmann, *Models of the global cloud structure on Venus derived from Venus Express observations,* Icarus **217**, 542 (2012).

A. T. Basilevsky, E. V. Shalygin, D. V. Titov, W. J. Markiewicz, F. Scholten, T. Roatsch, M. A. Kreslavsky, L. V. Moroz, N. I. Ignatiev, B. Fiethe, B. Osterloh, and H. Michalik, *Geologic interpretation of the near-infrared images of the surface taken by the Venus Monitoring Camera, Venus Express,* Icarus **217**, 434 (2012).

D. R. Bates, *Rayleigh scattering by air,* Planetary and Space Science **32**, 785 (1984).

J. F. Bell, D. Crisp, P. G. Lucey, T. A. Ozoroski, W. M. Sinton, S. C. Willis, and B. A. Campbell, *Spectroscopic observations of bright and dark emission features on the night side of venus,* Science **252**, 1293 (1991).

B. Bézard, C. De Bergh, D. Crisp, and J. P. Maillard, *The deep atmosphere of Venus revealed by high-resolution nightside spectra,* Nature **345**, 508 (1990).

B. Bezard, C. C. Tsang, R. W. Carlson, G. Piccioni, E. Marcq, and P. Drossart, *Water vapor abundance near the surface of Venus from Venus Express/VIRTIS observations,* Journal of Geophysical Research E: Planets **114**, 1 (2009).

J. Blamont and B. Ragent, *Further results of the Pioneer Venus nephelometer experiment,* Science **205**, 67 (1979).

R. A. Brackett, B. Fegley, and R. E. Arvidson, *Volatile transport on Venus and implications for surface geochemistry and geology,* Journal of Geophysical Research **100**, 1553 (1995).

C. Brodbeck, N. Van-Thanh, J.-P. Bouanich, C. Boulet, A. Jean-Louis, B. Bezard, and C. de Bergh, *Measurements of pure CO ₂ absorption at high densities near 2.3 μm,* Journal of Geophysical Research **96**, 17497 (1991).

J. Brossier, M. S. Gilmore, K. Toner, and A. J. Stein, *Distinct Mineralogy and Age of Individual Lava Flows in Atla Regio, Venus Derived From Magellan Radar Emissivity,* Journal of Geophysical Research: Planets **126**, 1 (2021).

J. Brossier and M. S. Gilmore, *Variations in the radiophysical properties of tesserae and mountain belts on Venus: Classifi-

cation and mineralogical trends, Icarus **355**, 114161 (2021).
M. Buckley, *Parker Solar Probe Offers Stunning View of Venus | NASA,* (2021).
D. E. Burch, D. A. Gryvnak, R. R. Patty, and C. E. Bartky, *Absorption of Infrared Radiant Energy by CO_2 and H_2O IV Shapes of Collision-Broadened CO_2 Lines*,* Journal of the Optical Society of America **59**, 267 (1969).
B. A. Campbell, D. B. Campbell, L. M. Carter, J. F. Chandler, J. D. Giorgini, J. L. Margot, G. A. Morgan, M. C. Nolan, P. J. Perillat, and J. L. Whitten, *The mean rotation rate of Venus from 29years of Earth-based radar observations,* Icarus **332**, 19 (2019).
A. Cardesín-Moinelo, G. Piccioni, A. Migliorini, D. Grassi, V. Cottini, D. Titov, R. Politi, F. Nuccilli, and P. Drossart, *Global maps of Venus nightside mean infrared thermal emissions obtained by VIRTIS on Venus Express,* Icarus **343**, 113683 (2020).
R. W. Carlson, K. H. Baines, T. H. Encrenaz, F. W. Taylor, P. Drossart, L. W. Kamp, J. B. Pollack, E. Lellouch, A. D. Collard, S. B. Calcutt, D. Grinspoon, P. R. Weissman, W. D. Smythe, A. C. Ocampo, G. E. Danielson, F. P. Fanale, T. V. Johnson, H. H. Kieffer, D. L. Matson, T. B. McCord, and L. A. Soderblom, *Galileo infrared imaging spectroscopy measurements at Venus,* Science **253**, 1541 (1991).
S. Chamberlain, J. Bailey, D. Crisp, and V. Meadows, *Ground-based near-infrared observations of water vapour in the Venus troposphere,* Icarus **222**, 364 (2013).
A. Coradini, F. Capaccioni, P. Drossart, A. Semery, G. Arnold, and U. Schade, *Virtis: The imaging spectrometer of the Rosetta mission,* Advances in Space Research **24**, 1095 (1999).
D. Cordier, D. A. Bonhommeau, S. Port, V. Chevrier, S. Lebonnois, and F. García-Sánchez, *The Physical Origin of the Venus Low Atmosphere Chemical Gradient,* The Astrophysical Journal **880**, 82 (2019).
C. C. Counselman, S. A. Gourevitch, R. W. King, G. B. Loriot, and E. S. Ginsberg, *Zonal and meridional circulation of the lower atmosphere of Venus determined by radio interferometry,* Journal of Geophysical Research: Space Physics **85**, 8026 (1980).
D. Crisp, S. McMuldroch, S. K. Stephens, W. M. Sinton, B. Ragent, K. W. Hodapp, R. G. Probst, L. R. Doyle, D. A. Allen, and J. Ellas, *Ground-based near-infrared imaging observations of venus during the Galileo encounter,* Science **253**, 1538 (1991).
D. Crisp, V. S. Meadows, B. Bezard, C. D. Bergh, J.-P. Maillard, and F. P. Mills, *Ground-based near-infrared observations of the Venus nightside: 1.27-micron airglow from the upper atmosphe,* **101**, 4577 (1996).
D. Crisp, *Radiative forcing of the Venus mesosphere,* Icarus **67**, 484 (1986).
D. Crisp, *Radiative forcing of the Venus mesosphere. II. Thermal fluxes, cooling rates, and radiative equilibrium temperatures,* Icarus **77**, 391 (1989).
C. de Bergh, B. Bézard, D. Crisp, J. P. Maillard, T. Owen, J. Pollack, and D. Grinspoon, *Water in the deep atmosphere of Venus from high-resolution spectra of the night side,* Advances in Space Research **15**, 79 (1995).
J. F. de Haan, P. B. Bosma, and J. W. Hovenier, *The adding method for multiple scattering calculations of polarized light,* Astronomy and astrophysics (Berlin. Print) **183**, 371 (1987).
W. De Rooij and C. Stap, Van Der, *Expansion of Mie scattering matrices in generalized spherical functions,* Astronomy and astrophysics (Berlin. Print) **131**, 237 (1984).
P. Drossart and F. Montmessin, *The legacy of Venus Express: highlights from the first European planetary mission to Venus,* Astronomy and Astrophysics Review **23**, 1 (2015).
A. Dutt and S. S. Limaye, *Adiabatic Lapse Rate and Static Stability in the Venus Atmosphere calculated from Real Gas Mixture Models,* , 1 (2018).
R. Espanani, A. Miller, A. Busick, D. Hendry, and W. Jacoby, *Separation of N2/CO2 mixture using a continuous high-pressure density-driven separator,* Journal of CO2 Utilization **14**, 67 (2016).
L. W. Esposito, R. G. Knollenberg, M. Y. A. Marov, O. B. Toon, and R. R. TURCO, *The clouds and hazes of Venus,* in *Venus* (University of Arizona Press, 1983) p. 484.
L. W. Esposito, J. L. Bertaux, V. Krasnopolsky, V. I. Moroz, and L. V. Zasova, *Chemistry of lower atmosphere and clouds,* in *Venus II: Geology, Geophysics, Atmosphere, and Solar Wind Environment* (University of Arizona Press, Tucson, AZ, 1997) pp. 415–458.
V. Eymet, R. Fournier, J.-L. Dufresne, S. Lebonnois, F. Hourdin, and M. A. Bullock, *Net exchange parameterization of thermal infrared radiative transfer in Venus' atmosphere,* Journal of Geophysical Research **114**, E11008 (2009).
B. Fegley, G. Klingelhoefer, K. Lodders, and T. Widemann, *Geochemistry of surface-atmosphere interactions on Venus,* in *Venus II: Geology, Geophysics, Atmosphere, and Solar Wind Environment*, edited by S. Bougher, D. Hunten, and R. Phillips (University of Arizona Press, 1997) pp. 591–636.
P. G. Ford and G. H. Pettengill, *Venus topography and kilometer-scale slopes,* Journal of Geophysical Research **97**, 103 (1992).
I. Garate-Lopez and S. Lebonnois, *Latitudinal variation of clouds' structure responsible for Venus' cold collar,* Icarus **314**, 1 (2018).
P. J. Gierasch, B. SW, D. M. Hunten, and R. J. Phillips, *Venus II: Geology, Geophysics, Atmosphere, and Solar Wind Environment,* by SW Bougher, DM Hunten, RJ Phillips, University of Arizona Press, Tucson , 459 (1997).
I. E. Gordon, L. S. Rothman, C. Hill, R. V. Kochanov, Y. Tan, P. F. Bernath, M. Birk, V. Boudon, A. Campargue, K. V. Chance, B. J. Drouin, J. M. Flaud, R. R. Gamache, J. T. Hodges, D. Jacquemart, V. I. Perevalov, A. Perrin, K. P. Shine, M. A. Smith,

J. Tennyson, G. C. Toon, H. Tran, V. G. Tyuterev, A. Barbe, A. G. Császár, V. M. Devi, T. Furtenbacher, J. J. Harrison, J. M. Hartmann, A. Jolly, T. J. Johnson, T. Karman, I. Kleiner, A. A. Kyuberis, J. Loos, O. M. Lyulin, S. T. Massie, S. N. Mikhailenko, N. Moazzen-Ahmadi, H. S. Müller, O. V. Naumenko, A. V. Nikitin, O. L. Polyansky, M. Rey, M. Rotger, S. W. Sharpe, K. Sung, E. Starikova, S. A. Tashkun, J. V. Auwera, G. Wagner, J. Wilzewski, P. Wcisło, S. Yu, and E. J. Zak, *The HITRAN2016 molecular spectroscopic database,* Journal of Quantitative Spectroscopy and Radiative Transfer **203**, 3 (2017).

D. Grassi, R. Politi, N. I. Ignatiev, C. Plainaki, S. Lebonnois, P. Wolkenberg, L. Montabone, A. Migliorini, G. Piccioni, and P. Drossart, *The Venus nighttime atmosphere as observed by the VIRTIS-M instrument. Average fields from the complete infrared data set,* Journal of Geophysical Research: Planets **119**, 837 (2014).

B. Grieger, N. I. Ignatiev, N. M. Hoekzema, and H. U. Keller, *Indication of a near surface cloud layer on Venus from reanalysis of Venera 13/14 spectrophotometer data,* in *European Space Agency, (Special Publication) ESA SP*, 544 (ESA Publications Division, Noordwijk, Netherlands, 2004) pp. 63–70.

D. H. Grinspoon, J. B. Pollack, B. R. Sitton, R. W. Carlson, L. W. Kamp, K. H. Baines, T. Encrenaz, and F. W. Taylor, *Probing Venus's cloud structure with Galileo NIMS,* Planetary and Space Science **41**, 515 (1993).

R. M. Haberle, R. T. Clancy, F. Forget, M. D. Smith, and R. W. Zurek, *The Atmosphere and Climate of Mars* (Cambridge University Press, 2017) pp. 1–574.

J. E. Hansen and L. D. Travis, *Light scattering in planetary atmospheres,* Space Science Reviews **16**, 527 (1974).

G. L. Hashimoto, *On observing the compositional variability of the surface of Venus using nightside near-infrared thermal radiation,* Journal of Geophysical Research **108**, 5109 (2003).

G. L. Hashimoto, M. Roos-Serote, S. Sugita, M. S. Gilmore, L. W. Kamp, R. W. Carlson, and K. H. Baines, *Felsic highland crust on Venus suggested by Galileo Near-Infrared Mapping Spectrometer data,* Journal of Geophysical Research **113**, E00B24 (2008).

G. L. Hashimoto, M. Roos-Serote, S. Sugita, M. S. Gilmore, L. W. Kamp, R. W. Carlson, and K. H. Baines, *Felsic highland crust on Venus suggested by Galileo Near-Infrared Mapping Spectrometer data,* Journal of Geophysical Research E: Planets **114**, 1 (2009).

R. Haus, D. Kappel, and G. Arnold, *Self-consistent retrieval of temperature profiles and cloud structure in the northern hemisphere of Venus using VIRTIS/VEX and PMV/VENERA-15 radiation measurements,* Planetary and Space Science **89**, 77 (2013).

R. Haus, D. Kappel, and G. Arnold, *Atmospheric thermal structure and cloud features in the southern hemisphere of Venus as retrieved from VIRTIS/VEX radiation measurements,* Icarus **232**, 232 (2014).

R. Haus, D. Kappel, and G. Arnold, *Radiative energy balance of Venus: An approach to parameterize thermal cooling and solar heating rates,* Icarus **284**, 216 (2017).

R. Haus and G. Arnold, *Radiative transfer in the atmosphere of Venus and application to surface emissivity retrieval from VIRTIS/VEX measurements,* Planetary and Space Science **58**, 1578 (2010).

J. Helbert, N. Müller, A. Maturilli, R. Nadalini, S. Smrekar, P. D'Incecco, and M. D'Amore, *Observing the surface of Venus after VIRTIS on VEX: new concepts and laboratory work,* Infrared Remote Sensing and Instrumentation XXI **8867**, 88670C (2013).

D. Hendry, A. Miller, N. Wilkinson, M. Wickramathilaka, R. Espanani, and W. Jacoby, *Exploration of high pressure equilibrium separations of nitrogen and carbon dioxide,* Journal of CO2 Utilization **3-4**, 37 (2013).

S. L. Hess, *Static stability and thermal wind in an atmosphere of variable composition: Applications to Mars,* Journal of Geophysical Research **84**, 2969 (1979).

C. W. B. W. S. F. L. H. H. J. m. J. F. N. R. L. T. Y. S. W. H. W. Hilsenrath, Joseph; Beckett, *Pergamon Press* (Pergamon Press, New York, 1960).

F. Hourdin, I. Musat, S. Bony, P. Braconnot, F. Codron, J. L. Dufresne, L. Fairhead, M. A. Filiberti, P. Friedlingstein, J. Y. Grandpeix, G. Krinner, P. LeVan, Z. X. Li, and F. Lott, *The LMDZ4 general circulation model: Climate performance and sensitivity to parametrized physics with emphasis on tropical convection,* Climate Dynamics **27**, 787 (2006).

J. N. Howard, D. E. Burch, and D. Williams, *Infrared Transmission of Synthetic Atmospheres* II Absorption by Carbon Dioxide,* Journal of the Optical Society of America **46**, 237 (1956).

R. Hueso, J. Peralta, I. Garate-Lopez, T. V. Bandos, and A. Sánchez-Lavega, *Six years of Venus winds at the upper cloud level from UV, visible and near infrared observations from VIRTIS on Venus Express,* Planetary and Space Science **113-114**, 78 (2015).

D. M. Hunten, L. Colin, T. M. Donahue, and V. I. Moroz, *vens* (1983).

P. G. Irwin, N. A. Teanby, R. de Kok, L. N. Fletcher, C. J. Howett, C. C. Tsang, C. F. Wilson, S. B. Calcutt, C. A. Nixon, and P. D. Parrish, *The NEMESIS planetary atmosphere radiative transfer and retrieval tool,* Journal of Quantitative Spectroscopy and Radiative Transfer **109**, 1136 (2008).

N. Iwagami, S. Ohtsuki, K. Tokuda, N. Ohira, Y. Kasaba, T. Imamura, H. Sagawa, G. L. Hashimoto, S. Takeuchi, M. Ueno, and S. Okumura, *Hemispheric distributions of HCl above and below the Venus' clouds by ground-based 1.7 μm spectroscopy,* Planetary and Space Science **56**, 1424 (2008).

N. Iwagami, S. Takagi, S. Ohtsuki, M. Ueno, K. Uemizu, T. Satoh, T. Sakanoi, and G. L. Hashimoto, *Science requirements and description of the 1 μm camera onboard the Akatsuki Venus Orbiter,* Earth, Planets and Space **63**, 487 (2011).

N. Iwagami, T. Sakanoi, G. L. Hashimoto, K. Sawai, S. Ohtsuki, S. Takagi, K. Uemizu, M. Ueno, S. Kameda, S. y. Murakami,

M. Nakamura, N. Ishii, T. Abe, T. Satoh, T. Imamura, C. Hirose, M. Suzuki, N. Hirata, A. Yamazaki, T. M. Sato, M. Yamada, Y. Yamamoto, T. Fukuhara, K. Ogohara, H. Ando, K. i. Sugiyama, H. Kashimura, and T. Kouyama, *Initial products of Akatsuki 1-μm camera,* Earth, Planets and Space **70**, 1 (2018).

E. P. James, O. B. Toon, and G. Schubert, *A numerical microphysical model of the condensational Venus cloud,* Icarus **129**, 147 (1997).

J. M. Jenkins, P. G. Steffes, D. P. Hinson, J. D. Twicken, and G. L. Tyler, *Radio Occultation Studies of the Venus Atmosphere with the Magellan Spacecraft. 2. Results from the October 1991 Experiments,* Icarus **110**, 79 (1994).

L. W. Kamp and F. W. Taylor, *Radiative-transfer models of the night side of Venus,* Icarus **86**, 510 (1990).

L. W. Kamp, F. W. Taylor, and S. B. Calcutt, *Structure of Venus's atmosphere from modelling of night-side infrared spectra,* Nature **336**, 360 (1988).

D. Kappel, *MSR, a multi-spectrum retrieval technique for spatially-temporally correlated or common Venus surface and atmosphere parameters,* Journal of Quantitative Spectroscopy and Radiative Transfer **133**, 153 (2014).

D. Kappel, G. Arnold, R. Haus, G. Piccioni, and P. Drossart, *Refinements in the data analysis of VIRTIS-M-IR Venus nightside spectra,* Advances in Space Research **50**, 228 (2012).

D. Kappel, R. Haus, and G. Arnold, *Error analysis for retrieval of Venus' IR surface emissivity from VIRTIS/VEX measurements,* Planetary and Space Science **113-114**, 49 (2015).

D. Kappel, G. Arnold, and R. Haus, *Multi-spectrum retrieval of Venus IR surface emissivity maps from VIRTIS/VEX nightside measurements at Themis Regio,* Icarus **265**, 42 (2016).

V. V. Kerzhanovich, *The atmospheric dynamics of Venus according to Doppler measurements by the Venera entry probes.* in *Venus*, edited by D. Hunten, L. Colin, T. Donahue, and V. Moroz (The university of Arizona press, 1983) pp. 766–778.

A. J. Kliore, V. I. Moroz, and G. M. Keating, *The Venus International Reference Atmosphere,* Advances in Space Research **5**, 1 (1985).

A. J. Kliore, *Recent results on the Venus atmosphere from pioneer Venus radio occultations,* Advances in Space Research **5**, 41 (1985).

A. J. Kliore and I. R. Patel, *Thermal structure of the atmosphere of Venus from Pioneer Venus radio occultations,* Icarus **52**, 320 (1982).

K. B. Klose, J. A. Wood, and A. Hashimoto, *Mineral equilibria and the high radar reflectivity of Venus mountaintops,* Journal of Geophysical Research **97** (1992), 10.1029/92je01865.

J. Knicely and R. R. Herrick, *Evaluation of the bandwidths and spatial resolutions achievable with near-infrared observations of Venus below the cloud deck,* Planetary and Space Science **181**, 104787 (2020).

R. G. Knollenberg and D. M. Hunten, *The microphysics of the clouds of Venus: Results of the Pioneer Venus Particle Size Spectrometer Experiment,* Journal of Geophysical Research **85**, 8039 (1980).

R. G. Knollenberg, *A reexamination of the evidence for large, solid particles in the clouds of Venus,* Icarus **57**, 161 (1984).

S. Lebonnois, F. Hourdin, V. Eymet, A. Crespin, R. Fournier, and F. Forget, *Superrotation of Venus' atmosphere analyzed with a full general circulation model,* Journal of Geophysical Research E: Planets **115**, 1 (2010).

S. Lebonnois and G. Schubert, *The deep atmosphere of Venus and the possible role of density-driven separation of CO 2 and N 2,* Nature Geoscience **10**, 473 (2017).

S. Lebonnois, J. Burgalat, P. Rannou, and B. Charnay, *Titan global climate model: A new 3-dimensional version of the IPSL Titan GCM,* Icarus **218**, 707 (2012).

S. Lebonnois, N. Sugimoto, and G. Gilli, *Wave analysis in the atmosphere of Venus below 100-km altitude, simulated by the LMD Venus GCM,* Icarus **278**, 38 (2016).

S. Lebonnois, G. Schubert, F. Forget, and A. Spiga, *Planetary boundary layer and slope winds on Venus,* Icarus **314**, 149 (2018).

S. Lebonnois, G. Schubert, T. Kremic, L. M. Nakley, K. G. Phillips, J. Bellan, and D. Cordier, *An experimental study of the mixing of CO2 and N2 under conditions found at the surface of Venus,* Icarus **338**, 113550 (2020).

J. Lecacheux, P. Drossart, P. Laques, F. Deladerriére, and F. Colas, *Detection of the surface of Venus at 1.0 μm from ground-based observations,* Planetary and Space Science **41**, 543 (1993).

C. Lécuyer, L. Simon, and F. Guyot, *Comparison of carbon, nitrogen and water budgets on Venus and the Earth,* Earth and Planetary Science Letters **181**, 33 (2000).

P. Ledoux, *On stellar models with convection and discontinuity of the mean molecular weight.* The Astronomical Journal **52**, 155 (1947a).

P. Ledoux, *Stellar models with convection and with discontinuity of the mean molecular weight,* The Astrophysical Journal **105**, 305 (1947b).

Y. J. Lee, D. V. Titov, S. Tellmann, A. Piccialli, N. Ignatiev, M. Pätzold, B. Häusler, G. Piccioni, and P. Drossart, *Vertical structure of the Venus cloud top from the VeRa and VIRTIS observations onboard Venus Express,* Icarus **217**, 599 (2012).

E. Lellouch, T. Clancy, D. Crisp, A. J. Kliore, D. Titov, and S. W. Bougher, *Monitoring of mesospheric structure and dynamics,* Venus II , 295 (1997).

S. R. Lewis, J. Dawson, S. Lebonnois, and M. Yamamoto, *Modeling efforts,* in *Towards Understanding the Climate of Venus: Applications of Terrestrial Models to Our Sister Planet*, Vol. 11 (Springer New York, 2013) pp. 111–127.

T. M. Lillesand and R. W. Kiefer, *Remote sensing and image interpretation.* (1979).

S. S. Limaye, S. Lebonnois, A. Mahieux, M. Pätzold, S. Bougher, S. Bruinsma, S. Chamberlain, R. T. Clancy, J. C. Gérard,

G. Gilli, D. Grassi, R. Haus, M. Herrmann, T. Imamura, E. Kohler, P. Krause, A. Migliorini, F. Montmessin, C. Pere, M. Persson, A. Piccialli, M. Rengel, A. Rodin, B. Sandor, M. Sornig, H. Svedhem, S. Tellmann, P. Tanga, A. C. Vandaele, T. Widemann, C. F. Wilson, I. Müller-Wodarg, and L. Zasova, *The thermal structure of the Venus atmosphere: Intercomparison of Venus Express and ground based observations of vertical temperature and density profiles,* Icarus **294**, 124 (2017).

S. S. Limaye, D. Grassi, A. Mahieux, A. Migliorini, S. Tellmann, and D. Titov, *Space Science Reviews*, Vol. 214 (The Author(s), 2018).

S. S. Limaye, R. Mogul, D. J. Smith, A. H. Ansari, G. P. Słowik, and P. Vaishampayan, *Venus' spectral signatures and the potential for life in the clouds,* Astrobiology **18**, 1181 (2018b).

S. S. Limaye, S. Watanabe, A. Yamazaki, M. Yamada, T. Satoh, T. M. Sato, M. Nakamura, M. Taguchi, T. Fukuhara, T. Imamura, T. Kouyama, Y. J. Lee, T. Horinouchi, J. Peralta, N. Iwagami, G. L. Hashimoto, S. Takagi, S. Ohtsuki, S. y. Murakami, Y. Yamamoto, K. Ogohara, H. Ando, K. i. Sugiyama, N. Ishii, T. Abe, C. Hirose, M. Suzuki, N. Hirata, E. F. Young, and A. C. Ocampo, *Venus looks different from day to night across wavelengths: morphology from Akatsuki multispectral images,* Earth, Planets and Space **70** (2018c), 10.1186/s40623-018-0789-5.

V. M. Linkin, J. E. Blamont, A. N. Lipatov, S. I. Devyatkin, A. V. Dyachkov, and S. P. Ignatova, *Vertical Thermal Structure in the Venus Atmosphere from Provisional VEGA-2 Temperature and Pressure Data,* Soviet Astronomy Letters **12**, 40 (1986).

E. Marcq, B. Bézard, P. Drossart, G. Piccioni, J. M. Reess, and F. Henry, *A latitudinal survey of CO, OCS, H2O, and SO2 in the lower atmosphere of Venus: Spectroscopic studies using VIRTIS-H,* Journal of Geophysical Research E: Planets **114**, 1 (2009).

E. Marcq, B. Bézard, T. Encrenaz, and M. Birlan, *Latitudinal variations of CO and OCS in the lower atmosphere of Venus from near-infrared nightside spectro-imaging,* Icarus **179**, 375 (2005).

E. Marcq, F. P. Mills, C. D. Parkinson, and A. C. Vandaele, *Composition and Chemistry of the Neutral Atmosphere of Venus,* Space Science Reviews **214** (2018), 10.1007/s11214-017-0438-5.

J.-L. Margot, D. B. Campbell, J. D. Giorgini, J. S. Jao, L. G. Snedeker, F. D. Ghigo, and A. Bonsall, *Spin state and moment of inertia of Venus,* (2021), 10.1038/s41550-021-01339-7.

W. J. Markiewicz, D. V. Titov, N. Ignatiev, H. U. Keller, D. Crisp, S. S. Limaye, R. Jaumann, R. Moissl, N. Thomas, L. Esposito, S. Watanabe, B. Fiethe, T. Behnke, I. Szemerey, H. Michalik, H. Perplies, M. Wedemeier, I. Sebastian, W. Boogaerts, S. F. Hviid, C. Dierker, B. Osterloh, W. Böker, M. Koch, H. Michaelis, D. Belyaev, A. Dannenberg, M. Tschimmel, P. Russo, T. Roatsch, and K. D. Matz, *Venus Monitoring Camera for Venus Express,* Planetary and Space Science **55**, 1701 (2007a).

W. J. Markiewicz, D. V. Titov, N. Ignatiev, H. U. Keller, D. Crisp, S. S. Limaye, R. Jaumann, R. Moissl, N. Thomas, L. Esposito, S. Watanabe, B. Fiethe, T. Behnke, I. Szemerey, H. Michalik, H. Perplies, M. Wedemeier, I. Sebastian, W. Boogaerts, S. F. Hviid, C. Dierker, B. Osterloh, W. Böker, M. Koch, H. Michaelis, D. Belyaev, A. Dannenberg, M. Tschimmel, P. Russo, T. Roatsch, and K. D. Matz, *Venus Monitoring Camera for Venus Express,* Planetary and Space Science **55**, 1701 (2007b).

V. S. Meadows and D. Crisp, *Ground-based near-infrared observations of the Venus nightside: The thermal structure and water abundance near the surface,* Journal of Geophysical Research: Planets **101**, 4595 (1996).

V. Meadows, *Ground based near-IR observations of the surface of Venus,* International Colloquim on Venus , 70 (1992).

G. L. Mellor and T. Yamada, *Development of a turbulence closure model for geophysical fluid problems,* Reviews of Geophysics **20**, 851 (1982).

J. F. Moore, *Infrared absorption of carbon dioxide at high densities with application to the atmosphere of Venus*, Ph.D. thesis, Columbia University, New York (1971).

V. I. Moroz, *The atmosphere of Venus,* Space Science Reviews **29**, 3 (1981).

N. I. Moskalenko, I. A. Ilin, S. N. Parzhin, L. V. Rodionov, N. I. Moskalenko, I. A. Ilin, S. N. Parzhin, and L. V. Rodionov, *Pressure-induced infrared radiation absorption in atmospheres,* FizAO **15**, 912 (1979).

N. Mueller, J. Helbert, G. L. Hashimoto, C. C. C. Tsang, S. Erard, G. Piccioni, and P. Drossart, *Correlations between Venus nightside near infrared emissions measured by VIRTIS/Venus Express and Magellan radar data,* European Planetary Science Congress 2008, Proceedings of the conference held 21-25 September, 2008 in Münster, Germany. Online at http://meetings.copernicus.org/epsc2008, p.421 , 1 (2008).

N. Mueller, J. Helbert, G. L. Hashimoto, C. C. Tsang, S. Erard, G. Piccioni, and P. Drossart, *Venus surface thermal emission at 1 μm in VIRTIS imaging observations: Evidence for variation of crust and mantle differentiation conditions,* Journal of Geophysical Research E: Planets **114**, 1 (2009).

N. T. Mueller, S. Smrekar, J. Helbert, E. Stofan, G. Piccioni, and P. Drossart, *Search for active lava flows with VIRTIS on Venus Express,* Journal of Geophysical Research: Planets **122**, 1021 (2017).

N. T. Mueller, C. C. C. Tsang, S. Lebonnois, and S. Smrekar, *Regional Venus Surface Temperature Variations in Models and Infrared Observations Motivation : Observing the surface in Near Infrared,* 49th Lunar and Planetary Science Conference , 10 (2018).

N. T. Mueller, S. E. Smrekar, and C. C. Tsang, *Multispectral surface emissivity from VIRTIS on Venus Express,* Icarus **335**, 113400 (2020).

S. Murakami, S. Ohtsuki, S. Kameda, K. McGouldrick, Y. Yamamoto, and G. L. Hashimoto, *Venus Climate Orbiter Akatsuki IR1 Calibrated Data v1.0, VCO-V-IR1-3-CDR-V1.0,e,* (2018).

M. Nakamura, T. Imamura, N. Ishii, T. Abe, Y. Kawakatsu, C. Hirose, T. Satoh, M. Suzuki, M. Ueno, A. Yamazaki, N. Iwagami, S. Watanabe, M. Taguchi, T. Fukuhara, Y. Takahashi, M. Yamada, M. Imai, S. Ohtsuki, K. Uemizu, G. L. Hashimoto, M. Takagi, Y. Matsuda, K. Ogohara, N. Sato, Y. Kasaba, T. Kouyama, N. Hirata, R. Nakamura, Y. Yamamoto, T. Horinouchi, M. Yamamoto, Y. Y. Hayashi, H. Kashimura, K. I. Sugiyama, T. Sakanoi, H. Ando, S. Y. Murakami, T. M. Sato, S. Takagi, K. Nakajima, J. Peralta, Y. J. Lee, J. Nakatsuka, T. Ichikawa, K. Inoue, T. Toda, H. Toyota, S. Tachikawa, S. Narita, T. Hayashiyama, A. Hasegawa, and Y. Kamata, *AKATSUKI returns to Venus,* Earth, Planets and Space **68** (2016), 10.1186/s40623-016-0457-6.

T. Navarro, G. Schubert, and S. Lebonnois, *Atmospheric mountain wave generation on Venus and its influence on the solid planet's rotation rate,* Nature Geoscience **11**, 487 (2018).

G. M. Nielson, *A Method for Interpolating Scattered Data Based Upon a Minimum Norm Network,* Mathematics of Computation **40**, 253 (1983).

K. Ogohara, T. Kouyama, H. Yamamoto, N. Sato, M. Takagi, and T. Imamura, *Automated cloud tracking system for the Akatsuki Venus Climate Orbiter data,* Icarus **217**, 661 (2012).

K. Ogohara, M. Takagi, S. y. Murakami, T. Horinouchi, M. Yamada, T. Kouyama, G. L. Hashimoto, T. Imamura, Y. Yamamoto, H. Kashimura, N. Hirata, N. Sato, A. Yamazaki, T. Satoh, N. Iwagami, M. Taguchi, S. Watanabe, T. M. Sato, S. Ohtsuki, T. Fukuhara, M. Futaguchi, T. Sakanoi, S. Kameda, K. i. Sugiyama, H. Ando, Y. J. Lee, M. Nakamura, M. Suzuki, C. Hirose, N. Ishii, and T. Abe, *Overview of Akatsuki data products: definition of data levels, method and accuracy of geometric correction,* Earth, Planets and Space **69** (2017), 10.1186/s40623-017-0749-5.

S. Ohtsuki, N. Iwagami, H. Sagawa, M. Ueno, Y. Kasaba, T. Imamura, K. Yanagisawa, and E. Nishihara, *Distributions of the Venus 1.27-μm O2 airglow and rotational temperature,* Planetary and Space Science **56**, 1391 (2008).

K. F. Palmer and D. Williams, *Optical Constants of Sulfuric Acid; Application to the Clouds of Venus?* Applied Optics **14**, 208 (1975).

P. N. Peplowski, D. J. Lawrence, and J. T. Wilson, *Chemically distinct regions of Venus's atmosphere revealed by measured N2 concentrations,* Nature Astronomy , 2 (2020).

J. Peralta, Y. J. Lee, K. McGouldrick, H. Sagawa, A. Sánchez-Lavega, T. Imamura, T. Widemann, and M. Nakamura, *Overview of useful spectral regions for Venus: An update to encourage observations complementary to the Akatsuki mission,* Icarus **288**, 235 (2017).

V. I. Perevalov and S. A. Tashkun, *CDSD-296 (Carbon Dioxide Spectroscopic Databank): Updated and Enlarged Version for Atmospheric Applications,* (2008), 10.5281/ZENODO.17520.

G. Piccioni, P. Drossart, E. Suetta, M. Cosi, E. Ammannito, A. Barbis, R. Berlin, A. Boccaccini, G. Bonello, M. Bouye, F. Capaccioni, G. Cherubini, M. Dami, O. Dupuis, A. Fave, G. Filacchione, Y. Hello, F. Henry, S. Hofer, G. Huntzinger, R. Melchiorri, J. Parisot, C. Pasqui, G. Peter, C. Pompei, J. Reess, A. Semery, A. S. Team, and the VIRTIS Co-I, *VIRTIS: The Visible and Infrared Thermal Imaging Spectrometer,* European Space Agency, (Special Publication) ESA SP **SP**, 1 (2007).

R. T. Pierrehumbert, *Principles of planetary climate* (Cambridge University Press, 2010).

B. E. Poling, J. M. Prausnitz, and J. P. O'Connell, *Properties of Gases and Liquids, Fifth Edition,* (2001).

J. B. Pollack, J. B. Dalton, D. Grinspoon, R. B. Wattson, R. Freedman, D. Crisp, D. A. Allen, B. Bezard, C. DeBergh, L. P. Giver, Q. Ma, and R. Tipping, *Near-Infrared Light from Venus' Nightside: A Spectroscopic Analysis,* (1993).

B. Ragent, L. W. Esposito, M. G. Tomasko, M. Y. Marov, V. P. Shari, and V. N. Lebedev, *Particulate matter in the Venus atmosphere,* Advances in Space Research **5**, 85 (1985).

P. L. Read, J. Barstow, B. Charnay, S. Chelvaniththilan, P. G. Irwin, S. Knight, S. Lebonnois, S. R. Lewis, J. Mendonça, and L. Montabone, *Global energy budgets and 'Trenberth diagrams' for the climates of terrestrial and gas giant planets,* Quarterly Journal of the Royal Meteorological Society **142**, 703 (2016).

L. S. Rothman, I. E. Gordon, R. J. Barber, H. Dothe, R. R. Gamache, A. Goldman, V. I. Perevalov, S. A. Tashkun, and J. Tennyson, *HITEMP, the high-temperature molecular spectroscopic database,* Journal of Quantitative Spectroscopy and Radiative Transfer **111**, 2139 (2010).

L. S. Rothman, R. B. Wattson, R. Gamache, J. W. Schroeder, and A. McCann, *HITRAN HAWKS and HITEMP: high-temperature molecular database,* Atmospheric Propagation and Remote Sensing IV **2471**, 105 (1995).

A. Sánchez-Lavega, S. Lebonnois, T. Imamura, P. Read, and D. Luz, *The Atmospheric Dynamics of Venus,* Space Science Reviews **212**, 1541 (2017).

J. T. Schofield and F. W. Taylor, *Measurements of the mean, solar-fixed temperature and cloud structure of the middle atmosphere of Venus,* Quarterly Journal of the Royal Meteorological Society **109**, 57 (1983).

Schubert and G., *General circulation and the dynamical state of the Venus atmosphere*, in *Venus*, edited by D.M. Hunten, L. Colin, T.M. Donahue, and V.I. Moroz (University of Arizona Press, Tucson, AZ, 1983).

A. Seiff, *Further information on structure of the atmosphere of Venus derived from the VEGA Venus balloon and Lander mission,* Advances in Space Research **7**, 323 (1987).

A. Seiff, D. B. Kirk, R. E. Young, R. C. Blanchard, J. T. Findlay, G. M. Kelly, and S. C. Sommer, *Measurements of thermal structure and thermal contrasts in the atmosphere of Venus and related dynamical observations: Results From the four Pioneer Venus Probes,* Journal of Geophysical Research **85**, 7903 (1980).

A. Seiff, J. T. Schofield, A. J. Kliore, F. W. Taylor, S. S. Limaye, H. E. Revercomb, L. A. Sromovsky, V. V. Kerzhanovich, V. I. Moroz, and M. Y. Marov, *Models of the structure of the atmosphere of Venus from the surface to 100 kilometers altitude,* Advances in Space Research **5**, 3 (1985).

D. Singh, *Venus nightside surface temperature,* Scientific Reports **9**, 1 (2019).

R. Span and W. Wagner, *A new equation of state for carbon dioxide covering the fluid region from the triple-point temperature to 1100 K at pressures up to 800 MPa,* Journal of Physical and Chemical Reference Data **25**, 1509 (1996).

A. Spiga, F. Forget, S. R. Lewis, and D. P. Hinson, *Structure and dynamics of the convective boundary layer on mars as inferred from large-eddy simulations and remote-sensing measurements,* Quarterly Journal of the Royal Meteorological Society **136**, 414 (2010).

D. M. Stam, J. F. De Haan, J. W. Hovenier, and P. Stammes, *A fast method for simulating observations of polarized light emerging from the atmosphere applied to the oxygen-A band,* Journal of Quantitative Spectroscopy and Radiative Transfer **64**, 131 (2000).

F. Taylor and D. Grinspoon, *Climate evolution of Venus,* Journal of Geophysical Research **114** (2009), 10.1029/2008je003316.

F. W. Taylor, *The scientific exploration of Venus* (Cambridge University Press, New York, 2014) p. 295.

F. W. Taylor, R. Beer, M. T. Chahine, D. J. Diner, L. S. Elson, R. D. Haskins, D. J. McCleese, J. V. Martonchik, P. E. Reichley, S. P. Bradley, J. Delderfield, J. T. Schofield, C. B. Farmer, L. Froidevaux, J. Leung, M. T. Coffey, and J. C. Gille, *Structure and meteorology of the middle atmosphere of Venus: Infrared remote sensing from the Pioneer Orbiter,* Journal of Geophysical Research: Space Physics **85**, 7963 (1980).

F. W. Taylor, D. Crisp, and B. Bézard, *Near-infrared sounding of the lower atmosphere of Venus,* in *Venus II*, edited by S. W. Bougher, R. J. Phillips, and D. M. Hunten (Univ. of Ariz. Press, Tuscon, 1997) pp. 325–351,.

F. W. Taylor, *Venus before Venus Express,* Planetary and Space Science **54**, 1249 (2006).

F. W. Taylor, H. Svedhem, and J. W. Head, *Venus: The Atmosphere, Climate, Surface, Interior and Near-Space Environment of an Earth-Like Planet,* Space Science Reviews **214** (2018), 10.1007/s11214-018-0467-8.

S. Tellmann, B. Häusler, D. P. Hinson, G. L. Tyler, T. P. Andert, M. K. Bird, T. Imamura, M. Pätzold, and S. Remus, *Small-scale temperature fluctuations seen by the VeRa Radio Science Experiment on Venus Express,* Icarus **221**, 471 (2012).

S. Tellmann, M. Pätzold, B. Häusler, M. K. Bird, and G. L. Tyler, *Structure of the Venus neutral atmosphere as observed by the Radio Science experiment VeRa on Venus Express,* Journal of Geophysical Research **114**, E00B36 (2009).

D. V. Titov, H. Svedhem, D. Koschny, R. Hoofs, S. Barabash, J. L. Bertaux, P. Drossart, V. Formisano, B. Häusler, O. Korablev, W. J. Markiewicz, D. Nevejans, M. Pätzold, G. Piccioni, T. L. Zhang, D. Merritt, O. Witasse, J. Zender, A. Accomazzo, M. Sweeney, D. Trillard, M. Janvier, and A. Clochet, *Venus Express science planning,* Planetary and Space Science **54**, 1279 (2006).

D. V. Titov, W. J. Markiewicz, N. I. Ignatiev, L. Song, S. S. Limaye, A. Sanchez-Lavega, J. Hesemann, M. Almeida, T. Roatsch, K. D. Matz, F. Scholten, D. Crisp, L. W. Esposito, S. F. Hviid, R. Jaumann, H. U. Keller, and R. Moissl, *Morphology of the cloud tops as observed by the Venus Express Monitoring Camera,* Icarus **217**, 682 (2012).

D. V. Titov, N. I. Ignatiev, K. McGouldrick, V. Wilquet, and C. F. Wilson, *Space Science Reviews*, Vol. 214 (The Author(s), 2018).

M. V. Tonkov, N. N. Filippov, V. V. Bertsev, J. P. Bouanich, N. Van-Thanh, C. Brodbeck, J. M. Hartmann, C. Boulet, F. Thibault, and R. Le Doucen, *Measurements and empirical modeling of pure CO_2 absorption in the 23-μm region at room temperature: far wings, allowed and collision-induced bands,* Applied Optics **35**, 4863 (1996).

C. C. Tsang, P. G. Irwin, F. W. Taylor, and C. F. Wilson, *A correlated-k model of radiative transfer in the near-infrared windows of Venus,* Journal of Quantitative Spectroscopy and Radiative Transfer **109**, 1118 (2008).

B. A. Voronin, J. Tennyson, R. N. Tolchenov, A. A. Lugovskoy, and S. N. Yurchenko, *A high accuracy computed line list for the HDO molecule,* Monthly Notices of the Royal Astronomical Society **402**, 492 (2010).

W. M. F. Wauben, J. De Haan, and J. Hovenier, *A method for computing visible and infrared polarized monochromatic radiation in planetary atmospheres,* Astronomy and Astrophysics -Berlin- **282**, 277 (1994).

L. V. Zasova, V. I. Moroz, and V. M. Linkin, *Venera-15, 16 and VEGA mission results as sources for improvements of the venus reference atmosphere,* Advances in Space Research **17**, 171 (1996).

A

ATMOSPHERE OF VENUS

Planet Venus, being similar to Earth in terms of the size and the distance from the Sun, has a pressure-temperature profile resembling to that of Earth over its common range, i.e., till the pressure level of 1 bar (Taylor et al., 2018), as shown in Figure A.1. Here, the primary difference is the high temperature in the stratosphere of Earth due to the absorption of solar UV rays by the ozone layer, along with minor differences due to the high amount of CO_2 and the distance from the Sun. On Venus, due to lack of stratosphere, as we traverse downward from the 100 mb pressure level, the pressure and temperature increase till a surface pressure of 95 bar and temperature is 737 K at the mean planetary radius of 6051.5 km.

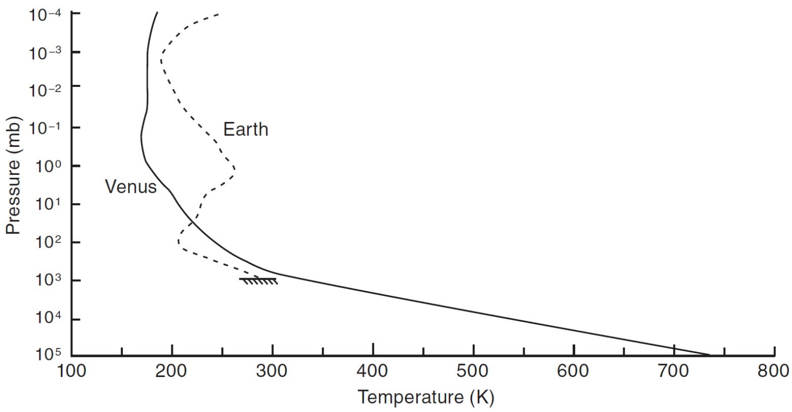

Figure A.1: Representative pressure-temperature profiles for Venus(Pioneer Venus) and Earth (Nimbus 7), from Taylor (2014)

The atmosphere primarily contains carbon dioxide (96%), nitrogen (3%), along with traces of argon, neon, water vapour, sulphur dioxide, etc. (Marcq et al., 2018). It is noteworthy that the net abundance of N_2 on Venus (3% at 90 bars) is not much different than that on Earth (78% at 1 bar). Also, the estimated total amount of CO_2 in the form of carbonates along with the amount present in the atmosphere on Earth is similar to that in the current atmosphere of Venus (Lécuyer et al., 2000). However, the deuterium to hydrogen fraction is about 100 times larger than that on Earth. The amount of Water Vapour is substantially low at about 30 ppm. On the other hand, the amount of Sulfur compounds is substantially high with about 150 ppm of SO_2 which indicates volcanic origin (Fegley et al., 1997). The hydrogen halides, most prominently HCL and HF, are present in trace amounts along with the noble gases including Ar, Kr, Xe, Ne are probably volcanic in origin (Baines et al., 2013).

This chapter gives a brief overview of the various aspects of the atmosphere of Venus that are important for Venusian studies. The thermal structure of the atmosphere from 100 km altitude to the surface is discussed in Section A.1. Next, the structure of clouds and hazes is described in Section A.2. Section A.3 highlights the important aspects of the atmospheric global circulation. The above-mentioned sections make use of certain atmospheric parameters. For details regarding these parameters, the reader is requested to refer to Appendix B.

A.1. THERMAL STRUCTURE OF THE ATMOSPHERE

The atmosphere of Venus exhibits a complex three-dimensional structure with different latitudinal and meridional temperature gradients at different altitudes which complicates the studies dealing with the deep atmosphere. It is primarily influenced by the global cloud cover, the global circulation, and the atmospheric composition (Limaye et al., 2018a). The atmospheric structure of Venus is shown in Figure A.2 (Titov et al., 2018). Derived from the Pioneer Venus and Venera landers, the color lines show mean temperature profiles at low (red), middle (blue) and high (green) latitudes with a single black line representing the temperature structure below 30 km. The typical vertical profile of aerosol extinction (Ragent et al., 1985) is given on the left. In the middle, the static stability profile (Seiff et al., 1985) from the VIRA model is shown.

In the **troposphere**, the temperature and pressure decreases monotonically from a surface value of ~ 735 K and ~ 95 bar till the tropopause value of 200 mbar and ~ 245 K (±35 K) (Kliore and Patel, 1982). Although only 2% of the incident sunlight reaches the surface, the surface temperature is high because of the extreme greenhouse effect and high surface pressures. This part of the atmosphere has large thermal inertia and thus, the diurnal temperature variations in this region are less than 1K (Seiff et al., 1985). The static stability (explained in Appendix B) starts increasing as we traverse downward from the tropopause, achieves a maximum at an altitude of ~48 km, and then it decreases again till the altitude of 30 km. This change in the lapse rate coincides with the boundaries of different cloud layers. This change is caused by the heating of the cloud layers due to absorbed sunlight (Blamont and Ragent, 1979). Below this altitude the atmosphere is marginally stable till the surface with a small peak in the static stability at ~14 km altitude. This can be seen from the stability profile shown in Figure A.2. This static stability profile is further discussed in detail in Chapter 2.

Based on Pioneer Venus radio occultations, Kliore (1985) defined the tropopause at the altitude where the temperature lapse rate exceeds -8 K/km. This occurs at an altitude of ~ 58 km in the equatorial and polar latitudes and at ~ 62 km in cold collar region (explained below). Similar results are obtained from Magellan radio occultations (Jenkins et al., 1994) and VeRa data (Tellmann et al., 2009). The upper troposphere, extending from ~ 45 km till the tropopause, exhibits a clear latitudinal gradient in temperature (Haus et al., 2017, Tellmann et al., 2009) from the equator to the poles with the polar regions being colder by ~ 30 K (Figure A.3). The structure of the lower troposphere from 45km to the surface is discussed in detail in Chapter 2

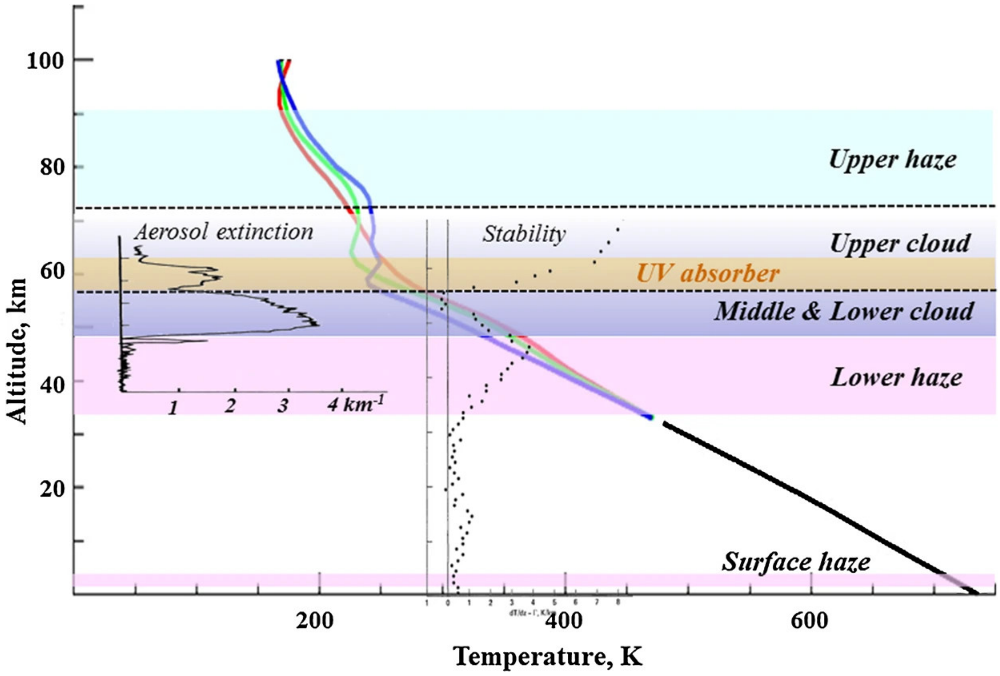

Figure A.2: The atmospheric structure of the Venus as derived by the Venera and Pioneer Venus descent probes. The color lines show mean temperature profiles at low (red), middle (blue) and high (green) latitudes with a single black line representing the temperature structure below 30 km. The typical vertical profile of aerosol extinction (Ragent et al., 1985) is given on the left. In the middle, the static stability profile (Seiff et al., 1985) from the VIRA model is shown. This image is taken from Titov et al. (2018).

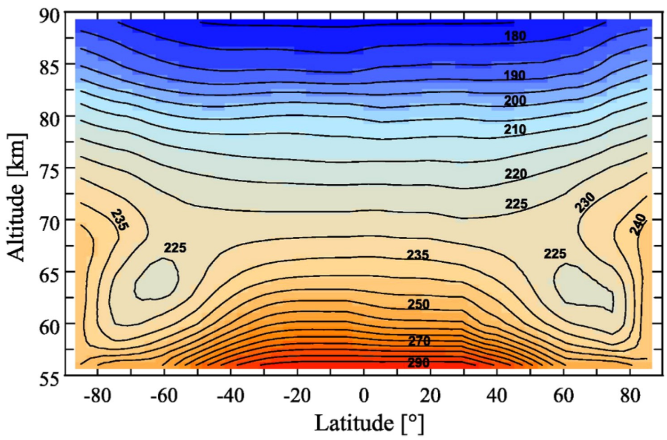

Figure A.3: Average temperature vs altitude-latitude profile in the Venus night-time hemisphere from VIRTIS-M dataset. This image is derived from Haus et al. (2017)

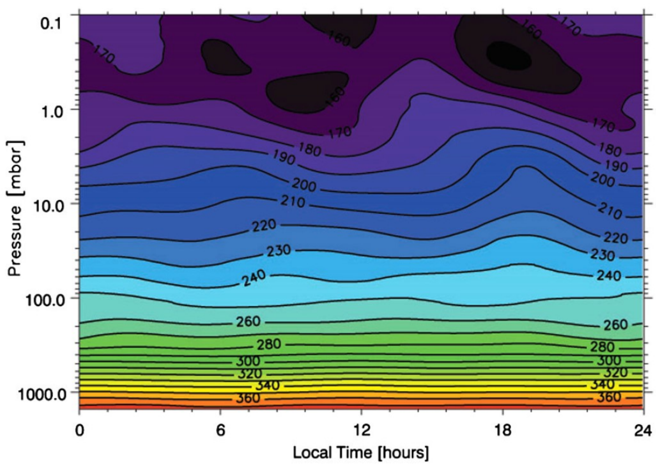

Figure A.4: Average temperature vs Pressure-local time in the equatorial region (lat ≤ ± 20°) from VeRa measurements (Tellmann et al., 2012)

Unlike Earth, Venus does not have a stratosphere. Thus, the **mesosphere** directly starts above the tropopause. The lower mesosphere extends till 90 km and above that the upper mesosphere till 150 km (Limaye et al., 2018a). Figure A.3 shows the average temperature vs. altitude-latitude cross-section of the night-side atmosphere of Venus as derived from VIRTIS-M dataset by Haus et al. (2017). A similar temperature field is obtained from VeRa measurements by Tellmann et al. (2009), from VIRTIS-M nightside measurements by Grassi et al. (2014), and these results are supported by Pioneer Venus measurements (Seiff et al., 1980) and Venera 15 results (Zasova et al., 1996). It can be observed that the temperature field is symmetric about the equator. Just below the altitude of the tropopause (~ 60 km) the temperature decreases from the equator to the pole. These meridional temperature gradients are small and are consistent with the zonal flow and in approximate cyclostrophic balance. A local temperature minimum can be seen at ~65 km altitude and 65°latitude in both hemispheres which is known as the 'cold collar region.' This region occurs due to the presence of an inversion layer (Limaye et al., 2018a). The temperature field in this altitude range further shows a three dimensional structure showing changes with the local time. From the night-side VIRTIS data, the rise of temperature towards the terminator can be observed (Tellmann et al., 2009).

The meridional temperature gradient changes as we move upwards from 70 km to 90 km with the temperature at the poles being higher than that at the equatorial latitudes. The subsidence due to the convergence of the mean meridional flow of the pole-ward branch of the Hadley circulation causes the adiabatic heating of the polar region which increases the temperature in the polar region. Similar to the lower altitudes, in the range of 70-90 km, a three-dimensional structure of the temperature field can be observed with temperatures increasing towards both the terminators from minima at 2:00 to 3:00 LT. In the equatorial region, a semidiurnal structure can be observed from Figure A.4 with the minimum temperature occurring at both terminators. This structure is observed from VeRa measurements (Tellmann et al., 2012) and earlier from the OIR experiment onboard the Pioneer Venus spacecraft (Schofield and Taylor, 1983). The static stability in the mesosphere is generally high. The upper mesosphere shows a more complex structure with alternative layers of warm and cold temperatures. In the upper layers, the temperature falls to 120 K.

A.2. Clouds and Hazes

Characterized by a continuous global cloud cover, the planet Venus shows a complex clouds system. The clouds are located in the altitude range of 45 to 75 km along with the haze layers extending above up to 90-100 km and below up to ~30 km altitude. A small layer of haze near the surface is also suspected (Grieger et al., 2004). The in-situ and remote sensing observations from Venera, Pioneer Venus, VeGa, Magellan, Venus Express, and recently, by Akatsuki orbiter have contributed towards establishing the global cloud structure which has been extensively reviewed by Esposito et al. (1983, 1997), Titov et al. (2018) and it is briefly described in this section.

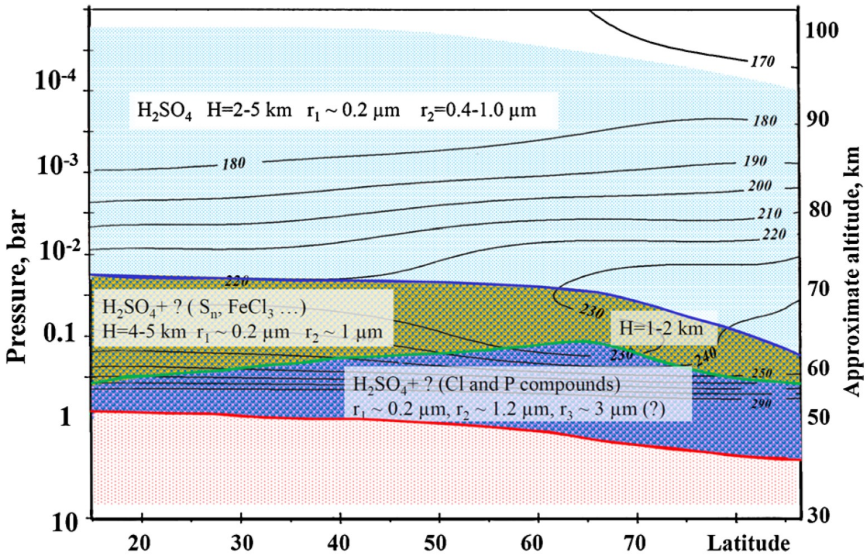

Figure A.5: The latitude-altitude structure of clouds showing the upper haze (light blue), upper cloud (blue and yellow droplets), middle and lower clouds (blue and red droplets), lower haze (red droplets). The temperature field of Venera-15 is shown by the black countours. Blue, green and red solid lines define the cloud top, the tropopause and the cloud base respectively. This image has been taken from (Titov et al., 2018)

Figure A.2 shows the average location of the cloud layers, while the latitude-altitude structure of clouds (symmetric about the equator) is shown in Figure A.5 along with their micro-physical properties. The black contours in Figure A.5 show the temperature field measured by Venera 14 (Lellouch et al., 1997) which is similar to the temperature field discussed earlier in Section A.1. The **upper haze** (shown by light blue color) extends from the cloud tops up to ~100 km altitude in the mesosphere and it is primarily composed of sub-micron sized ($r_1 \sim 0.2$µm) sulphuric acid particles. These values are shown in Table A.1, which are based on the Pioneer Venus dataset of particle distribution by Knollenberg and Hunten (1980) which is the most comprehensive particle size dataset in use. Knollenberg (1984) suggests that the particles may have not-spherical shapes as well.

The cloud tops, defined at an optical depth of $\tau = 1$, are observed at an altitude of 70km in the equatorial region and the mid-latitudes, and they descend to ~ 60 km altitude in the polar region. Similarly, the aerosol scale height (H) decreases from 4-5 km at the mid-latitudes to 1-2 km in the polar region. The **upper cloud** (shown by blue and yellow droplets in

Table A.1: Venus cloud system Parameters from Esposito et al. (1983) while the modes of aerosol popullation are taken from Knollenberg and Hunten (1980)

Region	Altitude range (km)	Optical depth, \tau (at 0.63 μm)	Mean diameter (μm)	Average number density (N cm^{-3})
Upper haze	70–90	0.2–1.0	0.4	500
Upper cloud	56.5–70	6.0–8.0	Mode 1: 0.4	1500
			Mode 2: 2.0	50
Middle cloud	50.5–56.5	8.0–10.0	Mode 1: 0.3	300
			Mode 2: 2.5	50
			Mode 3: 7.0	10
Lower cloud	47.5–50.5	6.0–12.0	Mode 1: 0.4	1200
			Mode 2: 2.0	50
			Mode 3: 8.0	50

Figure A.5) consists of photo-chemically produced Sulphuric acid droplets along with possibly solid Sulphur particles in small amounts. This region has bi-modal particle size distribution with a typical radii of r_1 ~0.2 μm (mode 1), 1 μm (mode 2). There is also a presence of mysterious UV absorber which allows us to trace the dynamic behavior of the upper cloud layer, however, its chemical origin is not yet known. Limaye et al. (2018b) suggest a possible biological origin for this UV absorber and warrant further investigation on this topic.

The tropopause (shown by the green line in Figure A.5) separates the upper cloud from the **middle and lower clouds**. It forms the physical base of the upper cloud with the region of photochemical production of Sulphuric acid above and the condensation cloud below it (Titov et al., 2018). The middle and lower clouds (shown by blue and red droplets in Figure A.5) extend below the tropopause up to an altitude of 48-50 km in the equatorial region and the mid-latitudes, and up to 45 km near the polar region Barstow et al. (2012). They are often separated from the upper clouds by 1-2 km gap accompanied by reduced aerosol extinction which can be seen from Figure A.2. However, a clear separation is not observed between the middle cloud and the lower cloud. The cloud density gradually increases as we traverse downwards from the tropopause and it is maximum near an altitude of ~50 km. This region showcases a trimodal particle size distribution with typical radii of r_1 ~ 0.15 - 0.2 μm (mode 1), r_2 ~ 1-1.25 μm (mode 2), and r_3 ~ 3.5-4 μm (mode 3), with Sulphuric acid as the major constituent along with Chlorine and Phosphorous abundances (Andreichikov, 1987). From Figure A.2 it can be observed that the atmosphere in this region is marginally stable indicating convective energy and material transport.

The **lower haze** (shown by red droplets in Figure A.5) extends below the cloud base up to an altitude of ~ 33 km and consists of more tenuous layers of particles. The high temperature in this region causes thermal decomposition of sulphuric acid droplets. Thus, the primary component of this layer is not yet known (Titov et al., 2018). Also, there is a possibility of a **near-surface haze** layer at an altitude of 1-2 km indicated by Venera 13, 14 descent probes (Grieger et al., 2004). This layer could be associated with dust or volcanic ash lifted up by the winds. However, further investigations possibly by radar observations or by using the near-IR surface observing windows are required.

A.3. Global Circulation and Dynamics

The atmosphere of Venus, which is most massive when compared with all the terrestrial planets, shows complex patterns of global circulation. It plays an important role in maintaining the thermal and compositional structure of the atmosphere over longer time scales. It is primarily characterized by three features: the zonal super-rotation, the Hadley circulation, and the polar vortices. The models of atmospheric dynamics and global circulation were sequentially established through previous missions and have been subsequently reviewed by Moroz (1981), Schubert and G. (1983),Gierasch et al. (1997), Drossart and Montmessin (2015), Sánchez-Lavega et al. (2017). This section gives a brief overview of the general circulation and dynamics.

The higher cloud layers travel parallel to the equator in a period of four to five days which is around ~60 times faster than the planet rotates around itself. Thus, this phenomenon is called **Super-Rotation**. The zonal winds flow towards the West and thus, the super-rotation phenomenon is also called the Retrograde Super-Rotation (RSR). The wind speeds reach a peak velocity of ~100 m/s at 65 km altitude decline on both sides as we travel downward and upwards from the upper cloud layer, with the velocity reaching near-zero values at the surface and the mesopause, respectively (Counselman et al.,

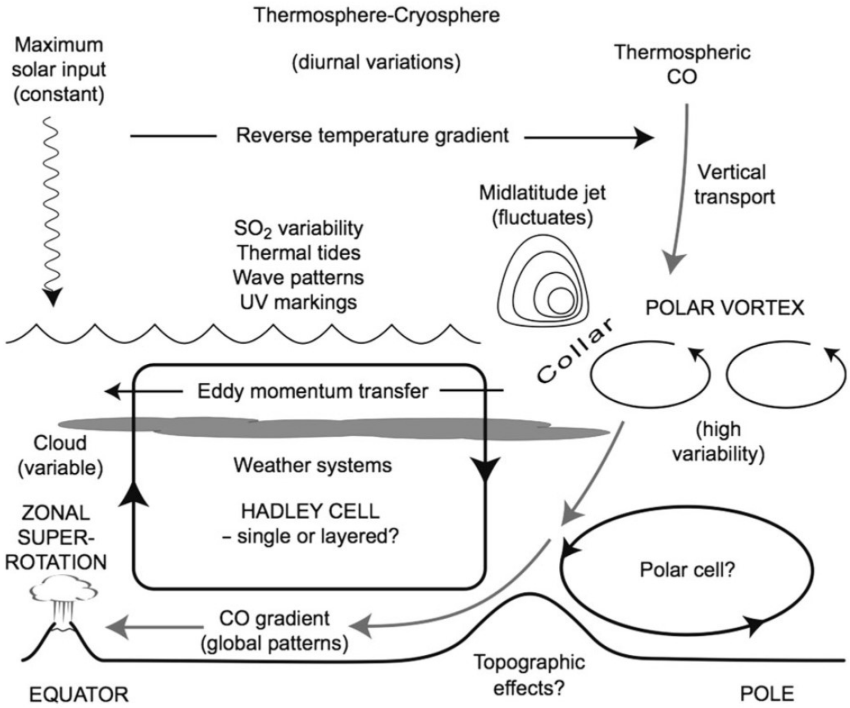

Figure A.6: A schematic of the primary features of general circulation in the atmosphere of Venus (Taylor and Grinspoon, 2009)

1980, Hueso et al., 2015). The deceleration of the zonal winds above the clouds is due to the pressure gradient caused by the temperature distribution in the higher altitudes, while that below the clouds is due to an increase in density and drag as we traverse from the clouds to the surface. The velocities in the near-surface layer remain low, increasing from 0.5 m/s near-surface to ~ 3 m/s near ~ 10 km altitude (Kerzhanovich, 1983). The available measurements cover a period of more than 50 years which leads to the conclusion this phenomenon of super-rotation is permanent in time with ~10-20 % velocity fluctuations (Sánchez-Lavega et al., 2017).

From equator towards the mid-latitudes, the meridional circulation is observed in both the hemispheres where the flow rises in the equatorial regions, travels towards the mid-latitudes, sinks down, and then returns towards the equatorial region again. This phenomenon is known as the **Hadley Cell** (Figure A.6). A sharp transition is observed at the latitude of ~65°where the Hadley cell is terminated. This gives rise to the highest winds forming the compact midaltitude jet and a belt of cold air surrounding the poles known as the **cold collar**. Within the cold collar, to conserve mass the air inside polar vortex descends rapidly which suppresses the cloud formation. This forms the' eye' of the polar vortex which is elongated in shape with brightness maxima at the two ends. The wave modes which are developed at the poles are dominated by wavelike instability with two maxima. This feature is termed as the **polar dipole**. The polar dipole rotates much faster with a period of 2.7 Earth days at the North Pole (Taylor et al., 1980) and that of 2.5 Earth days at the South Pole (Piccioni et al., 2007). To understand the behavior of the complex circulation and dynamic processes in the atmosphere of Venus, various Global Circulation Models have been developed over time. They are discussed the Section 2.3.

B

IMPORTANT ATMOSPHERIC PARAMETERS

In this section, the atmospheric parameters which are encountered during the previous chapter are explained briefly. Here, the definitions are taken from Lebonnois and Schubert (2017), Limaye et al. (2018a).

The equations dealing with the specific heat, the internal energy, ideal gas law, and hydrostatic balance are given below.

- The change in the internal energy of an ideal gas due to temperature is given by

$$dU = c_v dT \tag{B.1}$$

  where, U is the internal energy, T is the temperature, c_v is the specific heat at constant volume,

- The relation between specific heat at constant pressure and the specific heat at constant volume for an ideal gas is given by the Mayer's Law as follow

$$\frac{R}{\mu} = c_p - c_v \tag{B.2}$$

  where, R is the universal gas constant, μ is the mean molecular mass, c_p is the specific heat at constant pressure.

- For an air parcel going under the adiabatic displacement, the first law of thermodynamics is given by

$$dU = -p dv \tag{B.3}$$

  where, v is the specific volume, i.e. $1/\rho$, p is the pressure.

- The equation of state for the ideal gas is given by

$$\rho = \frac{\mu p}{RT} \tag{B.4}$$

- The hydrostatic balance is given by

$$dp = \rho g dz \tag{B.5}$$

Above equations are required in the upcoming sections for the derivations of various parameters.

Now, when the mean molecular mass (μ) is constant, the Equation B.4 can be rewritten as

$$pv = \frac{R}{\mu} T \tag{B.6}$$

Differentiating above equation

$$pdv + vdp = \frac{R}{\mu} dT \tag{B.7}$$

From Equation B.1 and Equation B.3 we get

$$pdv = -c_v dT \tag{B.8}$$

From Equation B.2 and Equation B.7 we get

$$vdp = c_p dT \tag{B.9}$$

Using Equation B.4 and Equation B.9 we get

$$\frac{R}{\mu} \frac{dp}{p} = c_p \frac{dT}{T} \tag{B.10}$$

B.1. Considering constant μ

B.1.1. Temperature Lapse Rate

A temperature lapse rate (Γ) is the change in temperature (T) with height (z).

$$\Gamma = \frac{dT}{dz} \tag{B.11}$$

The lapse rate of an air parcel is equal to adiabatic lapse rate when no energy is transferred to or from it from the surrounding atmosphere. Using Equation B.4,Equation B.5,Equation B.10, the equation for the adiabatic lapse rate (Γ_{adiab}) is given by,

$$\Gamma_{adiab} = \left(\frac{dT}{dz}\right)_{adiab} = -\frac{g}{c_p} \tag{B.12}$$

where g is the standard gravity given in m/s^2, c_p is the specific heat capacity at constant pressure given in J/(kg K). The unit of lapse rate (Γ) then becomes K/m which is usually converted into K/km for convenience.

Note: above relation holds for an ideal gas with constant mean molecular mass (μ).

B.1.2. Potential Temperature

The potential temperature θ is defined as the temperature that an air parcel would get after undergoing an adiabatic displacement from its position (T, p) to a reference pressure p_{ref}. For an atmospheric layer with constant c_p and μ, θ is given by integrating Equation B.10 from its position T, p to the reference pressure θ, p_{ref}. Thus, θ is given by,

$$\theta = T\left(\frac{p_{ref}}{p}\right)^k \tag{B.13}$$

Here, k is defined as

$$k = \frac{R}{\mu c_p} \tag{B.14}$$

However, when the c_p depends on the temperature, it is given by

$$c_p = c_{p0}\left(\frac{T}{T_0}\right)^{\nu} \tag{B.15}$$

For Venus, c_{p0}=1000 $Jkg^{-1}K^{-1}$, $T_0 = 460K$, $\nu = 0.35$ (Ledoux, 1947a, Poling et al., 2001, Span and Wagner, 1996)

Now, the expression of θ is given by

$$\theta^{\nu} = T^{\nu} + \nu T_0^{\nu} ln\left(\frac{p_{ref}}{p}\right)^{k0} \tag{B.16}$$

where, $k0$ is given by

$$k0 = \frac{R}{\mu c_{p0}} \tag{B.17}$$

B.1.3. Static Stability

The static stability is a measure to assess the convective stability of an atmospheric layer. In an unstable atmosphere, when moving a parcel of air adiabatically along the vertical in a well-mixed atmosphere, if the parcel rises to a colder environment, it will continue to rise or if it sinks in a warmer environment, it will continue to sink. This corresponds to the atmospheric lapse rate Γ lower than adiabatic lapse rate Γ_{adiab} denoting an unstable atmospheric layer under convective activity. Here, static stability (S) is defined as the difference between the temperature lapse rate of an atmospheric layer and the adiabatic lapse rate of that layer. It is given by,

$$S = \Gamma - \Gamma_{adiab} = dT/dz - \Gamma_{adiab} \tag{B.18}$$

The static stability is also be given by taking the vertical gradient of the potential temperature. It is given by,

$$S = \frac{1}{\theta}\frac{d\theta}{dz} \tag{B.19}$$

Now, when the S is positive, the atmosphere is stable. When the S is negative, the ambient temperature lapse rate is higher than adiabatic lapse rate and the atmosphere is unstable. In this condition, the ambient temperature lapse rate is known as super-adiabatic lapse rate which denotes that the atmosphere is convectively unstable.

B.2. Static Stability for a varying μ

The theory shown below is taken from Hess (1979), Lebonnois and Schubert (2017), Ledoux (1947b).

B.2.1. Adiabatic Lapse Rate for varying μ

Consider a parcel of air that is displaced adiabatically on an elemental distance dz. Consider an atmospheric layer where mean molecular mass, μ, varies with the altitude, pressure, or temperature. Here, the notation x' denotes the variable x inside the parcel.

For the parcel, the equation of state for an ideal gas can be written as,

$$p'\mu' = \rho' R T' \tag{B.20}$$

For an elemental distance dz, the μ' does not change as the composition of the parcel itself does not change. Now, taking log and differentiating vertically with respect to the elemental distance dz, we get

$$\frac{1}{p'}\frac{dp'}{dz} = \frac{1}{\rho'}\frac{d\rho'}{dz} + \frac{1}{T'}\frac{dT'}{dz} \tag{B.21}$$

Applying Equation B.10 to the parcel and combining the terms dp'/dz, we get,

$$\frac{1}{\rho'}\frac{d\rho'}{dz} = \frac{1}{p'}\frac{dp'}{dz}(1-k') \tag{B.22}$$

where, $k' = R/(\mu' c_p)$. Here, as we are varying only μ with the altitude, c_p' is not used (Lebonnois and Schubert, 2017).

For the gas surrounding the parcel, the equation of state can be written same as Equation B.4.

$$\rho = \frac{\mu p}{RT} \tag{B.23}$$

Taking the logarithm and then differentiating along the vertical axis, we get,

$$\frac{1}{\rho}\frac{d\rho}{dz} = \frac{1}{\mu}\frac{d\mu}{dz} + \frac{1}{p}\frac{dp}{dz} - \frac{1}{T}\frac{dT}{dz} \tag{B.24}$$

Here, the stability criterion is

$$\frac{1}{\rho'}\frac{d\rho'}{dz} > \frac{1}{\rho}\frac{d\rho}{dz} \tag{B.25}$$

Hence, from equations Equation B.24 and Equation B.21 we get,

$$\frac{1}{\mu}\frac{d\mu}{dz} + \frac{k'}{p}\frac{dp}{dz} - \frac{1}{T}\frac{dT}{dz} < 0 \tag{B.26}$$

Here, the adiabatic lapse rate is obtained at neutral stability,

$$\frac{1}{\mu}\frac{d\mu}{dz} + \frac{k'}{p}\frac{dp}{dz} - \frac{1}{T}\frac{dT}{dz} = 0 \tag{B.27}$$

Now, for an elemental displacement, the ratio $k/k' \sim 1$. Using Equation B.5 and Equation B.23 we get,

$$\Gamma_{adiab} = \frac{T}{\mu}\frac{d\mu}{dz} - \frac{g}{c_p} \tag{B.28}$$

This equation provides the adiabatic lapse rate for vertically varying μ. However, it is also valid when c_p is vertically varying (Lebonnois and Schubert, 2017).

B.2.2. Potential Temperature for Varying μ

The potential temperature of the parcel is found out based on its potential density (ρ_θ). ρ_θ is defined as the density a parcel with the density $\rho(\mu, T, p)$ would have when displaced adiabatically and with constant composition to the reference pressure i.e. $\rho(\mu, \theta, p_{ref})$. Based on Equation B.23, the potential density is given by,

$$\rho_\theta = \frac{\mu p_{ref}}{R\theta} = \frac{\mu_{ref} p_{ref}}{R\theta'} \tag{B.29}$$

where, modified potential temperature θ' is defined by,

$$\theta' = \theta(\mu_{ref}/\mu) \tag{B.30}$$

The θ depends on μ and as μ is varying with the altitude, it is not correct to use the stability criterion as the direct comparison of potential density between two atmospheric levels (Pierrehumbert, 2010).

$$\therefore \frac{1}{\rho_\theta}\frac{d\rho_\theta}{dz} = \frac{1}{\mu}\frac{d\mu}{dz} - \left(\frac{1}{\theta}\frac{\partial\theta}{\partial z}\right)_\mu - \left(\frac{1}{\theta}\frac{\partial\theta}{\partial\mu}\right)_z \frac{d\mu}{dz} \tag{B.31}$$

For an elemental displacement, from the definition of θ,

$$\left(\frac{1}{\theta}\frac{\partial\theta}{\partial z}\right)_\mu = -\frac{k'}{p}\frac{dp}{dz} + \frac{1}{T}\frac{dT}{dz} \tag{B.32}$$

Substituting Equation B.32 in Equation B.31 we get,

$$\therefore \frac{1}{\rho_\theta}\frac{d\rho_\theta}{dz} = \frac{1}{\mu}\frac{d\mu}{dz} - + \frac{k'}{p}\frac{dp}{dz} - \frac{1}{T}\frac{dT}{dz} - \left(\frac{1}{\theta}\frac{\partial\theta}{\partial\mu}\right)_z \frac{d\mu}{dz} \tag{B.33}$$

Thus, above equation shows that the $\frac{d\rho_\theta}{dz} = 0$ is not equivalent to the criterion for stability shown earlier in Equation B.27. This is true unless the last term on the RHS of the equation is negligible against the first.

For the deep atmosphere of Venus, the vertical profile of $\theta(\mu)$ is very close to the profile of $\theta(\mu_{ref})$, with the difference between the two not exceeding 0.15 K everywhere (Lebonnois and Schubert, 2017). Here, μ_{ref} = 43.44 g mol^{-1} which corresponds to 3.5 % N_2 mixed with CO_2. Now, for θ at the surface of 735 K, with a $\partial\theta/\partial\mu = 0.15/0.56$ (Lebonnois and Schubert, 2017), we get

$$\frac{\mu}{\theta}\frac{\partial\theta}{\partial\mu} = \frac{43.44}{735} \times \frac{0.15}{0.56} \sim 0.016 << 1 \tag{B.34}$$

Thus, it can be approximated that θ is not dependent on inital μ, i.e. $\partial\theta/\partial\mu = 0$ at any altitude. Thus, the stability criterion is equivalent to the Equation B.19 applied to the modified potential temperature θ'. Thus, we can simplify the relation to:

$$\frac{1}{\theta'}\frac{d\theta'}{dz} = 0 \tag{B.35}$$

C

Data Processing

C.1. Data Selection

Table C.1 gives a brief summary of the observations taken by the Akatsuki orbiter from IR1 (at 1.01 μm) and IR2 (at 1.74 and 2.32 μm) cameras. The orbits containing useful observations are highlighted in bold and a total of 45 observations are used in our analysis. For a possible cloud opacity correction, simultaneous observation in 1.7 and 2.3 μm windows are required. Thus, we also investigated the observations taken from the IR2 camera for corresponding orbits. These observations are also listed in the Table C.1. However, the IR2 camera was operated from between ~2 hours up to several days after the IR1 camera. Thus, an exact correction for the cloud opacity variations is not possible from these images.

Table C.1: Orbits of Akatsuki spacecraft highlighting useful observations

Orbit	IR1 observations at 1.01 μm	IR2 observations at 1.74 and 2.3 μm
c0000	Testing and Calibration	
r0001	-	-
r0004	1 good image	-
r0005	4 useful images	-
r0006	3 useful images	-
r0007	Not useful	-
r0008	Not useful	-
r0009	Not useful	-
r0010	1 useful image	-
r0011	1 useful image	Nightside visible in one quadrant (small size)
r0012	No observations	-
r0013	No observations	-
r0014	No observations	-
r0015	No observations	-
r0016	No observations	-
r0017	No observations	-
r0018	No observations	-
r0019	No observations	-
r0020	Full nightside disk visible, 2 useful images	Full nightside disk visible
r0021	Full nightside disk visible, 2 useful images	Full nightside disk visible
r0022	Full nightside disk visible, 2 useful images	Nightside disk visible in one quadrant (small size)
r0023	Full nightside disk visible, 6 useful images	Full nightside disk visible (small size)
r0024	Not Useful	-
r0025	Full nightside disk visible, 2 useful images	Full nightside disk visible
r0026	Full nightside disk visible, 8 useful images	Full nightside disk visible
r0027	Not Useful	-
r0028	Full nightside disk visible, 2 useful images	Full nightside disk visible
r0029	Not Useful	-
r0030	Full nightside disk visible, 5 useful images	Full nightside disk visible (small size)
r0031	Full nightside disk visible, 4 useful images	Full nightside disk visible
r0032	No observations	-
r0033	Full nightside disk visible, 2 useful images	-
r0034	No observations	-

D
Results

This chapter provides the high resolutions version of the maps discussed in Section 6.3 and Section 2.5.

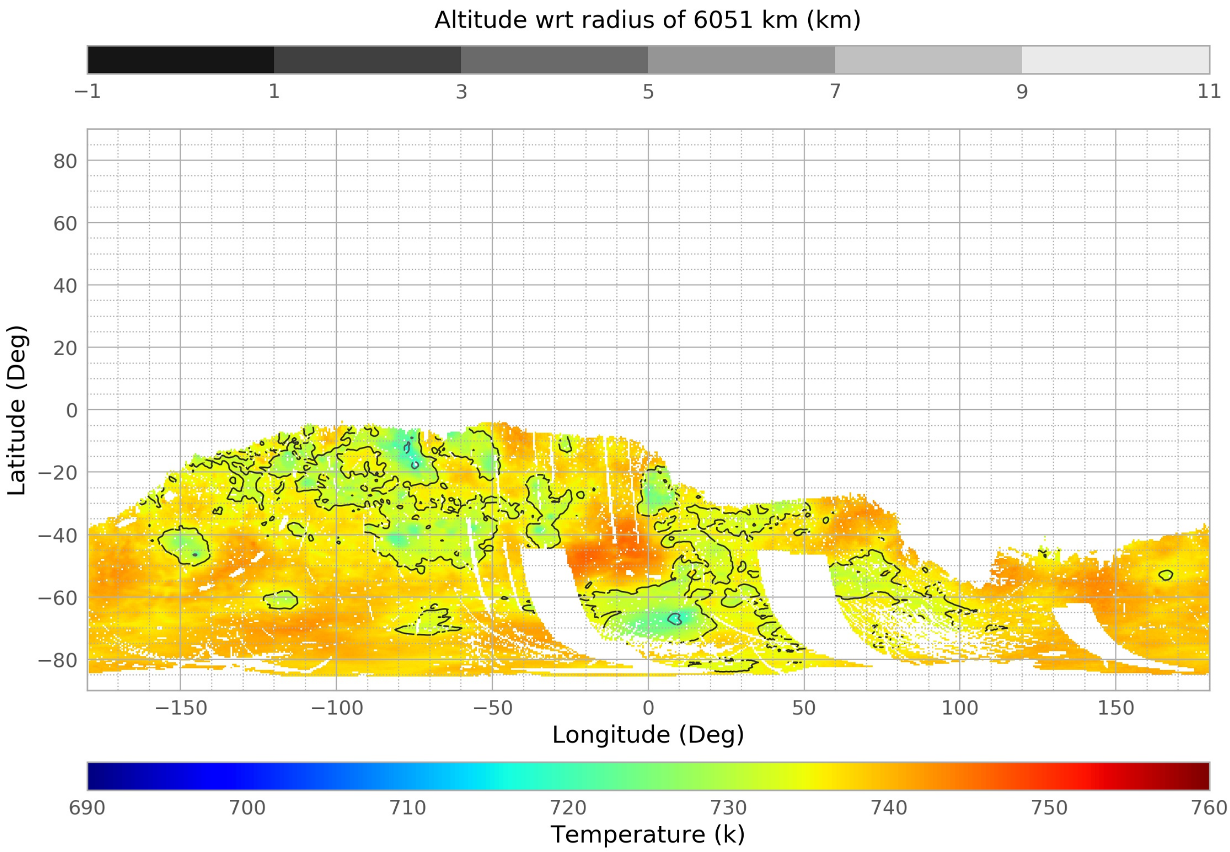

Figure D.1: Map of the surface temperatures retrieved from the VIRTIS dataset using the model described in Chapter 5. The description of this map is provided in Section 6.3.

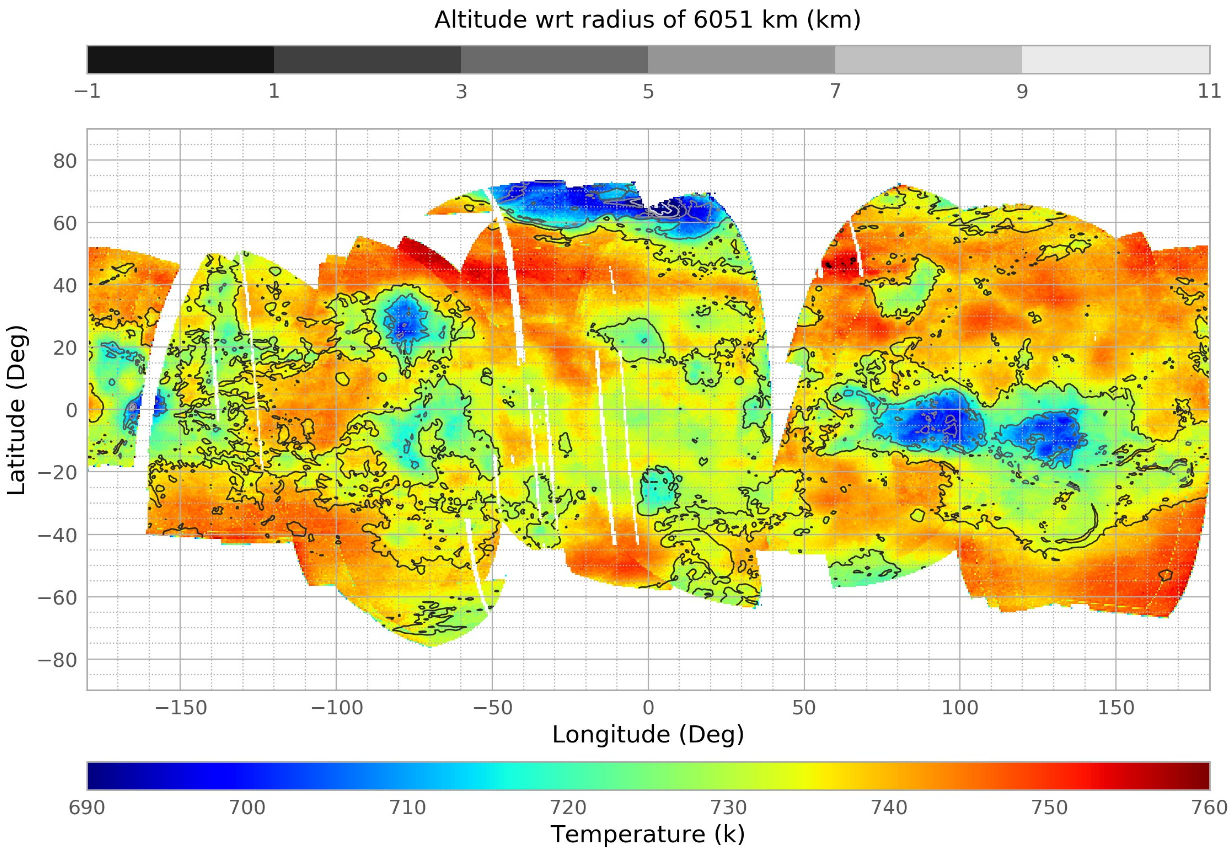

Figure D.2: Map of the surface temperatures retrieved from the IR1 dataset (level 3h) using the model described in Chapter 5. The description of this map is provided in Section 6.3

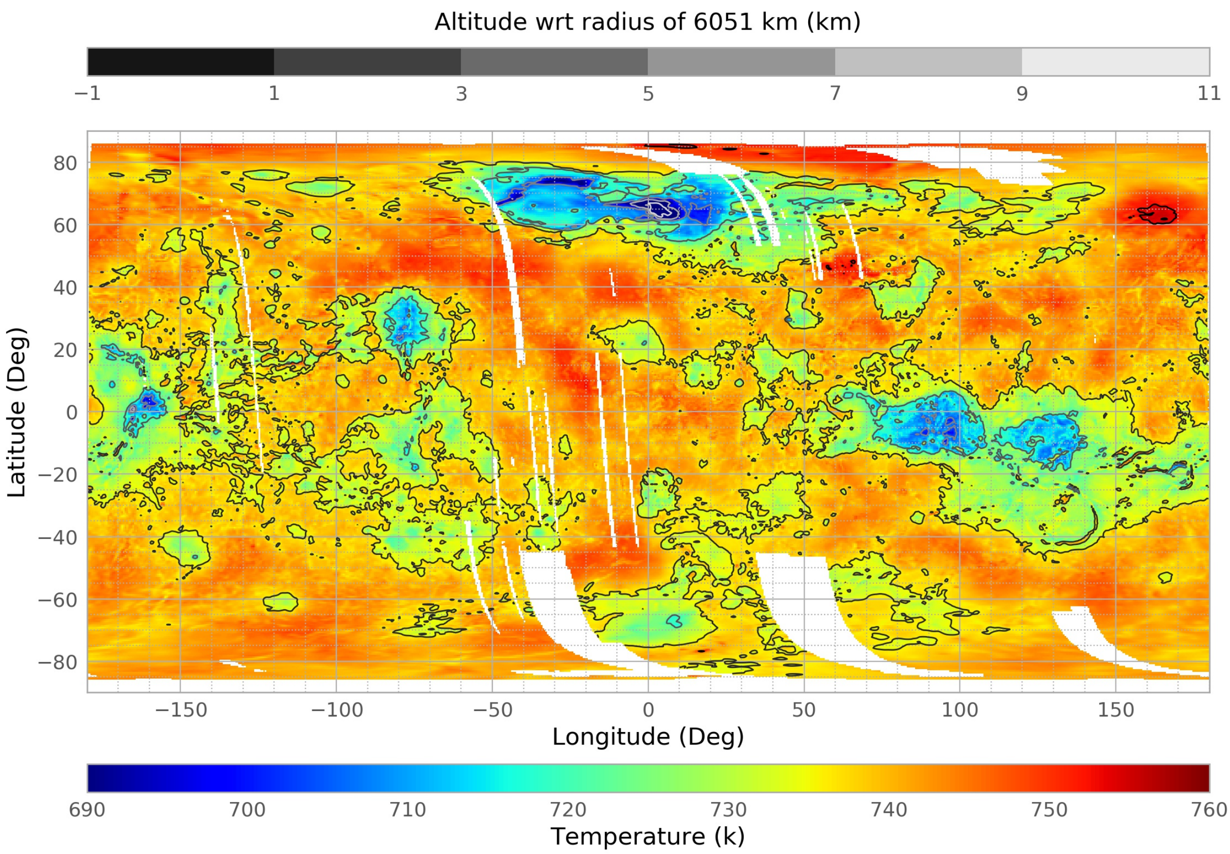

Figure D.3: Map of the surface temperatures generated by correlating surface topography with the VIRA temperature profile. The description of this map is provided in Section 6.3.

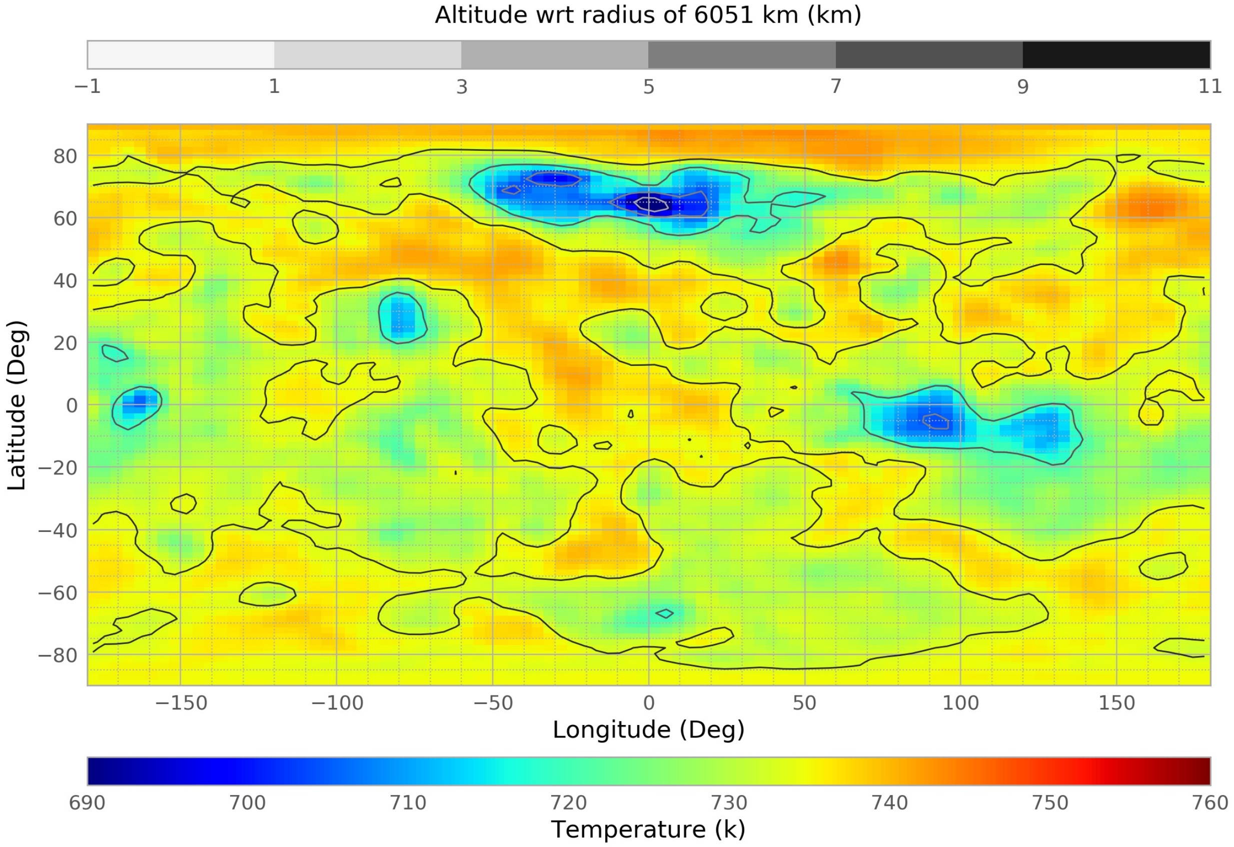

Figure D.4: Map of the surface temperatures generated by using the results from the GCM without the N_2 gradient (Lebonnois et al., 2018). The description of this map is provided in Section 2.5.

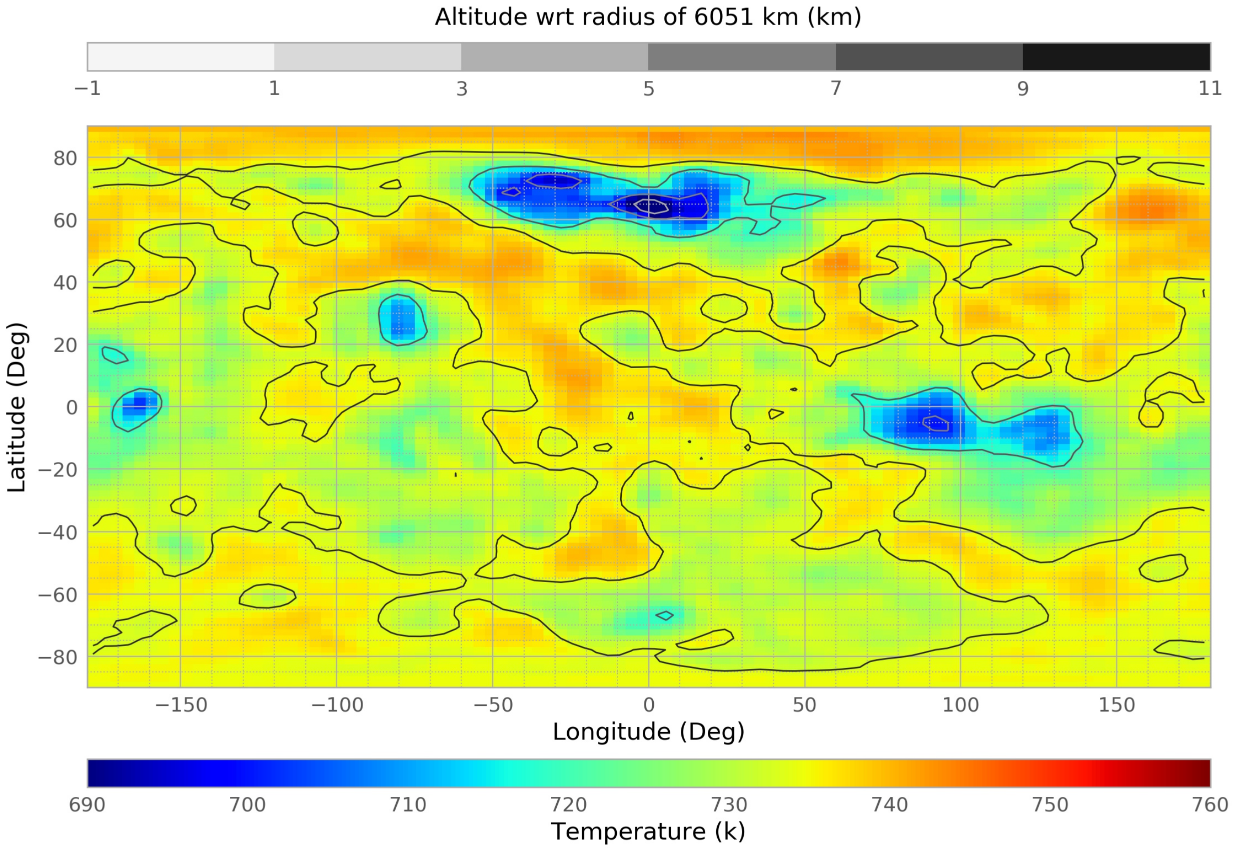

Figure D.5: Map of the surface temperatures generated by using the results from the GCM with the N_2 gradient (Lebonnois et al., 2018). The description of this map is provided in Section 2.5.

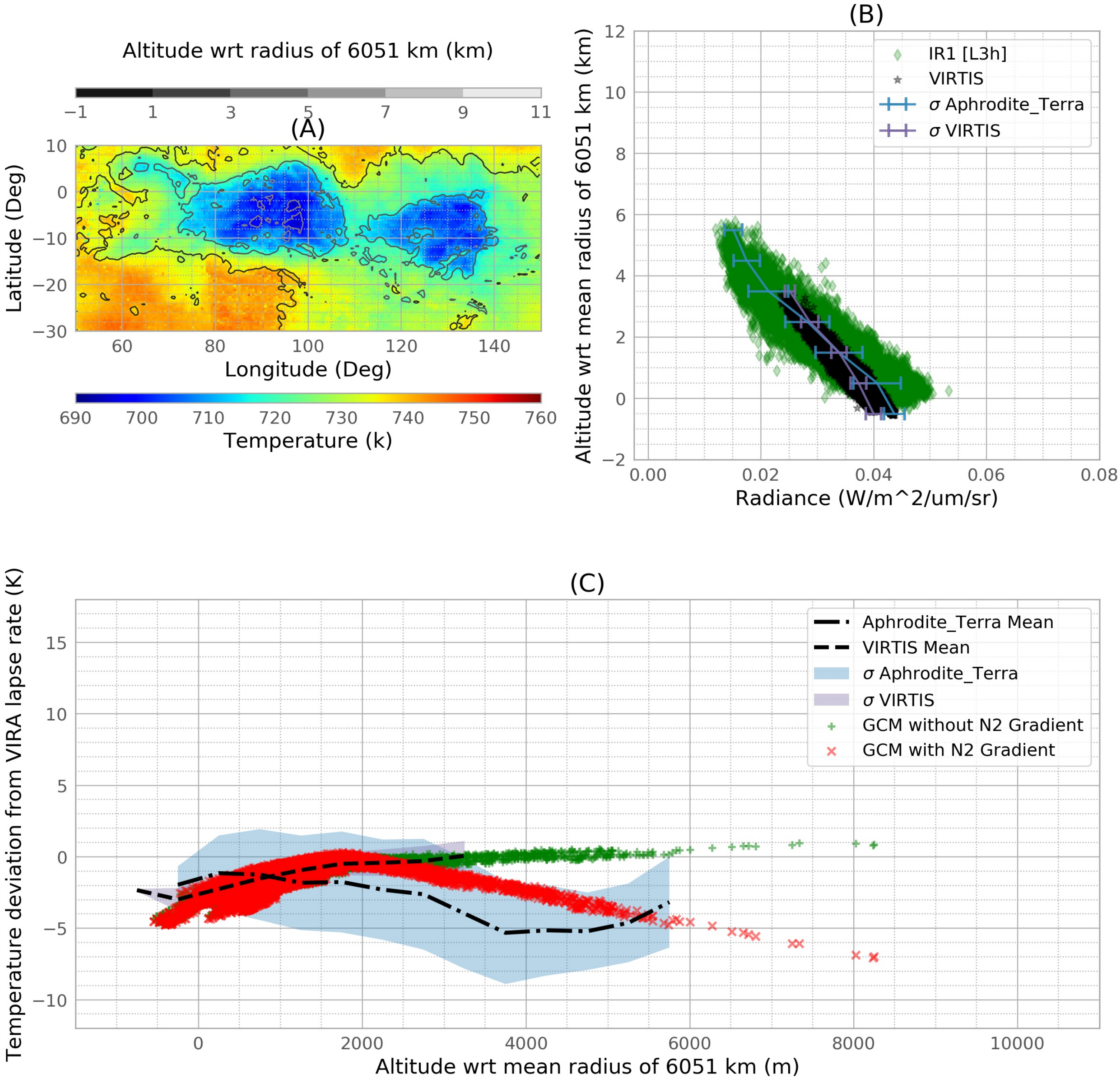

Figure D.6: (A) Surface temperature map of Aphrodite Terra extracted from the Figure D.2 and (C) the corresponding temperature deviation vs altitude plot. (B) the radiance vs altitude scatter plot of the extracted region. The description of this map is provided in Section 6.3.

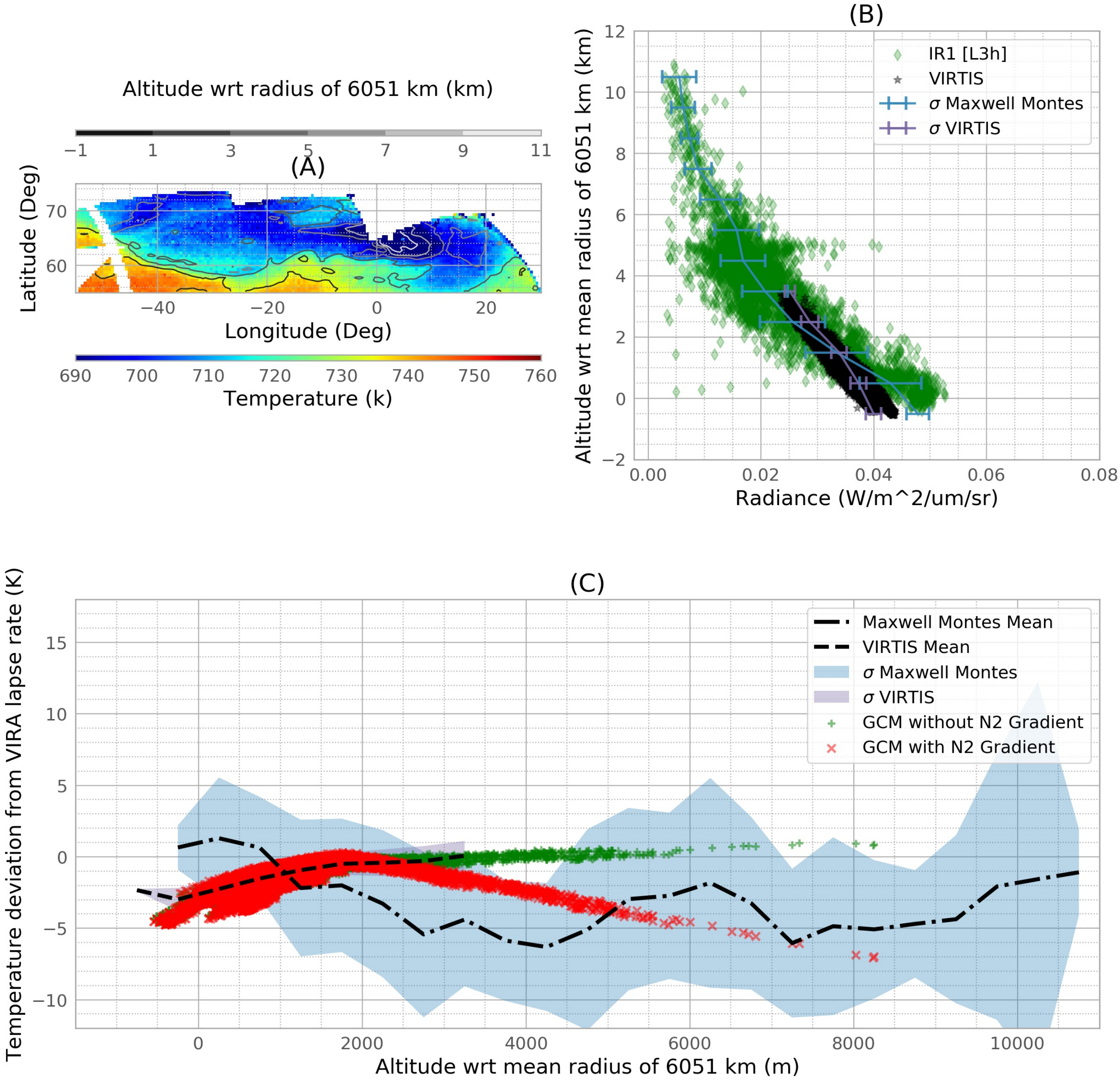

Figure D.7: (A) Surface temperature map of Maxwell Montes extracted from the Figure D.2 and (C) the corresponding temperature deviation vs altitude plot. (B) the radiance vs altitude scatter plot of the extracted region. The description of this map is provided in Section 6.3.

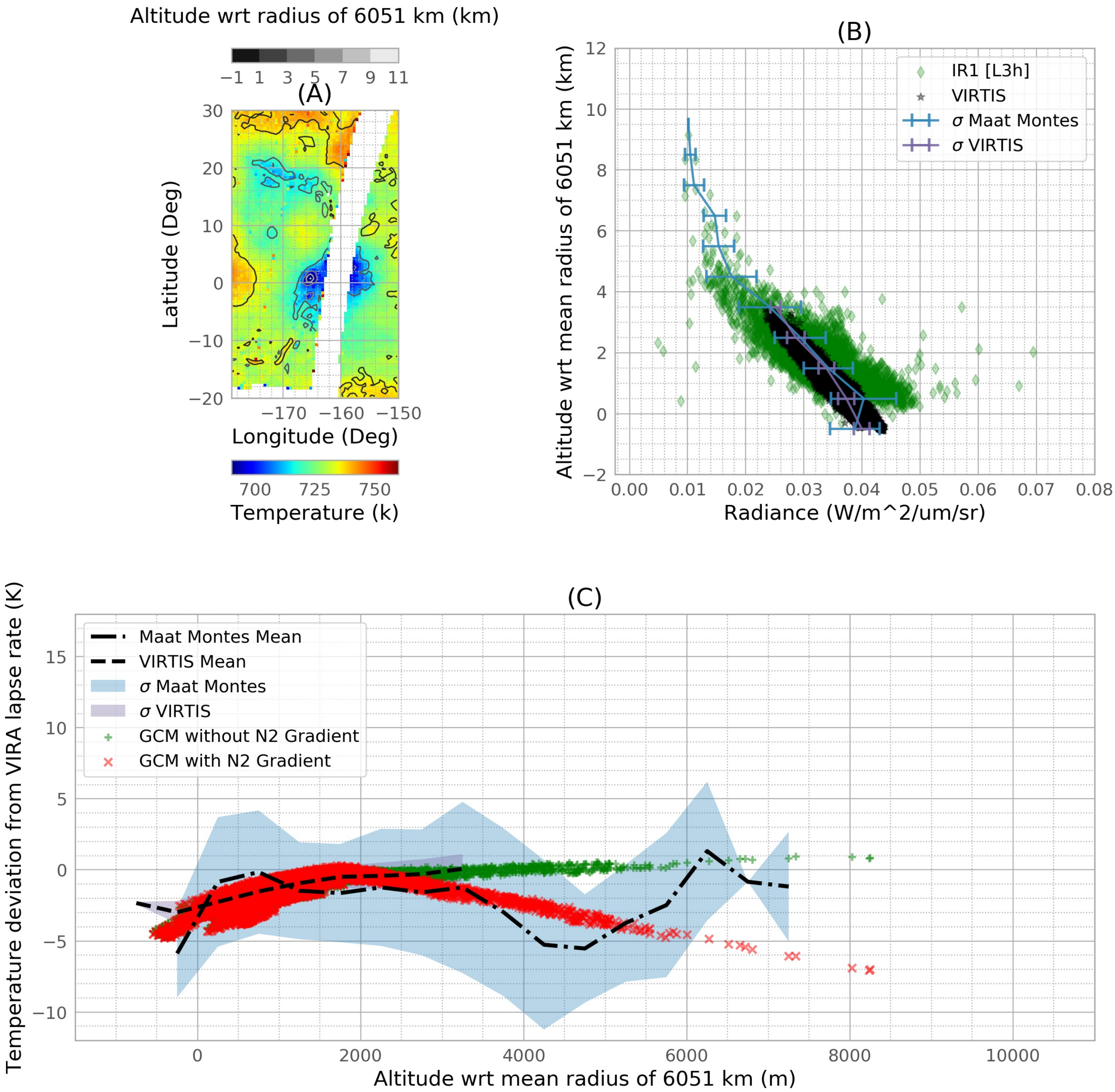

Figure D.8: (A) Surface temperature map of Maat Mons extracted from the Figure D.2 and (C) the corresponding temperature deviation vs altitude plot. (B) the radiance vs altitude scatter plot of the extracted region. The description of this map is provided in Section 6.3.